UNIVERSITÉ LAVAL

Planification de trajectoires analytiques point à point au-delà de l'espace statique pour des mécanismes parallèles suspendus entraînés par câbles

Thèse

Pascal Dion-Gauvin

Doctorat en génie mécanique
Philosophiæ doctor (Ph. D.)

Québec, Canada

Planification de trajectoires analytiques point à point au-delà de l'espace statique pour des mécanismes parallèles suspendus entraînés par câbles

Thèse

Pascal Dion-Gauvin

Sous la direction de:

Clément Gosselin, directeur de recherche

Résumé

L'objectif de ce travail de recherche est le développement de planifications de trajectoires analytiques de type point à point pour mécanismes à câbles suspendus complètement actionnés. Spécifiquement, cette thèse propose une planification de trajectoire point à point dite de transition pour mécanismes à effecteur ponctuel à 2 et à 3 degrés de liberté (ddl), ainsi que des planifications de trajectoires point à point classiques pour mécanismes spatiaux à 3 ddl, d'une part, et pour mécanismes à 6 ddl de type Gough-Stewart, d'autre part. Chaque trajectoire développée assure aux points limites une vitesse nulle et une accélération continue, en plus d'être spécifiquement construite dans le but de maintenir des forces exclusivement de tension dans les câbles tout au long du tracé.

La trajectoire de transition pour mécanismes à effecteur ponctuel à 2 ddl et à 3 ddl relie une pose à l'équilibre statique du mécanisme à une pose à accélération non-nulle et consiste en des oscillations rectilignes d'amplitude progressivement croissante centrées à la pose au repos. Il est établi que cette trajectoire est réalisable avec des forces exclusivement de tension dans les câbles pourvu qu'elle demeure entièrement sous le plan formé par les enrouleurs, ce qui en démontre la pertinence.

La trajectoire point à point destinée au mécanisme spatial à 3 ddl joint deux positions quelconques de l'espace tridimensionnel en suivant un tracé hypocycloïdal. Pour illustrer la pertinence de cette construction, il est démontré qu'il suffit que l'enveloppe circulaire de l'hypocycloïde soit entièrement située sous le plan des enrouleurs pour que la trajectoire souhaitée soit réalisable avec des forces exclusivement de tension dans les câbles.

Enfin, la trajectoire à 6 ddl destinée au mécanisme hexapodal relie deux poses arbitraires. Elle consiste, pour sa composante translationnelle, en une version améliorée de la trajectoire hypocycloïdale définie pour le mécanisme à 3 ddl, tandis que sa composante rotationnelle consiste en des oscillations angulaires le long des arcs de l'hypocycloïde. La pertinence de cette formulation est démontrée par le calcul, pour certaines positions génériques de la plateforme, de la proportion d'orientations que la trajectoire est en mesure de joindre avec un mouvement horizontal partant d'une pose au repos : il est obtenu que, pour des valeurs typiques, la planification proposée parvient à atteindre environ 90% de l'espace atteignable en orientation du mécanisme.

Abstract

The purpose of this work consists in the development of analytical point-to-point trajectory procedures for fully-actuated cable-suspended parallel mechanisms. Specifically, this thesis proposes a static-to-dynamic transition trajectory formulation for 2-degree-of-freedom (dof) and 3-dof mechanisms with point-mass end-effectors, as well as point-to-point trajectory formulations for spatial 3-dof and 6-dof mechanisms. Each proposed trajectory ensures a zero instantaneous velocity at the endpoints and the continuity of the acceleration, and is specifically designed to maintain tensile-only forces in the cables throughout the motion.

The proposed static-to-dynamic transition trajectory for the planar and spatial point-mass mechanisms connects a pose at rest in the static workspace to an arbitrary pose with a non-zero acceleration and consists of rectilinear oscillations of progressively increasing amplitude centred at the pose at rest. It is shown that this trajectory is dynamically feasible with tensile-only forces in the cables as long as it remains entirely below the plane passing by the fixed cable spools, which justifies its relevance.

The point-to-point trajectory intended for spatial 3-dof mechanisms connects two arbitrary positions in three-dimensional space by following a hypocycloidal path. In order to demonstrate the relevance of the proposed formulation, it is shown that it suffices that the circular envelope of the hypocycloid remains entirely below the plane passing by the cable spools for the desired motion to be feasible with tensile-only forces in the cables.

Finally, the 6-dof point-to-point trajectory intended for hexapodal mechanisms connects two poses with arbitrary position and orientation. It consists, for its translational component, in an enhanced version of the hypocycloidal trajectory defined for the 3-dof mechanism, while its rotational component consists of rotational oscillations along the arcs of the hypocycloid. The relevance of this construction is demonstrated by the computation, for generic positions of the platform, of the proportion of orientations that the trajectory can reach through a horizontal motion starting from a pose at rest: it is obtained that, for typical values, the proposed formulation can reach approximately 90% of the orientational workspace of the mechanism.

Table des matières

Résumé ii

Abstract iii

Table des matières iv

Liste des tableaux vi

Table des figures vii

Liste des vidéos viii

Remerciements ix

Avant-propos x

Introduction 1

1 Trajectory planning for the static to dynamic transition of point-mass cable-suspended parallel mechanisms 7
- 1.1 Résumé . . . 7
- 1.2 Abstract . . . 7
- 1.3 Introduction . . . 8
- 1.4 Planar Mechanism . . . 9
- 1.5 Spatial Mechanism . . . 20
- 1.6 The amplitude function . . . 29
- 1.7 Examples . . . 30
- 1.8 Conclusion . . . 34
- 1.9 Appendix A: Derivation of an effective amplitude function . . . 36
- 1.10 Appendix B: Study of nonhorizontal trajectories with the zero-tension amplitude function for horizontal trajectories . . . 38
- 1.11 Bibliography . . . 41

2 Dynamic point-to-point trajectory planning of a three-dof cable-suspended mechanism using the hypocycloid curve 44
- 2.1 Résumé . . . 44
- 2.2 Abstract . . . 44
- 2.3 Introduction . . . 45
- 2.4 Mechanism Modelling . . . 47

2.5 Plane of the Trajectory . . . 50
2.6 Hypocycloid Curve . . . 52
2.7 Proposed Trajectory . . . 54
2.8 Trajectory Feasibility . . . 55
2.9 Example Trajectory . . . 57
2.10 Conclusion . . . 61
2.11 Bibliography . . . 62

3 Beyond-the-static-workspace point-to-point trajectory planning of a 6-dof cable-suspended mechanism using oscillating SLERP 64
3.1 Résumé . . . 64
3.2 Abstract . . . 65
3.3 Introduction . . . 65
3.4 Introductory Concepts . . . 67
3.5 Properties of Quaternions . . . 71
3.6 Translational Trajectory . . . 75
3.7 Rotational Trajectory . . . 80
3.8 Trajectory Endpoints . . . 83
3.9 Static-to-Dynamic Transition Trajectory . . . 89
3.10 Workspace Analysis . . . 89
3.11 Trajectory Feasibility . . . 95
3.12 Simulations . . . 96
3.13 Conclusion . . . 105
3.14 Appendix: Derivation of the hypocycloid of variable amplitude . . . 106
3.15 Bibliography . . . 108

Conclusion 112

Bibliographie 115

Liste des tableaux

1.1 Nonceiled minimum feasible number of oscillations obtained for reaching—with a horizontal trajectory—a final point located at a distance $\widehat{d} = 4$ from the vertical axis passing through the centroid of the cable spools with the amplitude function $A_1(\tau)$ for the planar mechanism and for final points corresponding to points H_0 and H_1 of the spatial mechanism 31

1.2 Nonceiled minimum feasible number of oscillations obtained for reaching the final point ($\sigma R = 1, \xi = 1$) with various amplitude functions and inclinations . 33

1.3 Nonceiled minimum feasible number of oscillations obtained for reaching the final point ($\sigma R = 5, \xi = 0$) horizontally with various amplitude functions 34

2.1 Feasibility test and minimum feasible number of the example trajectory 59

3.1 Endpoint positions and orientations of the example trajectory 100

3.2 Results of the example point-to-point trajectory 100

3.3 Number of accessible and attainable orientations by the proposed trajectory for some final points 103

3.4 Minimum proportion of attainable orientations in the annulus defined by radii $1.5b$ and $3b$ for different heights of the platform 104

Table des figures

1.1 Planar two-dof cable-suspended mechanism 10
1.2 Pseudo-tension constraints 12
1.3 Static to dynamic rectilinear transition trajectory 14
1.4 Minimum value of N allowing instantaneous positive tension in each cable as a function of v 18
1.5 Spatial three-dof cable-suspended mechanism 21
1.6 Geometric interpretation of the weighted trajectory parameters 27
1.7 Spatial mechanism used to perform the experimental validation 32
1.8 Simulation results of the experimental validation 33
1.9 Comparison of various amplitude functions 35
1.10 Piecewise-defined amplitude function 36
1.11 Optimal inclination and its corresponding value of n for nonhorizontal trajectories 41

2.1 Spatial three-dof cable-suspended mechanism 47
2.2 Plane of the trajectory 51
2.3 Hypocycloid curve for $\theta_h = -\frac{4\pi}{3}$ and $n_h = 3$ 53
2.4 Hypocycloid curve connecting two points having $\psi_h = \frac{\pi}{2}$ with one, two, and three arcs respectively 53
2.5 Spatial 3-dof cable-suspended mechanism used to perform the experimental validation 58
2.6 Example trajectory 60
2.7 Computed tensions along the trajectory 60
2.8 Computed tensions along the third segment with 5 and 7 arcs respectively . . . 61

3.1 Schematic representation of a general 6-dof cable-suspended parallel mechanism 68
3.2 Plane of the trajectory 77
3.3 Hypocycloid curve for $\theta_h = -\frac{4\pi}{3}$ and $n_h = 3$ 78
3.4 Hypocycloid curve connecting two points having $\psi_h = \frac{2\pi}{3}$ with one, two, and three arcs respectively 80
3.5 Schematic representation of the proposed rotational trajectory 82
3.6 Interference of two cables 92
3.7 Platform Interference 93
3.8 Cylindrical reference frame 98
3.9 Rotation with respect to the circumferential axis Y_c 98
3.10 Translational component of the example trajectory 101
3.11 Orientational component of the example trajectory 102
3.12 Computed tensions along the trajectory 102
3.13 Construction of the hypocycloid of variable amplitude 106

Liste des vidéos

Toutes les vidéos sont disponibles à l'adresse

https://robot.gmc.ulaval.ca/publications/these-de-doctorat

sous [47] Pascal Dion-Gauvin.

Chap1_3dofTransitionTrajectory.mp4 32
Chap2_3dofPointToPointTrajectory.mp4 60

Remerciements

Mes premiers remerciements vont à mon directeur de recherche et directeur du Laboratoire de Robotique de l'Université Laval, Clément Gosselin. Clément a très tôt reconnu mon penchant pour la recherche plus fondamentale en robotique et a su me concocter un projet doctoral à ma mesure. C'est avant tout parce que celui-ci était taillé pour moi que j'ai pu en faire un succès et m'épanouir autant pendant cette période. Également, je suis reconnaissant de la grande liberté que Clément m'a accordée dans la recherche et dans l'écriture, ce qui me permet aujourd'hui de tirer une grande fierté de mon parcours. Plus que ses compétences et son savoir, je retiendrai de Clément ses qualités humaines profondes, notamment sa capacité d'écoute, sa flexibilité et sa propension à faire confiance.

Également, je tiens à remercier le professionnel de recherche du Laboratoire de Robotique Simon Foucault, qui a piloté la phase expérimentale du projet. Sans son apport précieux, cette phase aurait été beaucoup plus longue, ennuyeuse et ardue.

Enfin, je remercie ma famille, qui a toujours été présente pour moi.

Avant-propos

Cette thèse est l'achèvement de travaux effectués en vue de l'obtention du diplôme de Doctorat en génie mécanique. Elle est présentée sous forme d'une thèse par articles, c'est-à-dire que chaque chapitre est constitué d'un article que l'auteur de cette thèse a rédigé à titre de premier auteur. Ces articles ont toutefois été modifiés par rapport à la version apparaissant dans les publications afin d'en uniformiser la notation, de compléter certaines explications ou de clarifier certaines notions.

Le Chapitre 1 consiste en l'article de journal *Trajectory planning for the static to dynamic transition of point-mass cable-suspended parallel mechanisms*. Cet article a été publié dans le journal *Mechanism and Machine Theory* le 23 mars 2017 (Dion-Gauvin and Gosselin, 2017). L'intégralité des travaux théoriques présentés dans cet article, de même que la rédaction complète du corps de l'article, de la conclusion et de l'abstract, ont été effectuées par l'auteur de cette thèse. Le professeur Clément Gosselin, coauteur de l'article, a rédigé l'introduction en plus de réviser l'article en profondeur. Finalement, le professionnel de recherche Simon Foucault a piloté la phase expérimentale du projet. Dans un souci d'uniformité et pour éliminer tout risque d'ambiguité, la dérivation du modèle dynamique du mécanisme a été revue. Enfin, certaines définitions et tournures de phrases ont été simplifiées, et une figure a été ajoutée.

Le Chapitre 2 consiste en l'article de journal *Dynamic Point-to-Point Trajectory Planning of a Three-DOF Cable-Suspended Mechanism Using the Hypocycloid Curve*. Cet article a été publié dans le journal *IEEE/ASME Transactions on Mechatronics* le 31 mai 2018 (Dion-Gauvin and Gosselin, 2018). L'intégralité des travaux théoriques présentés dans cet article, de même que la rédaction complète de l'article, ont été effectuées par l'auteur de cette thèse. Le professeur Clément Gosselin, coauteur de l'article, a pour sa part révisé l'article en profondeur. Finalement, le professionnel de recherche Simon Foucault a piloté la phase expérimentale du projet. Dans un souci d'uniformité et pour éliminer tout risque d'ambiguité, la dérivation du modèle dynamique du mécanisme a été revue et la notation mathématique a été ajustée. Enfin, une figure a été corrigée.

Le Chapitre 3 consiste en l'article de journal *Beyond-the-static-workspace point-to-point trajectory planning of a 6-DoF cable-suspended mechanism using oscillating SLERP*. Cet article a été publié dans le journal *Mechanism and Machine Theory* le 11 mai 2022 (Dion-Gauvin

and Gosselin, 2022). L'intégralité des travaux théoriques présentés dans cet article, de même que la rédaction complète du corps de l'article, ont été effectuées par l'auteur de cette thèse. Le professeur Clément Gosselin, coauteur de l'article, a pour sa part rédigé le résumé anglais, l'introduction et la conclusion en plus de réviser l'article en profondeur. Finalement, l'étudiant Jérôme Landuré a contribué au développement de la technique de détection d'interférences entre deux câbles. Pour corriger certaines lacunes, une nouvelle technique de détection d'interférences entre un câble et la plate-forme est proposée dans cette thèse. De plus, dans un souci d'uniformité et pour éliminer tout risque d'ambiguité, la notation mathématique a été ajustée. Enfin, le résumé anglais a été remanié et certaines phrases ont été réécrites.

P. Dion-Gauvin and C. Gosselin. Trajectory planning for the static to dynamic transition of point-mass cable-suspended parallel mechanisms. *Mechanism and Machine Theory*, 113 : 158–178, 07 2017. doi:10.1016/j.mechmachtheory.2017.03.003.

P. Dion-Gauvin and C. Gosselin. Dynamic point-to-point trajectory planning of a three-dof cable-suspended mechanism using the hypocycloid curve. *IEEE/ASME Transactions on Mechatronics*, 23(4) :1964–1972, 2018. doi:10.1109/TMECH.2018.2840051.

P. Dion-Gauvin and C. Gosselin. Beyond-the-static-workspace point-to-point trajectory planning of a 6-dof cable-suspended mechanism using oscillating SLERP. *Mechanism and Machine Theory*, 174 :104894, 2022. ISSN 0094-114X. doi:10.1016/j.mechmachtheory.2022.104894.

Introduction

Contexte de la thèse

D'une façon générale, le robot le plus communément reconnu est le manipulateur sériel, qui se retrouve par exemple de manière omniprésente sur les chaînes d'assemblage dans l'industrie automobile. Ce type de robot bénéficie d'un espace de travail relativement grand puisque ses membrures sont jointes l'une à la suite de l'autre le long de la même chaîne cinématique. En contrepartie, il ne peut générer de grandes vitesses et accélérations car les lourds actionneurs placés à ses articulations doivent être déplacés lors de la mise en mouvement de l'effecteur. Outre le manipulateur sériel, le mécanisme le plus présent dans l'industrie est le robot parallèle, qui est constitué de plusieurs chaînes cinématiques en parallèle connectées à un même effecteur. Ce type de mécanisme constitue par exemple une partie intégrante des simulateurs de vols en aviation. En comparaison avec le robot sériel, le mécanisme parallèle dispose d'un plus petit espace de travail pour des membrures de mêmes dimensions parce que cet espace de travail est limité par la combinaison des restrictions de mobilité de chacune de ses chaînes cinématiques. En revanche, ce type de manipulateur est généralement en mesure de produire de grandes vitesses et accélérations puisque les actionneurs peuvent être fixés à la base du mécanisme et donc demeurer immobiles lors du déplacement de l'effecteur.

Un troisième type de mécanisme, le mécanisme parallèle entraîné par câbles, peut être vu comme regroupant à la fois l'avantage du mécanisme sériel et celui du mécanisme parallèle. Un mécanisme parallèle entraîné par câbles consiste en un effecteur attaché à des câbles qui est mis en mouvement par l'enroulement et le déroulement contrôlés de ces câbles sur leur bobine. D'une part, l'aspect filiforme des câbles et leur mécanisme d'enroulement sur l'enrouleur permettent d'assembler des mécanismes à câbles pourvus de grands espaces de travail, reproduisant ainsi l'avantage du mécanisme sériel. D'autre part, la masse négligeable des câbles de même que la disposition des enrouleurs et actionneurs à la base du mécanisme permettent aux actionneurs de générer, à l'instar du robot parallèle, de grandes vitesses et accélérations de l'effecteur. En contrepartie, les câbles ne pouvant résister à des forces de compression, seules des forces de tension peuvent leur être transmises. Cette problématique est incontournable et doit invariablement être résolue chaque fois que des mécanismes à câbles sont mis à contribution.

L'une des avenues privilégiées pour garantir l'unilatéralité des forces dans les câbles tout en assurant un minimum de controllabilité de l'effecteur consiste à utiliser un nombre de câbles—et d'actionneurs—plus grand que le nombre de degrés de liberté de l'effecteur. D'ailleurs, Kurtz and Hayward (1991) ont démontré que $n+1$ cables suffisent pour complètement contraindre un effecteur entraîné par câbles à n degrés de liberté. En revanche, un tel mécanisme comportant une redondance d'actionnement, des forces internes considérables peuvent être générées et une gestion de la distribution de celles-ci dans les membrures doit en être faite, ce qui complexifie la commande du robot. Pour éviter une telle gestion, une autre approche permettant de garantir l'unilatéralité des forces dans les câbles tout en assurant un minimum de contrôllabilité de l'effecteur consiste à utiliser un nombre de câbles correspondant au nombre de degrés de liberté de la tâche à accomplir et à tirer profit de la force gravitationnelle exercée sur l'effecteur pour maintenir les câbles sous tension. De tels mécanismes sont appelés mécanismes parallèles à câbles suspendus.

Les mécanismes parallèles à câbles suspendus sont, dans la plupart des cas répertoriés dans la littérature et dans l'industrie, conçus pour travailler en condition statique ou quasi-statique. Dans ce mode de fonctionnement, l'effecteur se déplace incrémentalement de pose d'équilibre statique en pose d'équilibre statique, maintenant ainsi les câbles sous tension en tout temps. Les applications les plus notables de mécanismes à câbles suspendus que sont la SkyCam (Cone, 1985), le RoboCrane NIST (Albus et al., 1993) et le radio-télescope FAST (Zi et al., 2008), peuvent toutes opérer en condition statique ou quasi-statique. Toutefois, ce mode de fonctionnement confine l'espace de travail de l'effecteur à l'ensemble des poses d'équilibre statique du mécanisme, lequel est limité par l'emprise des points d'attaches des enrouleurs à la base du mécanisme.

Plus récemment, les mécanismes parallèles à câbles suspendus ont été envisagés comme pouvant être opérés à des vitesses et accélérations non négligeables. Ce nouveau mode d'opération mène au concept d'espace de travail dynamique d'un mécanisme à câbles (Barrette and Gosselin, 2005), lequel correspond à l'ensemble des poses que l'effecteur peut atteindre en maintenant tous les câbles sous tension, que sa vitesse ou son accélération soit nulle ou non. Ainsi, puisque selon ce concept il n'est plus nécessaire que l'effecteur se trouve en état d'équilibre statique pour être complètement contrôlé, celui-ci a accès à un éventail beaucoup plus large de poses. Évidemment, les poses situées à l'extérieur de l'espace de travail statique du mécanisme peuvent seulement être atteintes avec une accélération non-nulle, alors que les poses appartenant à l'espace de travail statique peuvent aussi bien être atteintes avec une accélération nulle que non-nulle.

Cette notion d'espace de travail dynamique a naturellement mené à la planification de trajectoires de type pendule par des mécanismes suspendus possédant moins d'actionneurs que de degrés de liberté, c'est-à-dire sous-actionnés (Lefrançois and Gosselin, 2010; Zanotto et al., 2011). Dans cette approche, des trajectoires analytiques sont prescrites pour les variables ar-

ticulaires qui sont actionnées. Les trajectoires des variables articulaires non-actionnées, pour leur part, sont obtenues par l'intégration numérique en temps réel des équations différentielles du mouvement associées aux variables non-actionnées. Enfin, l'atteinte du point final ciblé est assurée par une optimisation (minimisation) entre la valeur prédite par l'intégration numérique et sa valeur désirée, laquelle fonction de minimisation est bonifiée de fonctions de pénalité garantissant le respect des contraintes inviolables du mécanisme, telles les contraintes de tension dans les câbles, les limites articulaires ainsi que les limites de couple aux actionneurs. Une telle procédure permet l'atteinte d'une pose finale désirée même si la trajectoire de l'effecteur ne peut être imposée en tout instant en raison du sous-actionnement du mécanisme.

Pour se soustraire à une planification de trajectoire et un schéma de commande d'une telle complexité, il a été proposé de réaliser les trajectoires de type pendule au moyen de mécanismes à câbles suspendus complètement actionnés, c'est-à-dire comptant autant d'actionneurs que de degrés de liberté. Dans cette approche, les trajectoires sont définies dans le repère global sous forme paramétrique et, puisque chaque degré de liberté peut être contrôlé, la contrainte de tension dans les câbles est vérifiée par la simple substitution de la trajectoire et de ses dérivées dans le modèle dynamique du mécanisme. Comme introduction à cette nouvelle approche, des trajectoires périodiques décrivant des mouvements linéaires ou elliptiques ont d'abord été développées pour des mécanismes à 2 ddl (Gosselin et al., 2012), à 3 ddl spatiaux (Gosselin, 2013), puis à 6 ddl (Jiang et al., 2018b). Ces travaux ont entre autres permis de démontrer que certaines trajectoires périodiques pouvaient atteindre des amplitudes de mouvement théoriquement infinies lorsque réalisées à la fréquence naturelle du pendule simple équivalent. Par la suite, en raison de leur plus grand potentiel d'applications pratiques, les trajectoires dites de type point à point, qui sont employées pour relier deux poses cibles à vitesse instantanée nulle sans égard au chemin emprunté par l'effecteur, ont été investiguées pour des mécanismes à 2 ddl (Gosselin and Foucault, 2014), à 3 ddl (Jiang and Gosselin, 2016), puis à 6 ddl (Jiang et al., 2018a). C'est dans ce contexte que s'inscrit la présente thèse.

Objectifs de la thèse

L'objectif de ce travail de recherche est de développer des trajectoires analytiques de type point à point pour les mécanismes à câbles suspendus complètement actionnés. Tel que mentionné précédemment, les trajectoires de type point à point trouvent leur utilité dans des applications qui requièrent de relier deux poses données à vitesse instantanée nulle et pour lesquelles le chemin spécifique emprunté pour relier ces deux poses n'est d'aucune importance. Par ailleurs, ce type de trajectoire étant habituellement employé pour relier plusieurs poses cibles en séquence, il importe d'assurer la continuité de l'accélération aux points limites afin d'éviter l'introduction de discontinuités au niveau des efforts articulaires qui pourraient se traduire par des instabilités du mécanisme. Enfin, puisque dans cette thèse les trajectoires sont desti-

nées à être réalisées par des mécanismes à câbles suspendus, leur suivi doit, en tout instant, requérir exclusivement des forces de tension dans les câbles afin de pouvoir être exécutées. Cela se traduit notamment par la nécessité d'atteindre les poses cibles avec des accélérations instantanées non-nulles, dans la mesure où ces poses cibles pourraient ne pas appartenir à l'espace de travail statique du mécanisme. L'objectif principal de cette thèse consiste donc à développer des procédures de planification de trajectoires respectant ces contraintes qui permettent d'atteindre le plus grand nombre possible de poses cibles. Un chapitre de cette thèse est consacré à la planification de trajectoires point à point pour un mécanisme à effecteur ponctuel à 3 degrés de liberté, et un autre est consacré à la planification de trajectoires pour un mécanisme à 6 degrés de liberté de type Gough-Stewart.

Un objectif complémentaire de cette thèse est le développement de trajectoires analytiques dites point à point de transition reliant une pose au repos appartenant à l'espace de travail statique du mécanisme à une pose cible à accélération non-nulle. Ces trajectoires peuvent être utilisées pour joindre la première d'une série de poses cibles à atteindre ou, par l'inversion de la trajectoire, pour retourner l'effecteur au repos une fois toutes les poses cibles atteintes. Puisqu'il s'agit d'un cas particulier de trajectoires point à point, les trajectoires de transition doivent également satisfaire les conditions aux points limites de vitesse instantanée nulle et de continuité de l'accélération, de même que la contrainte de tension dans les câbles. Enfin, en raison de l'unilatéralité des forces dans les câbles, une attention particulière doit être accordée à la sélection de la pose au repos, en ce sens où elle doit constituer une pose d'équilibre statique de l'effecteur. Un chapitre de cette thèse est consacré au développement de trajectoires de transition pour des mécanismes à effecteur ponctuel à 2 et 3 degrés de liberté.

Méthodologie et organisation de la thèse

Les trajectoires développées se divisant en trois catégories, leur présentation se décline en autant chapitres dans cette thèse. Ces chapitres sont organisés en ordre croissant de complexité des trajectoires, soit de la trajectoire comptant le plus petit nombre de degrés de liberté à celle en comptant le nombre le plus grand. Cet ordre consiste également en l'ordre dans lequel elles ont été produites et en ordre chronologique de publication des articles.

Dans un premier temps, le Chapitre 1 propose une formulation analytique de trajectoire point à point de transition pour mécanismes à effecteur ponctuel à deux et à trois ddl. Dans la première section du chapitre, une formulation de trajectoire pour le mécanisme plan à effecteur ponctuel est articulée et il est validé que celle-ci respecte les contraintes cinématiques et dynamiques dans la plupart des inclinaisons. Puis, cette trajectoire est adaptée au mécanisme spatial à effecteur ponctuel, et les similarités et différences entre les expressions des deux mécanismes sont mises en évidence. Par la suite, le rôle joué par la fonction d'amplitude dans le maintien des tensions dans les câbles est discuté, laquelle discussion mène à l'établissement

de critères visant à en évaluer la performance. Enfin, ce chapitre se conclut avec la présentation des résultats de simulations de trajectoires-exemples qui illustrent l'impact de divers paramètres sur la faisabilité de la trajectoire.

Dans un second temps, le Chapitre 2 propose une formulation analytique de trajectoire point à point pour mécanismes à trois ddl à effecteur ponctuel. En premier lieu, une trajectoire respectant par construction les conditions cinématiques aux points limites est définie. Puis, à partir des expressions des tensions dans les câbles, des relations algébriques simples établissant la faisabilité de la trajectoire sont développées. Ce chapitre se conclut par une section présentant les résultats d'une trajectoire-exemple simulée.

Enfin, le Chapitre 3 dresse un portrait détaillé de la planification de trajectoires point à point pour mécanismes à câbles suspendus à six ddl complètement actionnés. Le coeur du chapitre consiste en la dérivation complète des composantes translationnelle et rotationnelle de la trajectoire analytique proposée. Puis, ce chapitre établit clairement la distinction entre les poses accessibles au mécanisme à câbles et celles atteignables par la trajectoire, et articule des stratégies pour respectivement les identifier. En complément, l'architecture du mécanisme hexapodal à privilégier est discutée et un système de coordonnées novateur permettant de visualiser plus intuitivement la configuration du mécanisme est présenté. Enfin, comme les autres chapitres, celui-ci se conclut avec une phase de simulation servant à démontrer l'applicabilité de la trajectoire proposée.

Bibliographie

J. Albus, R. Bostelman, and N. Dagalakis. The NIST Robocrane. *Journal of Robotic Systems*, 10(5) :709–724, 1993. ISSN 07412223. doi:10.1002/rob.4620100509.

G. Barrette and C. M. Gosselin. Determination of the dynamic workspace of cable-driven planar parallel mechanisms. *Journal of Mechanical Design, Transactions of the ASME*, 127 (2) :242–248, 2005. ISSN 10500472. doi:10.1115/1.1830045.

L. L. Cone. Skycam : An aerial robotic camera system. *Byte*, 10(10) :122–132, 1985. ISSN 03605280.

C. Gosselin. Global planning of dynamically feasible trajectories for three-dof spatial cable-suspended parallel robots. In T. Bruckmann and A. Pott, editors, *Cable-Driven Parallel Robots*, pages 3–22. Springer Berlin Heidelberg, Berlin, Heidelberg, 2013. ISBN 978-3-642-31988-4. doi:10.1007/978-3-642-31988-4_1.

C. Gosselin and S. Foucault. Dynamic point-to-point trajectory planning of a two-dof cable-suspended parallel robot. *IEEE Transactions on Robotics*, 30(3) :728 – 736, 2014. ISSN 1552-3098. doi:10.1109/TRO.2013.2292451.

C. Gosselin, P. Ren, and S. Foucault. Dynamic trajectory planning of a two-dof cable-suspended parallel robot. In *Proceedings of the IEEE International Confe-*

rence on Robotics and Automation, pages 1476–1481, St. Paul, MN, USA, 2012. doi:10.1109/ICRA.2012.6224683.

X. Jiang and C. Gosselin. Dynamic point-to-point trajectory planning of a three-dof cable-suspended parallel robot. *IEEE Transactions on Robotics*, 32(6) :1550–1557, Dec 2016. ISSN 1552-3098. doi:10.1109/TRO.2016.2597315.

X. Jiang, E. Barnett, and C. Gosselin. Dynamic point-to-point trajectory planning beyond the static workspace for six-dof cable-suspended parallel robots. *IEEE Transactions on Robotics*, 34(3) :781–793, 2018a. doi:10.1109/TRO.2018.2794549.

X. Jiang, E. Barnett, and C. Gosselin. Periodic trajectory planning beyond the static workspace for 6-dof cable-suspended parallel robots. *IEEE Transactions on Robotics*, 34(4) : 1128–1140, 2018b. doi:10.1109/TRO.2018.2819668.

R. Kurtz and V. Hayward. Dexterity measure for tendon actuated parallel mechanisms. In *Proceedings of the Fifth International Conference on Advanced Robotics*, volume 2, pages 1141 – 1146, 07 1991. ISBN 0-7803-0078-5. doi:10.1109/ICAR.1991.240402.

S. Lefrançois and C. Gosselin. Point-to-point motion control of a pendulum-like 3-dof underactuated cable-driven robot. In *Proceedings of the IEEE International Conference on Robotics and Automation*, pages 5187–5193, Anchorage, AK, USA, 2010. doi:10.1109/ROBOT.2010.5509656.

D. Zanotto, G. Rosati, and S. Agrawal. Modeling and control of a 3-dof pendulum-like manipulator. In *Proceedings of the IEEE International Conference on Robotics and Automation*, pages 3964–3969, Shanghai, China, 2011. doi:10.1109/ICRA.2011.5980198.

B. Zi, B. Duan, J. Du, and H. Bao. Dynamic modeling and active control of a cable-suspended parallel robot. *Mechatronics*, 18(1) :1 – 12, 2008. doi:10.1016/j.mechatronics.2007.09.004.

Chapitre 1

Trajectory planning for the static to dynamic transition of point-mass cable-suspended parallel mechanisms

1.1 Résumé

Cet article présente une formulation de trajectoire reliant un point inital au repos à un point final à joindre à vitesse nulle et à accélération non-nulle pour des mécanismes à câbles suspendus à effecteur ponctuel à 2 et à 3 ddl. La trajectoire est conçue pour atteindre le premier d'une séquence de points cibles qui peuvent être positionnés à l'extérieur de l'espace de travail statique des mécanismes. Les planifications proposées consistent en des oscillations rectilignes d'amplitude progressivement croissante centrées au point initial, où le nombre minimal d'oscillations de la trajectoire est déterminé de manière à assurer des forces exclusivement de tension dans tous les câbles tout au long du mouvement. Il est prouvé que ce nombre d'oscillations peut être trouvé pour toute trajectoire se trouvant entièrement sous les enrouleurs. Cet article pose un nouveau regard sur la dynamique des mécanismes à câbles suspendus à 3 ddl, et met en exergue les similarités et différences entre les trajectoires à 2 et à 3 ddl. Des résultats de simulation d'une trajectoire exemple sont présentés afin d'illustrer l'approche proposée, et une démonstration vidéo d'une validation expérimentale réalisée sur un prototype à 3 ddl est incluse.

1.2 Abstract

This paper presents a trajectory formulation that connects an initial point at rest to a final point to be reached with zero velocity but nonzero acceleration for planar two-dof and spatial

three-dof cable-suspended mechanisms with point-mass end-effectors. The trajectory is designed to reach the first of a sequence of target points that can be located outside of the static workspace of the mechanisms. The proposed motion consists of oscillations of progressively increasing amplitude centred at the initial point, whereby an expression for the minimum feasible number of oscillations is determined by ensuring positive tension in all cables throughout the trajectory. It is shown that this number of oscillations can be found for any trajectory that is entirely located below the spools. The paper provides novel insight into the dynamics of the three-dof mechanism, and highlights the similarities and differences between the planar and spatial motions. Simulation results of example trajectories are included in order to illustrate the approach, along with a video demonstration of an experimental validation performed using a three-dof prototype.

1.3 Introduction

A cable-suspended parallel mechanism consists of a platform that is suspended by cables, and that is put into motion by the winding and unwinding of these cables on their respective servo-controlled winch. Unlike fully constrained cable-driven parallel mechanisms that have more cables than dofs (see for instance Lim et al., 2009; Gouttefarde et al., 2008; and many others), cable-suspended mechanisms have the same number of cables as dofs and rely on gravity to maintain tension in the cables. Cable-suspended parallel mechanisms can be used in applications that require very large workspaces, such as cranes (Albus et al., 1993) or camera support systems (Cone, 1985). Examples of some of the first cable-suspended mechanisms are presented in Alp and Agrawal (2002); Pusey et al. (2004); Bouchard and Gosselin (2010).

In most cases reported in the literature, cable-suspended mechanisms are assumed to work in static or quasi-static conditions, which implies that their workspace—referred to as the static workspace (Riechel and Ebert-Uphoff, 2004)—is limited by the footprint of the mechanism.

However, using the notion of dynamic workspace (Barrette and Gosselin, 2005), it is possible to envision the dynamic control of cable-suspended parallel mechanisms. The dynamic workspace is defined as the set of poses that the platform can reach with a controlled kinematic state (position, velocity and acceleration) while maintaining all cables under tension. Clearly, poses beyond the static workspace can only be reached with a nonzero acceleration, while poses in the static workspace can be reached with either zero or nonzero accelerations.

In this context, an elementary task that cable-suspended mechanisms must be able to perform consists in connecting two target points that are located outside of their static workspace with a zero instantaneous velocity at each of the points. Dynamic point-to-point trajectory planning aims at developing path-finding procedures that satisfy these boundary conditions while maintaining cable tension throughout the motion.

Trajectory planning techniques for underactuated cable-suspended mechanisms were proposed in Cunningham and Asada (2009); Lefrançois and Gosselin (2010); Zanotto et al. (2011); Zoso and Gosselin (2012). These techniques require the online numerical integration of the complex dynamic equations. On the other hand, the trajectory planning of fully actuated cable-suspended mechanisms is much simpler since it can be accomplished using algebraic relationships. Based on such relationships, periodic trajectories were developed in the literature for a two-dof planar mechanism with a point-mass end-effector (Gosselin et al., 2012), for a three-dof spatial mechanism with a point-mass end-effector (Gosselin, 2013), and then for a specific architecture of a planar three-dof mechanism (Jiang and Gosselin, 2014). Notably, the conditions that ensure trajectory feasibility presented in these publications lead to the discovery of a special frequency that can be regarded as the natural frequency of the mechanism, as shown in Jiang and Gosselin (2016). This approach was also used to develop dynamic point-to-point trajectories for a two-dof planar mechanism with a point-mass end-effector (Gosselin and Foucault, 2014). The dynamics of cable-suspended parallel mechanisms was also studied in Trevisani (2010); Schmidt et al. (2014); Zhang and Shang (2016); Berti et al. (2016).

In this paper, a dynamic trajectory planning framework is proposed for fully actuated planar two-dof and spatial three-dof cable-suspended mechanisms with point-mass end-effectors. The trajectory connects an initial point at rest to a final point to be reached with a dynamic state (nonzero acceleration). The proposed motion consists of oscillations of progressively increasing amplitude centred at the initial point, whereby the minimum number of oscillations is determined to ensure positive tension in all cables throughout the trajectory.

This paper is arranged as follows. Section 1.4 presents, in the following order, the kinematic and dynamic modelling of the two-dof mechanism, the proposed transition trajectory, the condition ensuring its feasibility, the optimized minimum-time trajectory, and the reverse transition trajectory. Section 1.5 presents the same derivations for the spatial three-dof mechanism and highlights the similarities and differences between the planar and spatial motions. Section 1.6 addresses the amplitude function, which is an essential component of the proposed trajectory formulation. Section 1.7 provides simulation results of examples trajectories that illustrate the impact of some parameters on the motion. Finally, a video demonstrating the implementation on a prototype is provided in order to validate the proposed trajectory.

1.4 Planar Mechanism

1.4.1 Mechanism Modelling

The planar two-dof cable-suspended mechanism addressed in this study is represented schematically in Fig. 1.1. It consists of two actuated spools mounted on a fixed structure which are used to control the extension of two massless cables with infinite stiffness. The cables are attached to a common end-effector which is considered as a point-mass. By controlling the

extension of the two cables, the position of the point-mass can be controlled. The mechanism has two actuators and two dofs and is therefore fully actuated. However, because the cables can only work in tension (they cannot push), constraints must be imposed on the Cartesian trajectory prescribed at the end-effector. The static workspace of the mechanism, i.e., the portion of the Cartesian space in which the end-effector can be brought to rest, is limited by vertical lines passing through the cable attachment points on the structure.

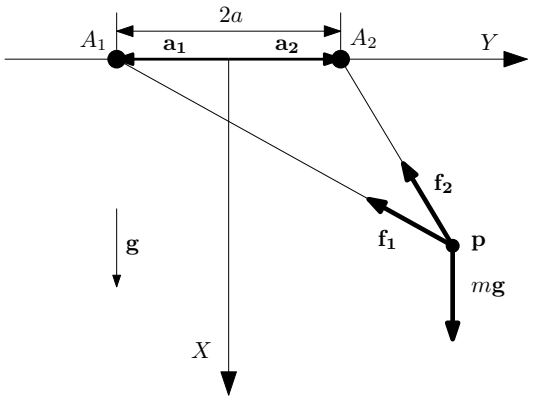

Figure 1.1 – Planar two-dof cable-suspended mechanism.

Referring to the two-dof cable-suspended mechanism of Fig. 1.1, a fixed reference frame is defined on the base of the mechanism, whose origin is located on the line that connects the spool output points and at an equal distance from these points. The Y axis is defined along this line which is assumed to be horizontal and the X axis is vertical, pointing downward. The distance between the spool output points is noted $2a$. The (constant) position vectors of these points can then be written as $\mathbf{a}_1 = \begin{bmatrix} 0 & a \end{bmatrix}^T$ and $\mathbf{a}_2 = \begin{bmatrix} 0 & -a \end{bmatrix}^T$. The position vector of the end-effector point-mass m is noted $\mathbf{p} = \begin{bmatrix} x & y \end{bmatrix}^T$. The cable lengths, i.e., the joint coordinates, are respectively noted ρ_1 and ρ_2. The inverse kinematic model of the mechanism is written as

$$\rho_k = \sqrt{(\mathbf{a}_k - \mathbf{p})^T(\mathbf{a}_k - \mathbf{p})}, \quad k = 1, 2. \tag{1.1}$$

Since the mass and elasticity of the cables are neglected, the dynamic model of the mechanism is obtained by considering the force balance on the point-mass end-effector, namely

$$\sum_{k=1}^{2} \left(\frac{\mathbf{a}_k - \mathbf{p}}{\rho_k} \right) f_k + m\mathbf{g} = m\ddot{\mathbf{p}}, \tag{1.2}$$

where f_k is the tension in cable k, and $\mathbf{g} = \begin{bmatrix} g & 0 \end{bmatrix}^T$ is the vector of gravitational acceleration. Equation (1.2) can be rewritten in matrix form as

$$\mathbf{M}\boldsymbol{\mu} = \ddot{\mathbf{p}} - \mathbf{g}, \tag{1.3}$$

with

$$\boldsymbol{\mu} = \frac{1}{m}\begin{bmatrix} \dfrac{f_1}{\rho_1} & \dfrac{f_2}{\rho_2} \end{bmatrix}^T, \tag{1.4}$$

and where matrix $\mathbf{M}$ is defined as

$$\mathbf{M} = \begin{bmatrix} \boldsymbol{\rho}_1 & \boldsymbol{\rho}_2 \end{bmatrix}, \tag{1.5}$$

with

$$\boldsymbol{\rho}_k = \mathbf{a}_k - \mathbf{p}, \qquad k = 1, 2. \tag{1.6}$$

Solving eq. (1.3) for vector $\boldsymbol{\mu}$ yields expressions for the cable forces, which must be positive to ensure dynamically feasible trajectories. One obtains

$$\boldsymbol{\mu} = \mathbf{M}^{-1}(\ddot{\mathbf{p}} - \mathbf{g}) \succeq \mathbf{0}, \tag{1.7}$$

where $\succeq$ stands for the componentwise inequality. The inverse of matrix $\mathbf{M}$ appearing in eq. (1.7) is given by

$$\mathbf{M}^{-1} = \frac{\mathrm{Adj}(\mathbf{M})}{\det(\mathbf{M})}, \tag{1.8}$$

where $\mathrm{Adj}\,(\mathbf{M})$ stands for the adjoint matrix of $\mathbf{M}$ and $\det\,(\mathbf{M})$ is its determinant. Referring to eq. (1.5), the latter is given by

$$\det\,(\mathbf{M}) = \boldsymbol{\rho}_2^T \mathbf{E} \boldsymbol{\rho}_1, \tag{1.9}$$

where $\mathbf{E}$ is the $90°$ rotation matrix, namely

$$\mathbf{E} = \begin{bmatrix} 0 & -1 \\ 1 & 0 \end{bmatrix}. \tag{1.10}$$

It can be noted, from eq. (1.9), that the determinant is positive as long as the end-effector remains below the straight line passing through the fixed cable spools. This assumption is used here to simplify the positive tension constraints (1.7), yielding

$$\boldsymbol{\kappa} = \mathrm{Adj}(\mathbf{M})(\ddot{\mathbf{p}} - \mathbf{g}) \succeq \mathbf{0}, \tag{1.11}$$

where the quantities $\boldsymbol{\kappa} = \begin{bmatrix} \kappa_1 & \kappa_2 \end{bmatrix}^T$, referred to as pseudotensions, bear the same sign as the cable tensions and are introduced to simplify the analysis. Referring to eq. (1.5), the adjoint matrix of $\mathbf{M}$ is given by

$$\mathrm{Adj}(\mathbf{M}) = \begin{bmatrix} \boldsymbol{\rho}_2^T \mathbf{E} \\ -\boldsymbol{\rho}_1^T \mathbf{E} \end{bmatrix}, \tag{1.12}$$

and hence the pseudotensions can be written as

$$\kappa_1 = \ (\mathbf{a}_2 - \mathbf{p})^T \mathbf{E}(\ddot{\mathbf{p}} - \mathbf{g}) \ > 0 \tag{1.13}$$

$$\kappa_2 = -(\mathbf{a}_1 - \mathbf{p})^T \mathbf{E}(\ddot{\mathbf{p}} - \mathbf{g}) > 0. \tag{1.14}$$

Therefore, satisfying the above inequalities at all points of a given trajectory ensures that the cables remain under tension throughout the trajectory. These conditions are necessary and sufficient and their simple form allows for trajectory planning. They are written, in scalar form, as (Gosselin et al., 2012)

$$\kappa_1 = -(a+y)(\ddot{x}-g) + x\ddot{y} > 0 \tag{1.15}$$

$$\kappa_2 = -(a-y)(\ddot{x}-g) - x\ddot{y} > 0. \tag{1.16}$$

1.4.2 The pendulum constraint

In Fig. 1.2, the pseudotension constraints of eq. (1.15) and (1.16) are represented schematically in the $\ddot{x}-\ddot{y}$ plane for a given position $\mathbf{p} = \begin{bmatrix} x & y \end{bmatrix}^T$ of the end-effector. The unbounded feasible region, i.e., the set of kinematic states for which both cables are under tension, is represented by the shaded area, which is defined by the lines corresponding to the constraints. As it can be observed, the constraints intersect at point $\ddot{\mathbf{p}} = \begin{bmatrix} g & 0 \end{bmatrix}^T$ regardless of the position of the end-effector.

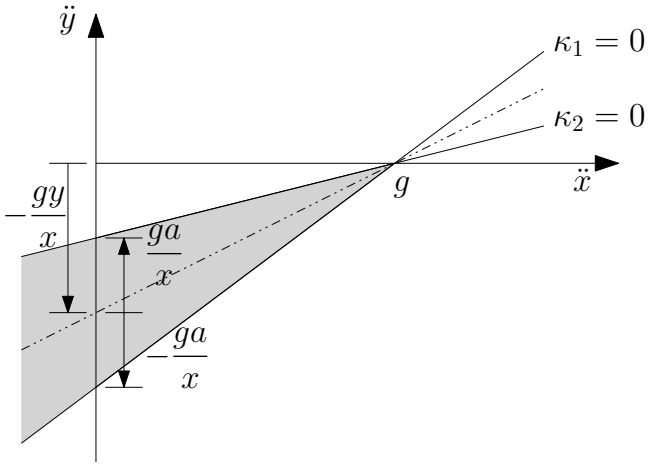

Figure 1.2 – Pseudo-tension constraints.

The triangle defined by the lines corresponding to the constraints and a given constant vertical acceleration $\ddot{x}$ has a median passing by point $(g, 0)$ that is illustrated by a dashed line in Fig. 1.2. Its equation can be written as

$$\frac{\ddot{x}-g}{x} = \frac{\ddot{y}}{y}. \tag{1.17}$$

From a physical point of view, eq. (1.17) is the dynamic model, written in Cartesian coordinates, of a simple pendulum suspended from the centroid of the cable spools. Considering the form of eqs. (1.15) and (1.16), it corresponds to the limit of either one of the pseudotensions when a goes to zero. The latter statement implies that a kinematic state satisfying eq. (1.17) has equal pseudotensions, of value $\kappa = a(\ddot{x}-g)$. Additionally, it can be shown that for such

a kinematic state, the resulting force produced by both cables is directed toward the centroid of the cable spools, at the centre of the positive tension sector defined by the two cables. Finally, according to the definition of a median, a kinematic state satisfying eq. (1.17) is located at equal distance from the two lines of zero tension for a given vertical acceleration, i.e., it is located the farthest possible from the loci of zero tension. For all these reasons, end-effectors satisfying eq. (1.17) are the least likely to fall into negative tension states if an external disturbance were to occur and can thus be construed as dynamically stable as possible. Equation (1.17) can therefore be thought of as the locus of ideal kinematic states.

This equation can be put to good use in dynamic trajectory planning. Specifically, in a context of point-to-point trajectory planning constructed as a sequence of trajectory segments, eq. (1.17) can be imposed on endpoint kinematic states in order to maximize the likelihood of obtaining feasible subsequent trajectory segments. In this regard, it generalizes the condition imposed on endpoint kinematic states put forward in Gosselin and Foucault (2014), thereby extending the dynamic workspace of the mechanism for a given initial kinematic state. This constraint is used here in the trajectory planning algorithm.

1.4.3 Static to Dynamic Transition Trajectory Planning

The static to dynamic transition trajectory connects an initial point at rest in the static workspace of the mechanism to a target point in the dynamic workspace. Let $\mathbf{p}_0 = \begin{bmatrix} x_0 & y_0 \end{bmatrix}^T$ be the coordinates of the initial (static) kinematic state. Since static kinematic states can be easily connected through quasi-static motions, the location within the static workspace of the initial point does not have to be prescribed from the outset. However, using eq. (1.17) to maximize the likelihood of obtaining a feasible trajectory yields $y_0 = 0$, while x_0 remains undetermined. The prescribed position of the final (dynamic) kinematic state, to be reached with a zero intantaneous velocity, is noted by vector $\mathbf{p}_1 = \begin{bmatrix} x_1 & y_1 \end{bmatrix}^T$. As shown schematically in Fig. 1.3, the proposed motion connecting point $\mathbf{p}_0$ to point $\mathbf{p}_1$ consists of progressively increasing oscillations centred at the initial point, along a straight line passing through the initial and final points.

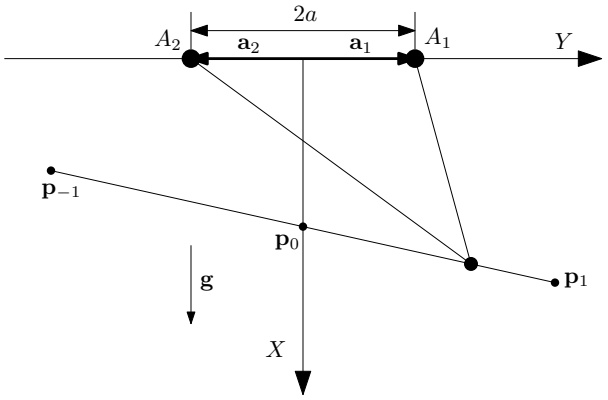

Figure 1.3 – Static to dynamic rectilinear transition trajectory.

The point located on the opposite side of the (vertical) X axis and at the same distance from the X axis as point $\mathbf{p}_1$, along the trajectory, is noted $\mathbf{p}_{-1}$, and its coordinates can be written as:

$$\mathbf{p}_{-1} = \begin{bmatrix} 2x_0 - x_1 \\ -y_1 \end{bmatrix}. \tag{1.18}$$

Observing that this point must remain below the spools leads to a constraint on x_0, namely

$$x_0 > \frac{x_1}{2}. \tag{1.19}$$

One parametric trajectory formulation producing the proposed motion is

$$x(t) = s_x(t/T) \rightarrow \ s_x(\tau) = (x_1 - x_0)A(\tau)\cos(2\pi n\tau) + x_0 \tag{1.20}$$

$$y(t) = s_y(t/T) \rightarrow \ s_y(\tau) = y_1 A(\tau)\cos(2\pi n\tau), \tag{1.21}$$

with

$$\tau = \frac{t}{T}, \qquad 0 \leq t \leq T, \qquad 0 \leq \tau \leq 1 \tag{1.22}$$

where $A(\tau)$ is a non-decreasing amplitude function, t is the time, τ is the normalized time, T is the duration of the trajectory segment, and $n \in \mathbb{N}^+$ is the number of oscillations. The latter two variables are linked by the relation

$$\mathcal{T} = \frac{T}{n}, \tag{1.23}$$

where $\mathcal{T}$ is the period of one oscillation. The rectilinear trajectory must meet initial conditions representing the initial state of rest that can be written as

$$x(0) = x_0, \qquad \dot{x}(0) = \ddot{x}(0) = 0, \qquad y(0) = \dot{y}(0) = \ddot{y}(0) = 0, \tag{1.24}$$

while the final conditions are given by

$$x(T) = x_1, \qquad y(T) = y_1, \qquad \dot{x}(T) = \dot{y}(T) = 0, \tag{1.25}$$

and

$$\frac{\ddot{x}(T) - g}{x(T)} = \frac{\ddot{y}(T)}{y(T)}, \tag{1.26}$$

where eq. (1.17) is used on the final kinematic state to produce eq. (1.26). Eqs. (1.24)–(1.25) lead to conditions on the amplitude function, namely

$$A(0) = 0 \qquad A'(0) = 0 \qquad A''(0) = 0 \tag{1.27}$$

$$A(1) = 1 \qquad A'(1) = 0, \tag{1.28}$$

while eq. (1.26) yields an expression for T^2, namely

$$T^2 = \frac{x_0}{g}(4\pi^2 n^2 - A''(1)). \tag{1.29}$$

Therefore, the amplitude function can be any smooth function on the interval $\tau \in [0, 1]$ that matches eqs. (1.27) and (1.28). In addition, eq. (1.29) must be positive-definite, yielding

$$n^2 > \frac{A''(1)}{4\pi^2}, \tag{1.30}$$

which is necessarily satisfied if the amplitude function is non-decreasing on the considered time interval (since the latter implies $A''(1) \leq 0$).

1.4.4 Positive-Tension Constraint

As shown above, the selection of a proper amplitude function ensures that the parametric trajectory defined by eqs. (1.20) and (1.21) meets all endpoint kinematic conditions. However, it is left to verify that the tensions in the cables remain positive throughout the trajectory. To this end, the parametric trajectory and its time derivatives are substituted into the pseudotensions, eqs. (1.15) and (1.16). Eq. (1.29) is thereafter substituted into the resulting expressions to eliminate T^2, yielding pseudotensions depending only on two parameters, namely x_0 and n. Then, using the substitutions

$$\widehat{\kappa}_k = \frac{\kappa_k}{ga}, \qquad \widehat{y}_1 = \frac{y_1}{a}, \qquad v = \frac{x_1 - x_0}{x_0}, \tag{1.31}$$

the (normalized) pseudotensions can be written as

$$\widehat{\kappa}_k = 1 - C_k \cos(2\pi n\tau) + S_k \sin(2\pi n\tau), \qquad k = 1, 2. \tag{1.32}$$

In the above expressions, coefficients C_k and S_k, $k = 1, 2$, are given by

$$C_k = \frac{(v + w_k)c(\tau)}{4\pi^2 n^2 - A''(1)} - vA(\tau) \tag{1.33}$$

$$S_k = \frac{4\pi n(v + w_k)s(\tau)}{4\pi^2 n^2 - A''(1)}, \tag{1.34}$$

with

$$c(\tau) = A''(\tau) - A(\tau)A''(1) \tag{1.35}$$

$$s(\tau) = A'(\tau), \tag{1.36}$$

and with

$$w_1 = -\widehat{y}_1, \qquad\qquad w_2 = \widehat{y}_1. \tag{1.37}$$

The linear combination of the sine and cosine functions in eqs. (1.32) can be rewritten as

$$\widehat{\kappa}_k = 1 + \sqrt{C_k^2 + S_k^2}\cos(2\pi n\tau + \phi_k), \qquad k = 1, 2, \tag{1.38}$$

where ϕ_k, $k = 1, 2$, are phase shifts. Given the bounds on trigonometric functions, the normalized pseudotensions are positive definite if

$$\widehat{\kappa}_{e,k} = 1 - \sqrt{C_k^2 + S_k^2} > 0, \qquad k = 1, 2. \tag{1.39}$$

The above expressions represent the time-dependent lower envelope of the normalized pseudotensions. On the considered time interval, these inequalities constitute a sufficient (but not necessary) condition for positive cable tension. Using the substitution

$$N \equiv n^2, \tag{1.40}$$

condition (1.39) depends solely on two parameters, namely v and N. These expressions are used extensively in this study to assess the feasibility of the proposed trajectory defined above.

Trajectory Feasibility

The inequality constraints derived in the preceding section can be used to determine the least constraining value of parameters v and N that ensures positive cable tensions throughout the trajectory. In this regard, one could reflect that the longer it takes for the trajectory to reach its final amplitude, the more likely the cables are to remain under tension. Referring to eq. (1.23), this proposition suggests that positive cable tensions are more likely to occur as T and n approach infinity, but as $\mathcal{T}$ remains in $\mathbb{R}$. Therefore, computing the limit of eqs. (1.39) as N approaches infinity yields

$$\lim_{N\to\infty} \widehat{\kappa}_{e,1} = \lim_{N\to\infty} \widehat{\kappa}_{e,2} = 1 - A(\tau)|v| > 0. \tag{1.41}$$

The left-hand side of the above inequality reaches its minimum value over the considered time interval at the amplitude function's maximum point, i.e., at $\tau = 1$ where $A''(1) = 1$. Ensuring that this minimum is positive definite leads to an interval on v, namely:

$$|v| < 1. \tag{1.42}$$

The latter expression can be rewritten as

$$0 < \frac{x_1}{x_0} < 2, \tag{1.43}$$

which merely consists of eq. (1.19) along with assumptions $x_0 > 0$ and $x_1 > 0$. In other words, a number of oscillations n can always be chosen large enough to ensure the feasibility of the trajectory provided that points $\mathbf{p}_1$ and $\mathbf{p}_{-1}$ are located below the spools. Therefore, ensuring positive cable tensions throughout the proposed trajectory introduces no additional geometric constraints to those previously assumed.

Trajectory with the Minimum Feasible Number of Oscillations for a Given Inclination v

Although there always exists a number of oscillations sufficiently large that guarantees the feasibility of the trajectory provided it is entirely located below the spools, in practice it may be desirable to determine the minimum value of N as a function of the inclination v that can be used while satisfying the constraints of cable tensions, eqs. (1.39). These constraints define in the $vN-$plane a feasible region that contains the set of points (v, N) that produce feasible trajectories. Therefore, the minimum feasible value of N as a function of v is found at the boundary of this feasible region, and can be obtained by setting both ineqs. (1.39) to zero. Then, each of these equalities is multiplied by its always-positive conjugate (to eliminate the square-root) and by the resulting always-positive denominator. Two quadratic equations in N, each yielding two possible solutions, are thereby produced. Since arbitrarily large numbers of oscillations ensure feasible trajectories, the feasible region contains arbitrarily large values of N and is unbounded. Therefore, the minimum feasible value of N as a function of v corresponds to the feasible region's lower boundary and belongs to one of the two branches of solution corresponding to the *largest* root of both quadratic equations. The two branches of solution can thus be written as:

$$N_k(v, \tau) = \frac{-E_k + \sqrt{E_k^2 - DF_k}}{4\pi^2 D}, \qquad k = 1, 2, \tag{1.44}$$

where

$$D = 1 - A(\tau)^2 v^2 \tag{1.45}$$

$$E_k = A(\tau)A''(\tau)v^2 - A''(1) - 2s(\tau)^2(v + w_k)^2 + c(\tau)A(\tau)vw_k \tag{1.46}$$

$$F_k = A''(1)^2 - c(\tau)^2 {w_k}^2 - A''(\tau)^2 v^2 - 2c(\tau)A''(\tau)vw_k. \tag{1.47}$$

Eqs. (1.44) represent the time-dependent zero-tension locus of each cable. For any time $\tau \in [0, 1]$, each relation yields the minimum value of N allowing instantaneous positive tension in the corresponding cable as a function of v. These relations are represented for various instants of time in Fig. 1.4 for the trajectory corresponding to the first column of Table 1.1.

In the figure, each shaded region comprises the points (v, N) that yield instantaneous positive tension in both cables at the considered instant of time.

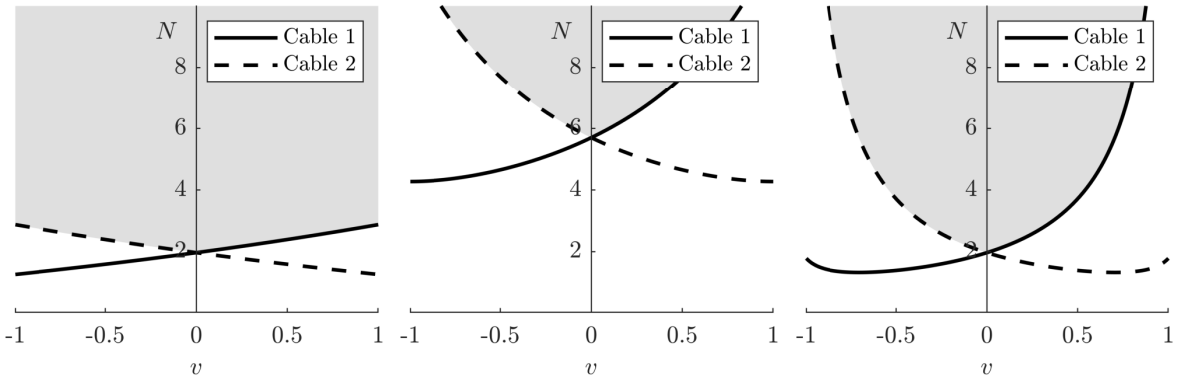

(a) $\tau = 0.25$. (b) $\tau = 0.5$. (c) $\tau = 0.75$.

Figure 1.4 – Minimum value of N as a function of v allowing instantaneous positive tension in each cable at various instants of time for the trajectory corresponding to the first column of Table 1.1.

In order for a given cable k to be under tension at *all* points of the proposed trajectory, its minimum feasible value of N must be large enough such that positive tension is maintained at the *most constraining instant* of the motion. Therefore, the minimum feasible value of N for cable k corresponds, for a given inclination v, to the maximum value of the corresponding eq. (1.44) over the considered time interval, $N_k(v) = \max_{\tau\in[0,1]} N_k(v,\tau)$. Likewise, the minimum feasible value of N of the whole trajectory is given by the largest among the minimum feasible values of N_k of each cable, which can be written as:

$$N(v) = \max\left(\max_{\tau\in[0,1]} N_1(v,\tau), \max_{\tau\in[0,1]} N_2(v,\tau)\right). \tag{1.48}$$

The above expression is the conceptual formulation of the feasible region's lower boundary equation in the $vN-$plane. For any given inclination of the motion v, this expression yields the minimum feasible value of N of the trajectory, which by virtue of eq. (1.40) leads to the minimum feasible number of oscillations n that ensures positive cable tensions at all points of the motion.

Minimum-Time Trajectory

The minimum-time trajectory for a given amplitude function corresponds to the minimum value of eq. (1.48) over v and is of substantial interest. In this regard, one should remark that, referring to eq. (1.37), both eqs. (1.44) satisfy the relation

$$N_1(v) = N_2(-v), \tag{1.49}$$

which indicates that they are symmetric one to the other with respect to the axis $v = 0$. Hence for $v = 0$, both cables have the same minimum feasible number of oscillations. Referring to

eq. (1.37), this is due to the lower pseudotension envelopes, eqs. (1.39), that are equal for the horizontal trajectory, namely:

$$\widehat{\kappa}_{eh,k} = 1 - |w_k|\sqrt{C^2 + S^2}, \qquad k = 1, 2, \tag{1.50}$$

with

$$C = \frac{c(\tau)}{4\pi^2 n^2 - A''(1)}, \tag{1.51}$$

$$S = \frac{4\pi n s(\tau)}{4\pi^2 n^2 - A''(1)}. \tag{1.52}$$

Hence the lower envelopes of both normalized pseudotensions have the same value for $v = 0$, which means that this inclination equally distributes among both cables the load required for reaching the final point. Conversely, an inclination $v \neq 0$ yields a cable supporting more load at the expense of the other (see factor $(w_k + v)$ in eqs. (1.33) and (1.34)), which results in a larger minimum feasible number of oscillations to account for the cable whose lower pseudotension envelope is the lowest. Hence, for the planar mechanism, the horizontal trajectory is the unequivocal optimal inclination leading to the overall minimum feasible value of N. Accordingly, substituting $v = 0$ into eq. (1.48) yields

$$N(0) = \max_{\tau\in[0,1]} \left(\frac{2w_{max}^2 s(\tau)^2 + A''(1) + w_{max}\sqrt{4w_{max}^2 s(\tau)^4 + 4A''(1)s(\tau)^2 + c(\tau)^2}}{4\pi^2} \right), \tag{1.53}$$

with

$$w_{max} = \max(|w_1|, |w_2|) = |\widehat{y}_1|. \tag{1.54}$$

For large values of w_{max}, the minimum feasible number of oscillations n obtained from the combination of eqs. (1.53) and (1.40) can be efficiently approximated by the expression

$$n(0) = \left(\frac{w_{max}}{\pi} \right) \max_{\tau\in[0,1]} s(\tau), \tag{1.55}$$

which constitutes a linear equation in w_{max} whose slope depends on the amplitude function being used.

In a nutshell, the minimum feasible value of N of the trajectory defined by eqs. (1.20) and (1.21) is given for a prescribed inclination $|v| < 1$ by eq. (1.48). This trajectory is the fastest for $v = 0$, for which the latter equation reduces to eq. (1.53). Once the desired value of N is computed, its square root is extracted and the resulting value is ceiled to the nearest integer to produce the minimum feasible number of oscillations, n.

1.4.5 Reverse Dynamic to Static Transition Trajectory

After a static to dynamic transition trajectory or a point-to-point trajectory segment, the end-effector is in a dynamic state and must be brought back to rest in the static workspace

through a dynamic to static transition motion. This motion has an initial nonzero acceleration that must correspond to the final acceleration of the preceding trajectory segment in order to avoid undesirable discontinuous cable forces. If eq. (1.17) is imposed on this initial kinematic state and on the final state of rest, the reverse trajectory of that proposed in Section 1.4.3 can be used, namely

$$x_b(t) = s_{x_b}(t/T) \rightarrow \ s_{x_b}(\tau) = s_x(1-\tau) \tag{1.56}$$

$$y_b(t) = s_{y_b}(t/T) \rightarrow \ s_{y_b}(\tau) = s_y(1-\tau), \tag{1.57}$$

where $s_x(\tau)$ and $s_y(\tau)$ are given by eq. (1.20) and (1.21), respectively. For the rectilinear motion defined above, the continuity of the acceleration is fully accounted for provided that the trajectory is aligned with the initial acceleration vector, in which case x_0 is given by, using to simplify,

$$x_0 = \frac{g}{g - \ddot{x}_1} x_1, \tag{1.58}$$

where eq. (1.17) was used for simplification, and where $\ddot{x}_1$ is the initial vertical acceleration, obtained from the previous trajectory segment. Hence x_0 is no longer arbitrary in a dynamic to static transition trajectory and must satisfy eq. (1.19). In such a case, the minimum feasible number of oscillations can be obtained through eq. (1.48). However, should the initial kinematic state be such that constraint (1.19) fails to be met, the state of rest cannot be reached through the proposed trajectory formulation. In this instance, other methods must be employed.

1.5 Spatial Mechanism

1.5.1 Mechanism Modelling

A spatial three-degree-of-freedom (3-dof) cable-suspended mechanism is represented schematically in Fig. 1.5. The mechanism consists of three actuated spools mounted on a fixed structure which are used to control the extension of three cables. The cables are attached to a common end-effector which is considered as a point-mass. By controlling the extension of the cables, the position of the point-mass in a three-dimensional space can be controlled. The mechanism includes three actuators and three degrees of freedom and is therefore fully actuated. However, and as is the case with the planar mechanism, constraints must be imposed on the Cartesian trajectory prescribed at the end-effector in order to ensure that a given trajectory is feasible, i.e., that it does not require compression forces in the cables.

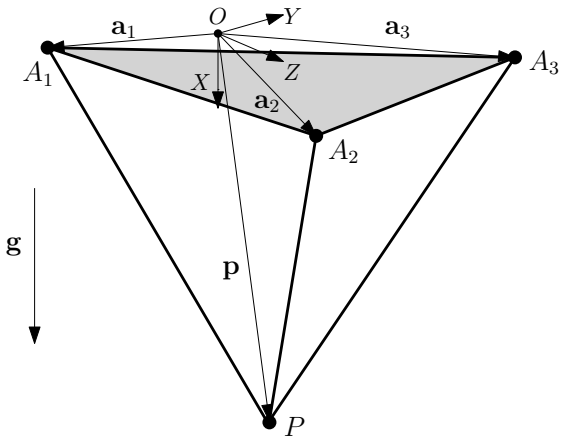

Figure 1.5 – Spatial three-dof cable-suspended mechanism.

Referring to the three-dof cable-suspended mechanism of Fig. 1.5, a fixed reference frame is first defined on the base of the mechanism. The X axis of the fixed reference frame is pointing downwards, i.e., in the direction of gravity. The points corresponding to the cable outputs of the spools are assumed to be fixed — in practice an eyelet or a pulley can be used — and are noted A_k, with $k = 1, 2, 3$. The vector connecting the origin of the fixed reference frame to point A_k is noted $\mathbf{a}_k$ and the position of the end-effector of mass m with respect to the origin of the fixed reference frame is noted $\mathbf{p} = [x, y, z]^T$.

The cable lengths, which are used as joint coordinates, are respectively noted $\rho_k,\ k = 1, 2, 3$. The inverse kinematic model can therefore be simply written as

$$\rho_k = \sqrt{(\mathbf{a}_k - \mathbf{p})^T(\mathbf{a}_k - \mathbf{p})}, \quad k = 1, 2, 3. \tag{1.59}$$

Similarly to the planar mechanism, the dynamic model of the spatial mechanism is obtained by considering the force balance on the point-mass end-effector, which can be written in matrix form as

$$\mathbf{M}\boldsymbol{\mu} = \ddot{\mathbf{p}} - \mathbf{g}, \tag{1.60}$$

with

$$\boldsymbol{\mu} = \frac{1}{m}\begin{bmatrix} \dfrac{f_1}{\rho_1} & \dfrac{f_2}{\rho_2} & \dfrac{f_3}{\rho_3} \end{bmatrix}^T, \tag{1.61}$$

and where matrix $\mathbf{M}$ is defined as

$$\mathbf{M} = \begin{bmatrix} \boldsymbol{\rho}_1 & \boldsymbol{\rho}_2 & \boldsymbol{\rho}_3 \end{bmatrix}, \tag{1.62}$$

with vectors $\boldsymbol{\rho}_k,\ k = 1, 2, 3$, given by eq. (1.6). Solving eq. (1.60) for $\boldsymbol{\mu}$ yields

$$\boldsymbol{\mu} = \mathbf{M}^{-1}(\ddot{\mathbf{p}} - \mathbf{g}) \succeq \mathbf{0}, \tag{1.63}$$

where the inverse of matrix $\mathbf{M}$ is given by eq. (1.8) with, for the spatial mechanism,

$$\det(\mathbf{M}) = (\boldsymbol{\rho}_1 \times \boldsymbol{\rho}_2)^T \boldsymbol{\rho}_3 \tag{1.64}$$

and

$$\mathrm{Adj}(\mathbf{M}) = \begin{bmatrix} (\boldsymbol{\rho}_2 \times \boldsymbol{\rho}_3)^T \\ (\boldsymbol{\rho}_3 \times \boldsymbol{\rho}_1)^T \\ (\boldsymbol{\rho}_1 \times \boldsymbol{\rho}_2)^T \end{bmatrix}. \tag{1.65}$$

Similarly to the planar mechanism, the determinant of matrix $\mathbf{M}$ is positive as long as the end-effector remains below the plane passing through the fixed cable spools. Using this assumption to simplify the positive tension constraints (1.63) yields, upon rearranging (Gosselin, 2013)

$$\kappa_1 = [\mathbf{p} \times (\mathbf{a}_2 - \mathbf{a}_3) + (\mathbf{a}_2 \times \mathbf{a}_3)]^T (\ddot{\mathbf{p}} - \mathbf{g}) > 0 \tag{1.66}$$

$$\kappa_2 = [\mathbf{p} \times (\mathbf{a}_3 - \mathbf{a}_1) + (\mathbf{a}_3 \times \mathbf{a}_1)]^T (\ddot{\mathbf{p}} - \mathbf{g}) > 0 \tag{1.67}$$

$$\kappa_3 = [\mathbf{p} \times (\mathbf{a}_1 - \mathbf{a}_2) + (\mathbf{a}_1 \times \mathbf{a}_2)]^T (\ddot{\mathbf{p}} - \mathbf{g}) > 0. \tag{1.68}$$

The above inequalities represent the necessary and sufficient conditions to be satisfied in order to ensure that the cables are kept under tension. Despite having different units than eqs. (1.13)–(1.14), the above quantities can be considered as their spatial counterparts and are therefore referred to as pseudotensions.

1.5.2 The pendulum constraint

This section aims at deriving the equation of the median of the unbounded feasible region defined by ineqs. (1.66)-(1.68). As is the case with eq. (1.17), this relation can be thought of as the locus of ideal kinematic states and can be put to good use in dynamic trajectory planning. The desired expression can be obtained from the property pointed out in Section 1.4.2 according to which a kinematic state satisfying this property admits equal pseudotensions. Accordingly one can write

$$\kappa_1 - \kappa_3 = 0 \tag{1.69}$$

$$\kappa_2 - \kappa_1 = 0 \tag{1.70}$$

$$\kappa_3 - \kappa_2 = 0. \tag{1.71}$$

The above expressions can be expanded as

$$\kappa_1 - \kappa_3 = -3\,[(\mathbf{p} - \mathbf{c}) \times (\mathbf{c} - \mathbf{a}_2)]^T (\ddot{\mathbf{p}} - \mathbf{g}) = 0 \tag{1.72}$$

$$\kappa_2 - \kappa_1 = -3\,[(\mathbf{p} - \mathbf{c}) \times (\mathbf{c} - \mathbf{a}_3)]^T (\ddot{\mathbf{p}} - \mathbf{g}) = 0 \tag{1.73}$$

$$\kappa_3 - \kappa_2 = -3\,[(\mathbf{p} - \mathbf{c}) \times (\mathbf{c} - \mathbf{a}_1)]^T (\ddot{\mathbf{p}} - \mathbf{g}) = 0. \tag{1.74}$$

where $\mathbf{c}$ stands for the position vector of the centroid of the cable spools, namely

$$\mathbf{c} = \frac{\mathbf{a}_1 + \mathbf{a}_2 + \mathbf{a}_3}{3}. \tag{1.75}$$

Eqs (1.72)–(1.74) can be written in matrix form as

$$3\mathbf{A}^T\mathbf{h} = \mathbf{0}, \tag{1.76}$$

where matrix $\mathbf{A}$ and vector $\mathbf{h}$ are respectively defined as

$$\mathbf{A} = \begin{bmatrix} (\mathbf{c} - \mathbf{a}_1) & (\mathbf{c} - \mathbf{a}_2) & (\mathbf{c} - \mathbf{a}_3) \end{bmatrix}, \tag{1.77}$$

and

$$\mathbf{h} = (\mathbf{p} - \mathbf{c}) \times (\ddot{\mathbf{p}} - \mathbf{g}). \tag{1.78}$$

In order for eq. (1.76) to be satisfied, vector $\mathbf{h}$ must either be the zero vector or be a nonzero vector belonging to the left-nullspace of $\mathbf{A}$. The latter possibility implies that all vectors orthogonal to $\mathbf{h}$ belong to the column space of $\mathbf{A}$, because the left-nullspace and the column space of any matrix are orthogonal complements of one another. Vector $(\mathbf{p} - \mathbf{c})$ is one vector orthogonal to $\mathbf{h}$ by virtue of eq. (1.78), and it cannot belong to the column space of $\mathbf{A}$ since 1) it is assumed that the end-effector remains below the plane of the cable spools; and 2) by virtue of eq. (1.77), the column space of $\mathbf{A}$ corresponds to the plane passing by the cable spools. Therefore, vector $(\mathbf{p} - \mathbf{c})$ does not belong to the column space of $\mathbf{A}$, vector $\mathbf{h}$ does not lie in the left-nullspace of $\mathbf{A}$, and thus eq. (1.76) is only satisfied if $\mathbf{h} = \mathbf{0}$, namely

$$(\mathbf{p} - \mathbf{c}) \times (\ddot{\mathbf{p}} - \mathbf{g}) = \mathbf{0}. \tag{1.79}$$

The above expression is the equation of the median of the unbounded region defined by constraints (1.66)–(1.68). Kinematic states satisfying this relation admit pseudotensions of equal value, and are thus the least likely to fall into negative tension states if an external force disturbance were to occur. It can be shown that the pseudotension associated with eq. (1.79) is

$$\kappa = \tfrac{1}{3}(\mathbf{a}_1 \times \mathbf{a}_2 + \mathbf{a}_2 \times \mathbf{a}_3 + \mathbf{a}_3 \times \mathbf{a}_1)^T(\ddot{\mathbf{p}} - \mathbf{g}). \tag{1.80}$$

Furthermore, eq. (1.79) corresponds from a physical point of view to the dynamic model, written in Cartesian coordinates, of a spatial pendulum suspended from point $\mathbf{c}$. Consequently, a kinematic state satisfying eq. (1.79) features the same properties as those stated in Section 1.4.2, and such a relation can be used in the same manner to maximize the likelihood of obtaining feasible trajectory segments.

1.5.3 Specific Mechanism Architecture

In order to provide physical insight, a special symmetric mechanism architecture is used for the remainder of the paper. In this architecture, the three spools are located on the vertices of a horizontal equilateral triangle whose centroid is at the origin of the fixed reference frame. The geometry is therefore defined as

$$\mathbf{a}_1 = \begin{bmatrix} 0 & \dfrac{\sqrt{3}a}{2} & -\dfrac{a}{2} \end{bmatrix}^T \tag{1.81}$$

$$\mathbf{a}_2 = \begin{bmatrix} 0 & -\dfrac{\sqrt{3}a}{2} & -\dfrac{a}{2} \end{bmatrix}^T \tag{1.82}$$

$$\mathbf{a}_3 = \begin{bmatrix} 0 & 0 & a \end{bmatrix}^T \tag{1.83}$$

$$\mathbf{c} = \mathbf{0}, \tag{1.84}$$

where a corresponds to the distance from a spool measured to the centroid. Substituting the above geometric parameters into inequalities (1.66) to (1.68), the latter can be rewritten as

$$\kappa_1 = -\frac{\sqrt{3}}{2}a\Big((a+\sqrt{3}y-z)(\ddot{x}-g)+x(\ddot{z}-\sqrt{3}\ddot{y})\Big) > 0 \tag{1.85}$$

$$\kappa_2 = -\frac{\sqrt{3}}{2}a\Big((a-\sqrt{3}y-z)(\ddot{x}-g)+x(\ddot{z}+\sqrt{3}\ddot{y})\Big) > 0 \tag{1.86}$$

$$\kappa_3 = -\frac{\sqrt{3}}{2}a\Big((a+2z)(\ddot{x}-g)-2x\ddot{z}\Big) > 0, \tag{1.87}$$

while the pendulum constraint becomes in scalar form:

$$\frac{\ddot{x}-g}{x} = \frac{\ddot{y}}{y} = \frac{\ddot{z}}{z}. \tag{1.88}$$

A trajectory planning algorithm is developed in the next section for this symmetric architecture.

1.5.4 Static to Dynamic Transition Trajectory Planning

Similarly to a planar transition trajectory segment, a spatial static to dynamic transition trajectory segment connects an initial point at rest in the static workspace of the mechanism to a target point in the dynamic workspace. Let $\mathbf{p}_0 = \begin{bmatrix} x_0 & y_0 & z_0 \end{bmatrix}^T$ be the coordinates of the initial (static) kinematic state, and let $\mathbf{p}_1 = \begin{bmatrix} x_1 & y_1 & z_1 \end{bmatrix}^T$ be the position vector of the final kinematic state, to be reached with a zero instantaneous velocity. Using eq. (1.88) on the initial point to maximize the likelihood of obtaining a feasible trajectory yields $y_0 = z_0 = 0$, while x_0 remains undetermined. Like the planar trajectory, the proposed motion connecting point $\mathbf{p}_0$ to point $\mathbf{p}_1$ consists of progressively increasing oscillations centred at the initial point, and therefore it can be devised as eqs. (1.20)–(1.21) along with

$$z(t) = s_z(t/T) \rightarrow \; s_z(\tau) = z_1 A(\tau)\cos(2\pi n\tau), \tag{1.89}$$

where the variables that are involved in the latter expression are defined in Section 1.4.3. Similarly to the planar motion, the opposite point of the final point along the rectilinear trajectory, point $\mathbf{p}_{-1}$, must remain below the spools, and hence constraint (1.19) equally applies. In addition to eqs. (1.24)–(1.25), the spatial trajectory must satisfy boundary conditions representing the initial state of rest and the final dynamic state in the Z–direction that can be written as

$$z(0) = \dot{z}(0) = \ddot{z}(0) = 0, \qquad z(T) = z_1, \quad \dot{z}(T) = 0. \tag{1.90}$$

Furthermore, eq. (1.88) is applied on the final kinematic state instead of eq. (1.17) to maximize the likelihood of obtaining a feasible subsequent trajectory segment, yielding

$$\frac{\ddot{x}(T)-g}{x(T)} = \frac{\ddot{y}(T)}{y(T)} = \frac{\ddot{z}(T)}{z(T)}. \tag{1.91}$$

Eqs. (1.90)–(1.91) represent additional constraints that the spatial trajectory must satisfy with respect to the planar trajectory. However, since the boundary conditions on the amplitude function derived for the planar mechanism, eqs. (1.27)–(1.28), correctly yield eq. (1.90), and since the expression for the duration of the trajectory obtained from the planar pendulum constraint, eq. (1.29), also satisfies the spatial pendulum constraint, eq. (1.91), the additional constraints (1.90)–(1.91) result in no supplementary condition imposed on the trajectory parameters.

1.5.5 Positive Tension Constraints

The positive tension constraints for the spatial mechanism can be obtained by first substituting the parametric trajectory and its time derivatives into the pseudotensions, eqs. (1.85)–(1.87). The duration of the trajectory T is thereafter eliminated from the resulting expressions by virtue of eq. (1.29). Then, using the substitutions

$$\widehat{\kappa}_k = \frac{\kappa_k}{\frac{\sqrt{3}}{2} g a^2}, \qquad v = \frac{x_1 - x_0}{x_0}, \qquad \widehat{y}_1 = \frac{y_1}{a}, \qquad \widehat{z}_1 = \frac{z_1}{a}, \tag{1.92}$$

the (normalized) pseudotensions can be written as eq. (1.32), $k = 1, 2, 3$, where C_k, S_k, $c(\tau)$, and $s(\tau)$ are respectively given by eqs. (1.33)–(1.36), and with

$$w_1 = \widehat{z}_1 - \sqrt{3}\widehat{y}_1, \qquad w_2 = \widehat{z}_1 + \sqrt{3}\widehat{y}_1, \qquad w_3 = -2\widehat{z}_1. \tag{1.93}$$

The above parameters, referred to as the weighted trajectory parameters, are closely related to the architecture of the mechanism since the coefficients multiplying the final point coordinates $\widehat{y}_1$ and $\widehat{z}_1$ depend on the position of the cable spools relative to one another. Hence, if a different mechanism architecture than the one presented in Section 1.5.3 is to be used, only the expressions for the weighted trajectory parameters differ; the form of the pseudotension expressions remains identical.

Considering the identical form of the normalized pseudotensions for the planar and spatial mechanisms, eq. (1.32), the expressions for the lower envelopes of the spatial pseudotensions are also given by eqs. (1.39), this time for $k = 1, 2, 3$. Such identical equation forms mean that spatial trajectory feasibility is determined using the same geometric constraint as for planar trajectory feasibility, namely through eq. (1.43). Likewise, the minimum feasible value of N for a given inclination v for spatial trajectories is given by

$$N(v) = \max\left(\max_{\tau\in[0,1]} N_1(v,\tau), \max_{\tau\in[0,1]} N_2(v,\tau), \max_{\tau\in[0,1]} N_3(v,\tau) \right), \tag{1.94}$$

where $N_k(v,\tau),\ k = 1, 2, 3$, is given by eq. (1.44).

The horizontal trajectory

Unlike the horizontal trajectory produced by a planar mechanism, the horizontal trajectory generated by a spatial mechanism is not the unequivocal inclination allowing the final kine-

matic state to be reached the fastest. Nonetheless, the study of this special case for the specific mechanism architecture of Section 1.5.3 remains relevant since it reveals the impact that the weighted trajectory parameters have on trajectories. Similarly to the planar trajectory, the horizontal lower pseudotension envelopes for the spatial trajectory are given by eqs. (1.50), this time for $k = 1, 2, 3$. Moreover, the minimum feasible value of N for a horizontal trajectory is obtained by substituting $v = 0$ into eq. (1.94), yielding eq. (1.53) with

$$w_{max} = \max(|w_1|, |w_2|, |w_3|). \tag{1.95}$$

Unlike those of the planar mechanism, the weighted trajectory parameters of spatial mechanisms are not all of the same magnitude for a given final kinematic state. Referring to eq. (1.93), the weighted trajectory parameter with the largest magnitude—and thus the corresponding cable—can be identified from the outset. For the mechanism of Section 1.5.3, Fig. 1.6 illustrates the portions of the $\widehat{y}_1\widehat{z}_1-$plane where each cable admits the lowest pseudotension in a horizontal trajectory along with the projection of the attachment points $A_k,\ k = 1, 2, 3$. The (open) regions are bounded by dashed straight lines whose linear equations are simply obtained by solving:

$$|w_1| = |w_2|, \qquad |w_2| = |w_3|, \qquad |w_3| = |w_1|. \tag{1.96}$$

Also depicted in Fig. 1.6 in the form of a regular hexagon is the locus of final points yielding a constant w_{max}, namely

$$w_{max} = 2R, \tag{1.97}$$

where $2R$ is the diameter of the inscribed circle. Figure 1.6 also shows the coordinates and the value of the weighted trajectory parameters for two representative final points on the locus: point H_0 is at the intersection of the hexagon and a boundary line, and point H_1 is located at the intersection of the hexagon and the straight line passing through an attachment point and the centroid of all three attachment points (not illustrated).

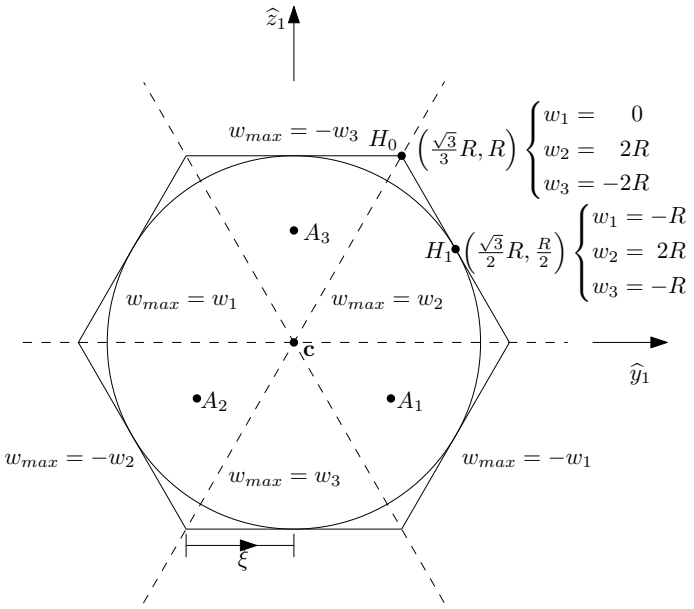

Figure 1.6 – Geometric interpretation of the weighted trajectory parameters.

As it can be observed from Fig. 1.6, the weighted trajectory parameter with the largest magnitude is the one whose corresponding attachment point is located in the region (or opposite region) of the final point. Moreover, it is negative if the final point is in the region of the k-th attachment point and positive if the final point is in the opposite region.

Referring to eq. (1.53), the minimum feasible value of N in a horizontal trajectory depends solely on the numerical value of w_{max} for a given amplitude function. Therefore, the hexagonal locus represented in Fig. 1.6 also corresponds to the set of final points that have an identical minimum feasible number of oscillations in a horizontal trajectory for a given amplitude function. As it is shown below however, this value of N leads to the minimum value for the minimum feasible number of oscillations for only some of these final points, i.e., some final points have an inclination v that allows a minimum feasible number of oscillations lower than the one required to perform a horizontal trajectory.

Referring to eq. (1.50), a horizontal trajectory aiming at a final kinematic state satisfying any of eqs. (1.96) admits two equally low pseudotension envelopes in the corresponding cables. For such a final point, the remaining cable has a zero weighted trajectory parameter that produces a constant unitary pseudotension. Specifically, the remaining pseudotension does not fluctuate throughout this rectilinear trajectory since the latter is perpendicular to the straight line passing through the centroid of the cable spools and the attachment point of the corresponding cable, i.e., $\mathbf{a}_k \times \dot{\mathbf{p}} = \mathbf{a}_k \times \ddot{\mathbf{p}} = \mathbf{0}$ (see eqs. (1.66)–(1.68)). Therefore, as it is the case with the final points of the planar trajectory formulation of Section 1.4, final points satisfying any of eqs. (1.96) generate nonzero weighted trajectory parameters of opposite signs but of identical magnitude that cause the lowest pseudotension envelope of a horizontal

trajectory to be equally shared by all possible cables. For this reason, the horizontal trajectory constitutes in both cases the optimal inclination that leads to the minimum value for the minimum feasible number of oscillations. The planar trajectory formulation of Section 1.4 can therefore be construed as a special case of spatial trajectories and is treated as such in the remainder of the paper. With regard to Fig. 1.6, point H_0 has an optimal horizontal inclination and thereby represents the farthest points from the centroid of the cable spools that can be reached through a horizontal motion for a given w_{max}.

For final points not satisfying any of eqs. (1.96), the magnitude of the weighted trajectory parameters all differ from one another and the inclination v can be set to a nonzero value to reduce the adverse effect that the weighted trajectory parameter with the largest magnitude has on its pseudotension envelope. Actually, as parameters $w_k,\ k = 1, 2, 3$, appear in the form of $|w_k+v|$ in eqs. (1.39) and on the numerator of eqs. (1.44), the sign of the optimal inclination v depends on the sign of the weighted trajectory parameter with the largest magnitude as given by eq. (1.112). Consequently, the horizontal trajectory cannot be the inclination that allows the final kinematic state to be reached the fastest for final points not satisfying any of eqs. (1.96). However, an increasing magnitude of v has a compounding adverse effect on the number of oscillations by virtue of the amplitude function. This impact can be seen in factor $-vA(\tau)$ that appears in eqs. (1.33) and most significantly on the denominator of eqs. (1.44). The optimal inclination v is therefore a tradeoff between these two absolutes. It depends on the final point and on the choice of the amplitude function and can be obtained numerically from the optimization over v of eq. (1.94) temporally discretized along the trajectory. For a final point admitting weighted trajectory parameters with the most disparate magnitudes, its optimal inclination has the largest magnitude—and is the farthest from a horizontal trajectory—, and thereby point H_1 in Fig. 1.6 is the closest point from the centroid of the cable spools that can be reached through a horizontal motion for a given w_{max}.

1.5.6 Reverse Dynamic to Static Transition Trajectory

If the end-effector is stationary and meets eq. (1.88), it can be brought back to rest in the static workspace through the reverse trajectory of that proposed in Section 1.5.4, namely

$$x_b(t) = s_{x_b}(t/T) \rightarrow \ s_{x_b}(\tau) = s_x(1-\tau) \tag{1.98}$$

$$y_b(t) = s_{y_b}(t/T) \rightarrow \ s_{y_b}(\tau) = s_y(1-\tau) \tag{1.99}$$

$$z_b(t) = s_{z_b}(t/T) \rightarrow \ s_{z_b}(\tau) = s_z(1-\tau), \tag{1.100}$$

where $s_x(\tau)$, $s_y(\tau)$ and $s_z(\tau)$ are given by eqs. (1.20), (1.21) and (1.89), respectively, and where $x_b(t)$, $y_b(t)$ and $z_b(t)$ define the reverse trajectory. For the rectilinear motion defined above, the mandatory continuity of the acceleration is fully accounted for provided that the trajectory is aligned with the initial acceleration vector, in which case x_0 is no longer arbitrary but given by eq. (1.58). If this value is such that it satisfies eq. (1.42), the corresponding

minimum feasible number of oscillations is given by eqs. (1.94) and (1.40); otherwise, the state of rest cannot be reached through the trajectory defined by eqs. (1.98)–(1.100) and numerical methods must be employed.

1.6 The amplitude function

As stated in Section 1.4.3, the amplitude function can be any smooth function on the interval $\tau \in [0, 1]$ that satisfies the conditions given in eqs. (1.27) and (1.28), for instance:

$$A_1(\tau) = -3\tau^4 + 4\tau^3, \quad A_2(\tau) = 6\tau^5 - 15\tau^4 + 10\tau^3, \quad A_3(\tau) = 2\tau^5 - 7\tau^4 + 6\tau^3. \tag{1.101}$$

Although the expression that can be used as an amplitude function is not unique, all valid functions do not produce the same results, i.e., some are better suited than others to perform a given trajectory. Specifically, the role of the amplitude function is to shape the distribution throughout time of the load required for reaching the final point. As a result, the more evenly a given amplitude function distributes this load along a given trajectory, the more efficient it is in performing such trajectory and the lower the minimum feasible number of oscillations will be. In this section, the decoupling of the amplitude function from the weighted trajectory parameters in the horizontal pseudotension envelopes (eqs. (1.50)) is exploited to derive a zero-tension amplitude function for horizontal trajectories.

1.6.1 Zero-Tension Amplitude Function for the Horizontal Trajectory

The horizontal pseudotension envelopes can be used to derive a zero-tension amplitude function for horizontal trajectories, i.e., one for which the lower envelope of the lowest pseudotension is held at a constant zero value at all instants of a trajectory passing by the initial and final points. Considering the form of eqs. (1.50), such an amplitude function is a solution of the equation

$$1 - w_{max}\sqrt{C^2 + S^2} = 0, \quad \forall\, \tau \in [0, 1], \qquad \text{with} \qquad A(0) = 0, \quad A(1) = 1. \tag{1.102}$$

The above problem consists of a second order nonlinear ordinary differential equation with Dirichlet boundary conditions and unknown parameter n. Its particular solution is given by:

$$A_{idl}(\tau) = \tau, \tag{1.103}$$

and

$$n_{idl} = \frac{w_{max}}{\pi}, \tag{1.104}$$

where A_{idl} and n_{idl} respectively stand for the zero-tension amplitude function and its corresponding value of n. As it can be seen, eq. (1.103) does not satisfy the first and second order boundary conditions of eqs. (1.27) and (1.28), and thereby cannot be used in practice. However, the value for parameter n obtained concurrently is of great use as it constitutes a lower

bound for the minimum feasible number of oscillations of horizontal trajectories. Indeed, the value of n given by eq. (1.104) is obtained from an amplitude function that distributes to perfection the load required for reaching the final point at each instant of the motion, and therefore *no other amplitude function can yield a smaller minimum feasible number of oscillations for a given final point to be reached by a horizontal motion.* As a result, the effectiveness of practical amplitude functions in performing horizontal trajectories can be assessed by comparing the value of n obtained from eqs. (1.53) and (1.40) to the one obtained from eq. (1.104) for a given final point. Appendix A (Section 1.9) provides a piecewise-defined amplitude function that exploits the benefits of the zero-tension amplitude function while satisfying the first and second order boundary conditions of eqs. (1.27) and (1.28) so that it can be used in practice.

1.6.2 Zero-Tension Amplitude Function for Nonhorizontal Trajectories

Defined analogously as that for horizontal trajectories, the zero-tension amplitude function for nonhorizontal trajectories allows, with the appropriate value for parameter n, the lower envelope of the lowest pseudotension to admit a (constant) zero value at all instants of a nonhorizontal trajectory. The expression that solves the corresponding nonlinear second order ordinary differential equation was not found but if it exists, it invariably depends on the weighted trajectory parameters w_k and the inclination v of the trajectory since both are coupled to the amplitude function derivatives in eq. (1.39).

In the absence of such a solution, the zero-tension amplitude function for horizontal trajectories, eq. (1.103), can nevertheless be used to study nonhorizontal trajectories. Indeed, its simple mathematical form leads to analytic formulas for the optimal inclination and its corresponding value of n whose behaviours are assumed to be similar to those produced by similar practical amplitude functions, such as those given in eq. (1.101). This study, which is presented in Appendix B (Section 1.10), notably concludes that, for a nonhorizontal motion, choosing the minimum value for the minimum feasible number of oscillations over the one obtained from a horizontal motion yields a negligible gain. This result is important since it allows in practice to use the simpler horizontal trajectory and have the effectiveness of the optimal inclined trajectory.

1.7 Examples

Example simulations for three types of trajectories are conducted, each one being designed to highlight the impact of the variation of one parameter on the minimum feasible number of oscillations, namely the magnitude of the largest weighted trajectory parameter for the planar and spatial mechanisms, the inclination v, and the amplitude function being used.

1.7.1 Comparison of the Planar and Spatial Mechanisms

For a given amplitude function, the minimum feasible number of oscillations in a horizontal trajectory is solely determined by the magnitude of the largest weighted trajectory parameter. The expression for this parameter varies depending on the type of mechanism being used, planar or spatial, and, for the latter mechanism, on the direction in the horizontal plane in which the trajectory occurs. The first simulation illustrates this dependency for a final point located at a given distance $\widehat{d} = 4$ from the vertical axis passing through the centroid of the cable spools. Table 1.1 presents the expression for the largest weighted trajectory parameter as a function of $\widehat{d}$ along with the corresponding nonceiled minimum feasible number of oscillations for the planar mechanism and for final points corresponding to points H_0 and H_1 in Fig. 1.6. This simulation was conducted for a horizontal trajectory performed with the amplitude function $A_1(\tau)$ given in eq. (1.101). The nonceiled minimum feasible numbers of oscillations are thus obtained from eqs. (1.53) and (1.40). The amplitude function $A_1(\tau)$ is the polynomial function of minimal degree that satisfies all the boundary constraints (1.27) and (1.28).

	Planar	Spatial Mechanism	
	Mechanism	H_0	H_1
w_{max}	$\widehat{d}$	$\sqrt{3}\widehat{d}$	$2\widehat{d}$
n	2.15	3.86	4.47

Table 1.1 – Nonceiled minimum feasible number of oscillations obtained for reaching—with a horizontal trajectory—a final point located at a distance $\widehat{d} = 4$ from the vertical axis passing through the centroid of the cable spools with the amplitude function $A_1(\tau)$ for the planar mechanism and for final points corresponding to points H_0 and H_1 of the spatial mechanism.

Hence for a final point located at a distance $\widehat{d} = 4$ from the central vertical axis of the mechanism, the (nonceiled) minimum feasible number of oscillations is reduced by 14% if the trajectory is performed in the direction of point H_0 instead of in the direction of point H_1, and by 44.31% over this improved result if the trajectory is instead performed with the planar mechanism. For target points all located in a single plane, it is therefore advantageous to use a planar mechanism.

1.7.2 Experimental Validation

In order to validate the proposed trajectory formulation, the trajectory corresponding to the middle column of Table 1.1 is performed experimentally using the three-dof spatial cable-suspended mechanism shown in Fig. 1.7. The distance between the centroid of the cable spools and one attachment point is $a = 0.693$ m, and thereby the final point of the performed trajectory has the Cartesian coordinates $(0, 2.77, 0)$ m. Three servo-controlled winches are

used to control the length of the cables. The motion performed by the end-effector of mass $m = 0.129$ kg consists of the transition trajectory given by eqs. (1.20), (1.21) and (1.89), then continues with three oscillations of constant amplitude obtained by setting $A(\tau) = 1$ in the aforementioned equations, and concludes by the reverse transition trajectory described in Section 1.5.6. The parametric trajectory is shown in Fig. 1.8a, while Fig. 1.8b provides the cable tensions per unit mass throughout the trajectory. As expected, the first figure shows that the end-effector oscillates horizontally with increasingly large amplitudes until it reaches its target point. Figure 1.8b shows that the tensions in the cables are positive at all instants of the trajectory, which confirms that the value of n obtained from eq. (1.53) is sufficiently large. Moreover, the lowest tension is positive—rather than zero—because the value of n used is ceiled to the nearest integer in performing the trajectory and because, as it can be recalled, such a value of n ensures nonnegativity in the tension envelopes, which is a sufficient but not necessary condition for positive cable tensions. A video showing this experimentation (*Chap1_3dofTransitionTrajectory.mp4*) is available under [46] Pascal Dion-Gauvin at:

https://robot.gmc.ulaval.ca/publications/these-de-doctorat.

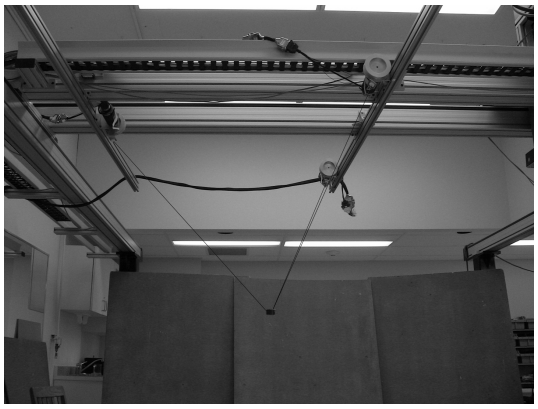

Figure 1.7 – Spatial mechanism used to perform the experimental validation.

1.7.3 Comparison of Trajectories Performed with various Inclinations

As demonstrated in Appendix B (Section 1.10), the gain in number of oscillations obtained by choosing the optimal inclination over the horizontal motion for a trajectory performed with an amplitude function similar to eq. (1.103) is negligible for all final points. Simulation results are now presented that aim to validate this statement for practical amplitude functions. To this end, a final point for which this gain is believed to be the most significant is desired. In this regard, Fig. 1.11b shows that such a final point has the coordinates $(\sigma R = 1, \xi = 1)$ for the amplitude function given by eq. (1.103), and thereby this point is heuristically selected for the amplitude functions $A_1(\tau)$, $A_2(\tau)$, and $A_3(\tau)$. The amplitude function $A_2(\tau)$ is the polynomial function of minimal degree that satisfies all the boundary constraints and that ensures $A''(1) = 0$, while the amplitude function $A_3(\tau)$ is the polynomial function of degree 5 that generally yields the lowest minimum feasible number of oscillations in horizontal trajectories, i.e., the

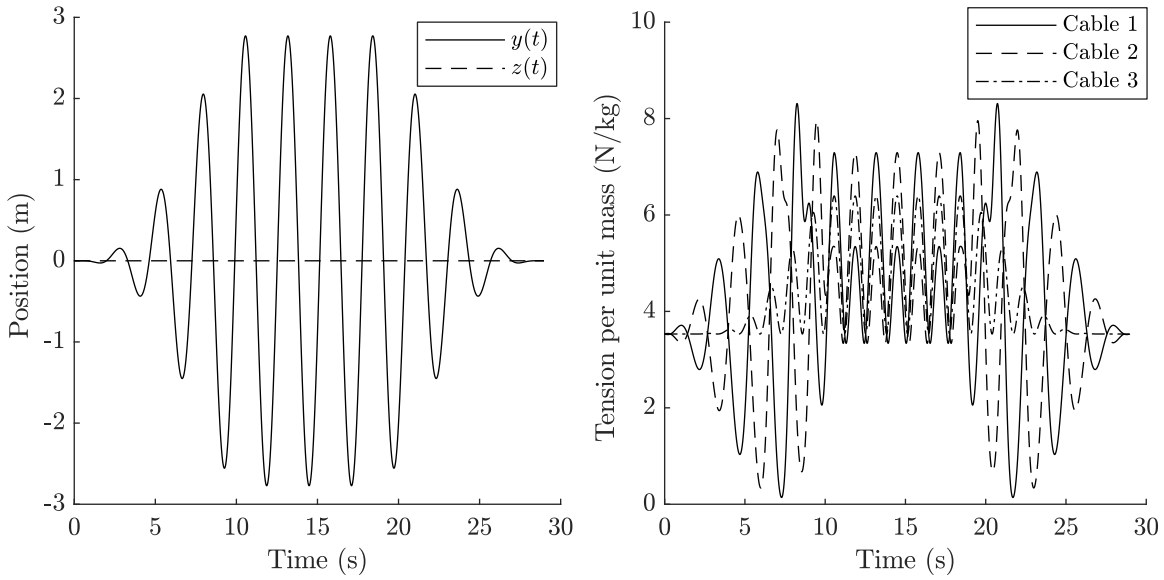

(a) Parametric trajectory.

(b) Tensions in the cables.

Figure 1.8 – Simulation results of the experimental validation.

one with the lowest maximum slope $s(\tau)$ on the interval $\tau \in [0,1]$ (see eq. (1.55)). The optimal inclination for reaching this final point is obtained by the numerical optimization over v of eq. (1.94) temporally discretized along the trajectory. Table 1.2 presents the nonceiled minimum feasible number of oscillations for this inclination and for various others. Values of n for nonhorizontal trajectories are computed numerically using eq. (1.94), while that for the horizontal trajectory is calculated with eq. (1.53).

Inclination v	$-v_{opt}$	0	v_{opt}	0.8	0.999
Min. feas. value of n for $A_1(\tau)$ $(v_{opt} = 0.5681)$	1.21	0.85	0.69	0.76	2.82
Min. feas. value of n for $A_2(\tau)$ $(v_{opt} = 0.48798)$	1.54	1.1	0.93	1.29	8.25
Min. feas. value of n for $A_3(\tau)$ $(v_{opt} = 0.71002)$	1.41	0.90	0.61	0.73	1.62

Table 1.2 – Nonceiled minimum feasible number of oscillations obtained for reaching the final point $(\sigma R = 1, \xi = 1)$ with various amplitude functions and inclinations.

Hence the final point for which it is the most advantageous to use the optimal inclination over the horizontal inclination is $(\sigma R = 1, \xi = 1)$, and for this final point the values of n corresponding to the optimal inclination are only slightly lower than the one required for a horizontal trajectory. Considering that the values of n must be ceiled to the nearest integer in order for the final kinematic state to be reached with a zero velocity, it must be concluded that choosing the optimal inclination over the horizontal inclination leads to an actual gain in the number of oscillations for only an insignificant number of final points. This result allows in practice to use the simpler horizontal trajectory and have the effectiveness of the optimal inclined trajectory.

1.7.4 Comparison of Trajectories Performed by various Amplitude Functions

Simulation results are now presented to investigate the effectiveness of various amplitude functions in performing a horizontal trajectory aiming at the final point ($\sigma R = 5, \xi = 0$). The amplitude functions considered in this simulation consist of those given in eq. (1.101) along with the piecewise-defined function defined in Appendix A (Section 1.9). The piecewise-defined amplitude function is used with its optimal value for parameter ε, and from the numerical optimization of eq. (1.53) temporally discretized along the trajectory, $\varepsilon = 0.0399$ is obtained for the considered final point. Table 1.3 presents the nonceiled minimum feasible number of oscillations obtained for reaching the final point with each of the aforementioned amplitude functions along with the lower bound of n as obtained from eq. (1.104).

Amplitude function	A_{idl}	$A_1(\tau)$	$A_2(\tau)$	$A_3(\tau)$	$A_{eff}(\tau)$
Min. feas. value of n	2.76	4.85	5.17	4.72	2.94

Table 1.3 – Nonceiled minimum feasible number of oscillations obtained for reaching the final point ($\sigma R = 5, \xi = 0$) horizontally with various amplitude functions.

Hence for the trajectory performed in this simulation, the amplitude functions given in eq. (1.101) all lead to similar minimum feasible numbers of oscillations, whereas the piecewise-defined function of eq. (1.110) yields a significantly lower value, near the lower bound predicted by eq. (1.104). These results are evidenced by Fig. 1.9, where the lower envelope of the lowest pseudotension obtained for each amplitude function is plotted using its nonceiled value for n. As expected, it can be observed that the average value of the lowest of eqs. (1.50) for the piecewise-defined amplitude function is significantly lower than the one produced by the other amplitude functions, thereby confirming that the load required for reaching the final point is distributed more evenly with eq. (1.110) than it is with any of the functions defined in eq. (1.101). Referring to eq. (1.55), values of n obtained from these amplitude functions for other final points admit relative differences among them that are similar to those found in Table 1.3, and therefore the effectiveness of the amplitude functions determined in this simulation extend to all horizontal trajectories. As a result, considering that the ceiling of the minimum feasible number of oscillations mitigates the gain resulting from using a horizontally-effective amplitude function, it must be concluded that using the piecewise-defined amplitude function is particularly worthwhile for high values of n, i.e., for reaching final points that are located far from the centroid of the cable spools.

1.8 Conclusion

This paper proposes a transition trajectory formulation for planar two-dof and spatial three-dof cable-suspended mechanisms with point-mass end-effectors. This transition trajectory

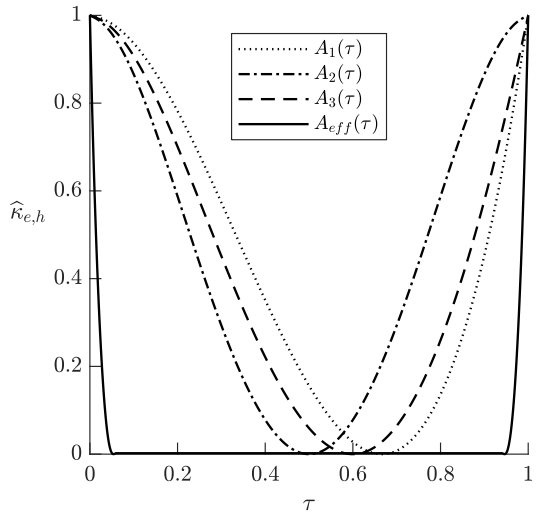

Figure 1.9 – Lower envelope of the lowest pseudotension for various amplitude functions performing the same horizontal trajectory.

connects an initial point at rest in the static workspace of the mechanisms to a final point to be reached with a zero velocity and nonzero acceleration. First, the tension equations of each mechanism are used to obtain the locus of ideal kinematic states, which corresponds to that of a simple pendulum suspended from the centroid of the cable spools. In a context of point-to-point trajectory planning constructed as a sequence of trajectory segments, prescribing these kinematic states at the endpoints of a point-to-point trajectory increases the likelihood of obtaining feasible subsequent trajectory segments, and therefore such relation constitutes in itself an important result of the paper. Using the latter constraint, the proposed motion is then defined. It consists of oscillations of progressively increasing amplitude centred at the initial point, whereby a minimum feasible number of oscillations is determined by ensuring positive tensions in all cables throughout the trajectory. It is found that the horizontal trajectory is the unequivocal minimum-time inclination for the planar mechanism, while it is the optimal inclination for the spatial mechanism in only certain orientations. Additionally, an amplitude function that allows the lowest tension envelope to be zero at all instants of the motion is analytically derived for horizontal trajectories. Although such an amplitude function cannot be used in practice, it leads to a lower bound for the minimum feasible number of oscillations that can be used to assess the efficiency of various amplitude functions in reaching a given final point. Finally, simulation examples are given. One of the simulations conducted was also successfully performed experimentally, which validates the proposed approach. This study opens the avenue for using cable-suspended mechanisms beyond their static workspace. Current work includes the dynamic point-to-point trajectory planning of a point-mass end-effector in three dimensional space.

1.9 Appendix A: Derivation of an effective amplitude function

The zero-tension amplitude function for horizontal trajectories, eq. (1.103), can inspire the design of a highly effective amplitude function that can be used in practice. As represented in Fig. 1.10, the proposed solution consists of a piecewise-defined function with three segments, the second of which is linear. It is akin to the third order polynomial s-curve (Nguyen et al., 2008), since both have similar velocity profiles and ensure continuity up to the acceleration level at the connections of the segments. On the interval $\tau \in [0, \varepsilon]$, the amplitude function satisfies the boundary conditions (1.27) along with having a zero curvature at $\tau = \varepsilon$ to ensure the continuity of the acceleration with the linear segment. Additionally, to make the proposed amplitude function effective, a strictly increasing slope from a zero value at $\tau = 0$ to a maximum value in $\tau = \varepsilon$ is desired. The linear function defined on the second interval $\tau \in [\varepsilon, 1-\varepsilon]$ ensures continuity and smoothness with the preceding segment, and its slope is thereby given by the final slope of the previous interval. The function defined over the last interval matches at $\tau = 1-\varepsilon$ the final conditions of the linear segment to ensure continuity up to the acceleration level and satisfies at $\tau = 1$ the boundary conditions (1.28). Additionally, a zero acceleration is prescribed at the end of the considered time interval ($A''(1) = 0$) in order to make the piecewise-defined amplitude function symmetric. Finally, a strictly decreasing slope throughout the last interval is desired to make the proposed amplitude function effective.

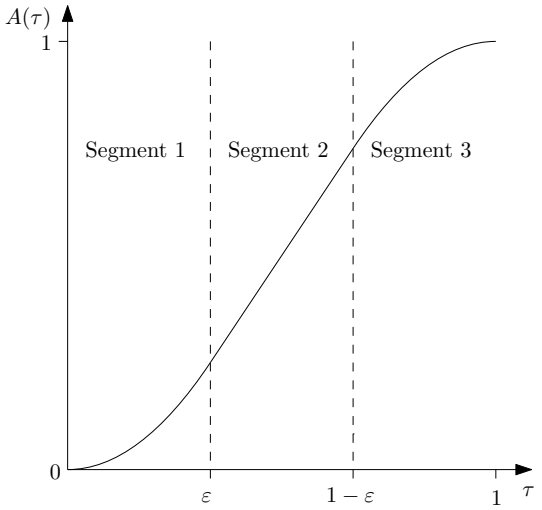

Figure 1.10 – Piecewise-defined amplitude function.

Rewriting the acceleration constraints effective on the first segment yields zero curvature at the endpoints of the interval and strictly positive curvature in between. Defining $f_1(\tau)$ as the amplitude function on the interval $\tau \in [0, \varepsilon]$, one can set

$$f_1''(\tau) = \frac{-6m}{\varepsilon^3}\tau(\tau - \varepsilon), \tag{1.105}$$

where it can be readily shown that m is the slope of the linear segment of the amplitude function. Integrating twice the above expression while satisfying the boundary conditions (1.27) yields

$$f_1(\tau) = -\frac{m\tau^3(\tau - 2\varepsilon)}{2\varepsilon^3}. \tag{1.106}$$

On the second interval, the amplitude function can be defined as

$$f_2(\tau) = m(\tau - \varepsilon) + \frac{m\varepsilon}{2}, \tag{1.107}$$

where $\frac{1}{2}m\varepsilon$ is the value of the amplitude function at the beginning of the second interval as obtained from the previous segment. On the third interval, the constraints—in particular, zero curvature at the endpoints of the interval and strictly negative curvature in between—are analogous to those of the first interval, and thereby the function that applies on the third interval $f_3(\tau)$ can be defined as the reverse of that of the first interval. This leads to

$$f_3(\tau) = 1 - f_1(1 - \tau). \tag{1.108}$$

Ensuring that the above expression is continuous and smooth with the linear segment yields:

$$m = \frac{1}{1 - \varepsilon}. \tag{1.109}$$

Collecting eqs. (1.106)–(1.109), the proposed amplitude function can be written as

$$A_{eff}(\tau) = \begin{cases} \dfrac{\tau^3(2\varepsilon - \tau)}{2\varepsilon^3(1 - \varepsilon)} & \text{for } \tau \in [0, \varepsilon] \\ \dfrac{2\tau - \varepsilon}{2(1 - \varepsilon)} & \text{for } \tau \in [\varepsilon, 1 - \varepsilon] \\ 1 - \dfrac{(1 - \tau)^3(2\varepsilon - (1 - \tau))}{2\varepsilon^3(1 - \varepsilon)} & \text{for } \tau \in [1 - \varepsilon, 1], \end{cases} \tag{1.110}$$

where $\varepsilon \in]0, 0.5]$ is a free parameter.

Althought the amplitude function defined above is based on the properties of the horizontal pseudotension expressions, it can obviously be employed to perform nonhorizontal trajectories. Moreover, the choice of ε as a free parameter is a convenient one. Indeed, referring to eq. (1.110), a small value of ε leads to a small slope in the second interval at the expense of large curvatures in the first and third intervals, and vice-versa. Yet since w_{max} is only multiplied by $s(\tau)$ in the numerator of eq. (1.53), the slope has a greater incidence on the number of oscillations for final points admitting large values of w_{max}, whereas the curvature-related $c(\tau)$ has a greater incidence on the number of oscillations for final points admitting small values of w_{max}. Hence the relation between the optimal ε and the distance from the centroid of the cable spools to final point is unequivocal: the optimal ε decreases as w_{max} increases. In practice, the numerical value of the optimal ε for a given position of the final kinematic state and its corresponding minimum feasible number of oscillations can be obtained numerically from the optimization of eq. (1.53) temporally discretized along the trajectory.

1.10 Appendix B: Study of nonhorizontal trajectories with the zero-tension amplitude function for horizontal trajectories

Symmetric Representation

A convenient way to represent the position of final points considering the symmetry of the mechanism presented in Section 1.5.3 is to express them in a $(\sigma R, \xi)$ coordinate system. In doing so, two symmetric final points having different $(\widehat{y}_1, \widehat{z}_1)$ coordinates but identical characteristics will admit a unique $(\sigma R, \xi)$ representation. This coordinate system thus facilitates the synthesis and is used for this purpose in this section.

Referring to Fig. 1.6, a normalized coordinate $\xi \in [0, 1]$ can be defined to denote the position of the points H_ξ measured linearly from a sector boundary ($\xi = 0$) up to its bisector ($\xi = 1$). Because of the symmetry of the locus, twelve final points have an identical set of numerical values of parameters $|w_k|,\ k = 1, 2, 3$, for a given R and thus admit a common ξ coordinate, which can be found by the relation

$$\xi = \frac{\min(|w_1|, |w_2|, |w_3|)}{R}, \tag{1.111}$$

with R given by eq. (1.97). Hence final points that have a horizontal optimal inclination admit $\xi = 0$, while final points that have a nonhorizontal optimal inclination have $\xi \neq 0$. At this point it remains to discriminate the final points whose weighted trajectory parameter with the largest magnitude is positive from those whose weighted trajectory parameter with the largest magnitude is negative. Since the weighted trajectory parameters all add up to 0 by definition, the sign σ of the weighted trajectory parameter with the largest magnitude can be obtained by:

$$\sigma = \text{altsgn}(w_1 w_2 w_3), \tag{1.112}$$

where the alternate signum function $\text{altsgn}(x)$ is defined as

$$\text{altsgn}(x) = \begin{cases} \pm 1 & \text{for } x = 0 \\ \text{sgn}(x) & \text{otherwise,} \end{cases} \tag{1.113}$$

i.e., such that $\text{altsgn}^2(x) = 1$ is continuous on $\mathbb{R}$. Hence a unique $(\sigma R, \xi)$ representation encompasses all final points that have identical optimal inclination and minimum feasible number of oscillations. This representation can be used to rewrite the weighted trajectory parameters, which yields, referring to Fig. 1.6:

$$w_A = 2\sigma R - \sigma R \xi, \qquad w_B = \sigma R \xi, \qquad w_C = -2\sigma R, \tag{1.114}$$

where each of w_A, w_B, and w_C represents either w_1, w_2 or w_3, depending on the region of the $(\widehat{y}_1, \widehat{z}_1)$ plane where the final point is located.

Prescribed Final Point and Inclination

The value of parameter n for a nonhorizontal trajectory performed by the zero-tension amplitude function for horizontal trajectories is obtained by substituting eq. (1.103) into eq. (1.94). Its minimum value, occurring at $\tau = 1$, is given by:

$$n_{gdl} = \frac{\max(|w_1 + v|, |w_2 + v|, |w_3 + v|)}{\pi\sqrt{1 - v^2}}. \tag{1.115}$$

For a prescribed final point and a prescribed inclination, the above equation yields the minimum value of n for which the zero-tension amplitude function for horizontal trajectories produces nonnegative pseudotension envelopes throughout the interval $\tau \in [0, 1]$. Hence eq. (1.104) is retrieved for $v = 0$, but since the above expression originates from an amplitude function that does not produce zero tension for nonhorizontal trajectories, its numerical value can only be used as a guideline, and not as a lower bound, for minimum feasible numbers of oscillations of nonhorizontal trajectories.

As it can be observed from eq. (1.115), the index n_{gdl} is determined by the largest of the terms $|w_k + v|$ for a prescribed inclination, and therefore does not necessarily originate from the cable whose weighted trajectory parameter has the largest magnitude. More precisely, it is either determined by the weighted trajectory parameter with the largest positive value or by the one with the largest negative value (depending on the sign of v), and therefore can only come from two of the three cables for a given final point. Substituting eq. (1.114) into eq. (1.115), the latter can be rewritten as a function of the determining cable, namely

$$n_{gdl} = \begin{cases} \dfrac{|2\sigma R - \sigma R\xi + v|}{\pi\sqrt{1 - v^2}} & \text{for} \quad \dfrac{v}{\frac{1}{2}\sigma R\xi} \geq 1 \\ \dfrac{|-2\sigma R + v|}{\pi\sqrt{1 - v^2}} & \text{for} \quad \dfrac{v}{\frac{1}{2}\sigma R\xi} \leq 1. \end{cases} \tag{1.116}$$

In the above equation, a division by zero can only occur in the subdomain definition of the function when the normalized coordinate ξ is zero. In this case, the two weighted trajectory parameters have the same magnitude but bear opposite signs, and in this regard eq. (1.116) coherently predicts that the determining cable is the one whose weighted trajectory parameter has the sign of the prescribed inclination.

Optimal Inclination for a Prescribed Final Point

The optimal inclination for a given final point corresponds to the minimum point of eq. (1.116). Therefore, it is found either where its derivative with respect to v is zero or at the common boundary of the subfunctions' respective domain. A thorough analysis leads to:

$$v_{gdl,min} = \begin{cases} \sigma\dfrac{R\xi}{2} & \text{for } R^2\xi \leq 1 \\ \sigma\dfrac{1}{2R} & \text{for } R^2\xi \geq 1. \end{cases} \tag{1.117}$$

Substituting the optimal inclination into eq. (1.116) leads to the minimum value of n_{gdl} as a function of v, namely

$$n_{gdl,min} = \begin{cases} \dfrac{(4-\xi)R}{\pi\sqrt{4-R^2\xi^2}} & \text{for} R^2\xi \leq 1 \\ \dfrac{\sqrt{4R^2-1}}{\pi} & \text{for } R^2\xi \geq 1. \end{cases} \tag{1.118}$$

The above two equations are analytic formulas respectively yielding the optimal inclination and the minimum value of n_{gdl} as a function of the final point for a trajectory performed with the zero-tension amplitude function for horizontal trajectories. In particular, an optimal horizontal inclination and its corresponding value of n, eq. (1.104), is retrieved for $\xi = 0$. Since eq. (1.103) is similar to the majority of practical amplitude functions—such as those given in eq. (1.101)—, values produced by eqs. (1.117)–(1.118) are representative of those obtained in real trajectories and are thereby represented graphically in Fig. 1.11. First, the boundary delimiting the two subdomains of these equations, $R^2\xi = 1$, is depicted in Fig. 1.11a in the Cartesian $\widehat{y}_1\widehat{z}_1-$plane along with the projection of the attachment points A_k, $k = 1, 2, 3$, and the dashed straight lines of the locus of final points satisfying $\xi = 0$. Numerical simulations conducted with practical amplitude functions show that such boundaries exist for real trajectories. Figure 1.11b illustrates in the $\sigma Rv-$plane the optimal inclination as given by eq. (1.117) for three values of ξ. For $R^2\xi < 1$, the optimal inclination is found at the common linear boundary of the regions corresponding to the determining cable (see eq. (1.116)), which generates two equal pseudotension envelopes. For $R^2\xi > 1$, the minimum value of n_{gdl} is produced by a unique cable, the one with the largest weighted trajectory parameter, and thereby the optimal inclination is obtained by equating to zero the derivative of the corresponding subfunction of eq. (1.116) with respect to v. It is remarkable that the optimal inclination on this interval is not affected in any means by the coordinate ξ. Moreover, this graph illustrates that for values of R and v of the same order of magnitude, the magnitude of the optimal inclination increases when ξ increases, in accordance with what is explained in Section 1.5.5. Finally, Fig. 1.11c illustrates in the $Rn-$plane the value of $n_{gdl,min}$ given by eq. (1.118) for three values of ξ. It can be observed that the minimum value of n_{gdl} increases approximately linearly with R, which demonstrates the applicability of eq. (1.55). Moreover, even though the optimal inclination varies greatly with ξ for values of R and v of the same order of magnitude, eq. (1.118) remains only slightly affected by this coordinate. As a result, recalling that the value of $n_{gdl,min}$ for $\xi = 0$ corresponds to eq. (1.104), a lower bound for the minimum feasible number of oscillations of horizontal trajectories for *any* final point located on a hexagonal locus of apothem R, it can be concluded that the gain in number of oscillations obtained by choosing the optimal inclination over the horizontal one is minimal. Since it allows to use the simpler horizontal trajectory and have the effectiveness of the optimal inclined trajectory, this result is important and should be considered when performing real trajectories.

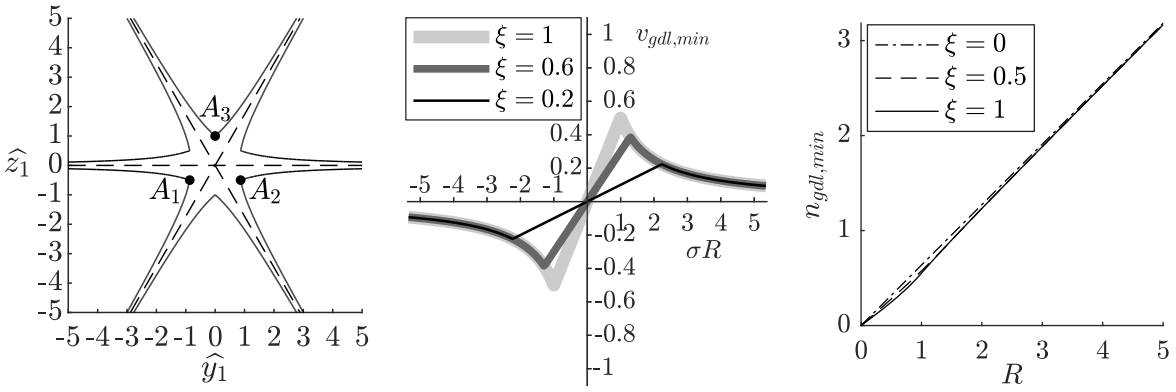

(a) Locus of the optimal inclination with the largest magnitude as a function of $\widehat{y}_1$ and $\widehat{z}_1$. The dashed straight lines correspond to the set of final points satisfying $\xi = 0$.

(b) Optimal inclination as a function of the final point.

(c) Overall minimum value of n_{gdl} as a function of the final point. The dashed line corresponding to the value of $n_{gdl,min}$ for $\xi = 0$ also corresponds to the minimum value of n required by the horizontal motion for all $\xi \in [0, 1]$.

Figure 1.11 – Optimal inclination and its corresponding value of n for a trajectory performed with the zero-tension amplitude function for horizontal trajectories.

1.11 Bibliography

J. Albus, R. Bostelman, and N. Dagalakis. The NIST Robocrane. *Journal of Robotic Systems*, 10(5):709–724, 1993. ISSN 07412223. doi:10.1002/rob.4620100509.

A. B. Alp and S. K. Agrawal. Cable suspended robots: Design, planning and control. In *Proceedings of the IEEE International Conference on Robotics and Automation*, volume 4, pages 4275–4280, Washington, DC, USA, 2002. doi:10.1109/ROBOT.2002.1014428.

G. Barrette and C. M. Gosselin. Determination of the dynamic workspace of cable-driven planar parallel mechanisms. *Journal of Mechanical Design, Transactions of the ASME*, 127 (2):242–248, 2005. ISSN 10500472. doi:10.1115/1.1830045.

A. Berti, M. Gouttefarde, and M. Carricato. Dynamic recovery of cable-suspended parallel robots after a cable failure. In *Proceedings of the 2016 ARK Conference*, pages 338–344, 2016.

S. Bouchard and C. Gosselin. A gravity-powered mechanism for extending the workspace of a cable-driven parallel mechanism: Application to the appearance modelling of objects. *International Journal of Automation Technology*, 4(4):372–379, 2010.

L. L. Cone. Skycam: An aerial robotic camera system. *Byte*, 10(10):122–132, 1985. ISSN 03605280.

D. Cunningham and H. H. Asada. The winch-bot: A cable-suspended, under-actuated robot utilizing parametric self-excitation. In *Proceedings of the 2009*

IEEE International Conference on Robotics and Automation, pages 1844–1850, 2009. doi:10.1109/ROBOT.2009.5152378.

C. Gosselin. Global planning of dynamically feasible trajectories for three-dof spatial cable-suspended parallel robots. In T. Bruckmann and A. Pott, editors, *Cable-Driven Parallel Robots*, pages 3–22. Springer Berlin Heidelberg, Berlin, Heidelberg, 2013. ISBN 978-3-642-31988-4. doi:10.1007/978-3-642-31988-4_1.

C. Gosselin and S. Foucault. Dynamic point-to-point trajectory planning of a two-dof cable-suspended parallel robot. *IEEE Transactions on Robotics*, 30(3):728 – 736, 2014. ISSN 1552-3098. doi:10.1109/TRO.2013.2292451.

C. Gosselin, P. Ren, and S. Foucault. Dynamic trajectory planning of a two-dof cable-suspended parallel robot. In *Proceedings of the IEEE International Conference on Robotics and Automation*, pages 1476–1481, St. Paul, MN, USA, 2012. doi:10.1109/ICRA.2012.6224683.

M. Gouttefarde, S. Krut, F. Pierrot, and N. Ramdani. On the design of fully constrained parallel cable-driven robots. In *Advances in Robot Kinematics: Analysis and Design*, pages 71–78. Springer Netherlands, Dordrecht, 2008. ISBN 978-1-4020-8599-4. doi:10.1007/978-1-4020-8600-7_8.

X. Jiang and C. Gosselin. Dynamically feasible trajectories for three-dof planar cable-suspended parallel robots. In *Proceedings of the ASME Design Engineering Technical Conference*, volume 5A, Buffalo, NY, USA, 2014. doi:10.1115/DETC2014-34419. V05AT08A085.

X. Jiang and C. Gosselin. Dynamic point-to-point trajectory planning of a three-dof cable-suspended parallel robot. *IEEE Transactions on Robotics*, 32(6):1550–1557, Dec 2016. ISSN 1552-3098. doi:10.1109/TRO.2016.2597315.

S. Lefrançois and C. Gosselin. Point-to-point motion control of a pendulum-like 3-dof underactuated cable-driven robot. In *Proceedings of the IEEE International Conference on Robotics and Automation*, pages 5187–5193, Anchorage, AK, USA, 2010. doi:10.1109/ROBOT.2010.5509656.

W. B. Lim, G. Yang, S. H. Yeo, S. K. Mustafa, and I. M. Chen. A generic tension-closure analysis method for fully-constrained cable-driven parallel manipulators. In *Proceedings of the IEEE International Conference on Robotics and Automation*, pages 2187–2192, May 2009. doi:10.1109/ROBOT.2009.5152772.

K. D. Nguyen, T.-C. Ng, and I.-M. Chen. On algorithms for planning s-curve motion profiles. *International Journal of Advanced Robotic Systems*, 5(1):99–106, 2008. ISSN 17298806. doi:10.5772/5652.

J. Pusey, A. Fattah, S. Agrawal, and E. Messina. Design and workspace analysis of a 6-6 cable-suspended parallel robot. *Mechanism and Machine Theory*, 39(7):761–778, 2004. ISSN 0094114X. doi:10.1016/j.mechmachtheory.2004.02.010.

A. T. Riechel and I. Ebert-Uphoff. Force-feasible workspace analysis for under-constrained, point-mass cable robots. In *Proceedings of the IEEE International*

Conference on Robotics and Automation, volume 5, pages 4956–4962, April 2004. doi:10.1109/ROBOT.2004.1302503.

V. Schmidt, W. Kraus, W. Y. Ho, J. Seon, A. Pott, J.-O. Park, and A. Verl. Extending dynamic trajectories of cable-driven parallel robots as a novel robotic roller coaster. In *Proceedings for the Joint Conference of ISR 2014 - 45th International Symposium on Robotics and Robotik 2014 - 8th German Conference on Robotics, ISR/ROBOTIK 2014*, pages 367–373, Munich, Germany, 2014.

A. Trevisani. Underconstrained planar cable-direct-driven robots: A trajectory planning method ensuring positive and bounded cable tensions. *Mechatronics*, 20(1):113–127, 2010. ISSN 09574158. doi:10.1016/j.mechatronics.2009.09.011.

D. Zanotto, G. Rosati, and S. Agrawal. Modeling and control of a 3-dof pendulum-like manipulator. In *Proceedings of the IEEE International Conference on Robotics and Automation*, pages 3964–3969, Shanghai, China, 2011. doi:10.1109/ICRA.2011.5980198.

N. Zhang and W. Shang. Dynamic trajectory planning of a 3-dof under-constrained cable-driven parallel robot. *Mechanism and Machine Theory*, 98:21–35, 2016. ISSN 0094-114X. doi:10.1016/j.mechmachtheory.2015.11.007.

N. Zoso and C. Gosselin. Point-to-point motion planning of a parallel 3-dof underactuated cable-suspended robot. In *Proceedings of the IEEE International Conference on Robotics and Automation*, pages 2325–2330, St. Paul, MN, USA, 2012. doi:10.1109/ICRA.2012.6224598.

Chapitre 2

Dynamic point-to-point trajectory planning of a three-dof cable-suspended mechanism using the hypocycloid curve

2.1 Résumé

Cet article propose une planification de trajectoire pour le mouvement point à point de mécanismes à câbles suspendus spatiaux à 3 ddl. Le tracé de la trajectoire consiste en une courbe hypocycloïdale inscrite dans le plan défini par le vecteur d'accélération au point initial et le point final. Le mouvement résultant assure une vitesse instantanée nulle à chacun des points cibles et la continuité de l'accélération, alors que les forces de tension dans les câbles sont garanties par un choix judicieux du nombre d'arcs de l'hypocycloïde. La formulation de trajectoire proposée peut être utilisée en séquence pour relier consécutivement des points cibles qui peuvent se trouver à l'extérieur de l'espace de travail statique du mécanisme. Comparativement à d'autres approches présentées dans le passé, la technique développée dans cet article produit de très grandes régions de points atteignables. En particulier, il est démontré que les trajectoires horizontales sont nécessairement réalisables, et ce peu importe la position des points cibles à atteindre. Des résultats de simulation d'une trajectoire exemple sont présentés afin d'illustrer l'approche proposée, et une démonstration vidéo d'une validation expérimentale réalisée sur un prototype est incluse.

2.2 Abstract

This paper proposes a dynamic trajectory planning technique for the point-to-point motion of three-degree-of-freedom (three-dof) cable-suspended mechanisms. The trajectory path is

inspired from a hypocycloid curve that is embedded in the plane defined by the acceleration vector at the initial point and the final point. The proposed motion ensures zero instantaneous velocity at each of the endpoints and continuity of the acceleration, while positive cable tensions are guaranteed through a proper choice of the number of arcs of the hypocycloid. The trajectory can be used in sequence to connect consecutive target points that may lie beyond the static workspace of the mechanism. Compared to previously proposed approaches, the technique developed in this paper produces very large regions of attainable target points. In particular, it is proven that horizontal trajectories are always feasible, for any prescribed target point. Simulation results of an example trajectory are included in order to illustrate the approach, along with a video demonstration of an experimental validation performed using a prototype.

2.3 Introduction

A cable-suspended parallel mechanism consists of a platform that is suspended by cables, and that is put into motion by the winding and unwinding of these cables on their respective servo-controlled winch. Unlike fully constrained cable-driven parallel mechanisms that have more cables than dofs (see for instance Lim et al., 2009; Gouttefarde et al., 2008; and many others), cable-suspended mechanisms have the same number of cables as dofs and rely on gravity to maintain tension in the cables. Cable-suspended parallel mechanisms can be used in applications that require very large workspaces, such as cranes (Albus et al., 1993) or camera support systems (Cone, 1985). Examples of some of the first cable-suspended mechanisms are presented in Alp and Agrawal (2002); Pusey et al. (2004); Bouchard and Gosselin (2010). More recent cable-suspended mechanisms that deal with trajectory planning were studied in Korayem and Tourajizadeh (2011); Kevac et al. (2017).

In most cases reported in the literature, cable-suspended mechanisms are assumed to work in static or quasi-static conditions, which implies that their workspace—referred to as the static workspace (Riechel and Ebert-Uphoff, 2004)—is limited by the footprint of the mechanism. However, using the notion of dynamic workspace (Barrette and Gosselin, 2005), it is possible to envision the dynamic control of cable-suspended parallel mechanisms. The dynamic workspace is defined as the set of poses that the platform can reach with a controlled kinematic state (position, velocity and acceleration) while maintaining all cables under tension.

In this context, the planning of trajectories that extend beyond the static workspace was first developed for underactuated cable-suspended mechanisms (Cunningham and Asada, 2009; Lefrançois and Gosselin, 2010; Zanotto et al., 2011; Zoso and Gosselin, 2012). To avoid the online numerical integration of the dynamic equations, trajectory planning approaches for fully actuated cable-suspended mechanisms were later proposed. In this case, since all dofs can be controlled, cable tension constraints are accounted for at the trajectory planning

stage instead of in the control loop, which makes the trajectory feasibility verification more transparent. In Gosselin et al. (2012); Gosselin (2013); Jiang and Gosselin (2014, 2016a), periodic trajectories were designed as a first attempt to explore the dynamic workspace. In practice however, cable-suspended mechanisms are most likely required to connect target points in sequence with a zero instantaneous velocity at each of the points. Dynamic point-to-point trajectory planning that satisfy these boundary conditions while maintaining cable tension was thereafter addressed in Gosselin and Foucault (2014); Jiang and Gosselin (2016b); Dion-Gauvin and Gosselin (2017).

In this paper, a dynamic point-to-point trajectory formulation is developed for a fully actuated spatial three-dof mechanism with a point mass end-effector. The proposed motion connecting two points in the dynamic workspace of the mechanism ensures zero instantaneous velocity at each of the endpoints as well as continuity of the acceleration to avoid undesirable discontinuous cable forces. The proposed motion is based on a hypocycloid curve, whereby the number of arcs of the hypocycloid is determined such that positive cable tension is guaranteed throughout the trajectory. The proposed trajectory can be used in sequence to connect a series of target points consecutively.

This paper provides an alternative approach to the point-to-point trajectory planning technique for three-dof cable-suspended mechanisms presented in Jiang and Gosselin (2016b) that alleviates the drawbacks of the latter while featuring new advantages. Specifically, the introduction of a free variable in the proposed formulation, namely the number of arcs of the hypocycloid, produces attainable regions of target points that are much larger, thus making less frequent the need to introduce an intermediate point to reach the desired final point. Moreover, the use of the pendulum constraints (Dion-Gauvin and Gosselin, 2017) allows to naturally derive an expression for the duration of the trajectory, which is an improvement over Jiang and Gosselin (2016b) wherein it is chosen heuristically. Finally, a sufficient but not necessary condition for trajectory feasibility is developed, which gives an indication of the feasibility of the motion. This test allows to demonstrate that this new formulation produces feasible horizontal trajectories for any target point.

As pointed out in Gosselin and Foucault (2014), cable-suspended mechanisms that can move outside of their static workspace can be very useful in applications where the footprint of the mechanism is limited by obstacles. Pick-and-place operations can be performed with such mechanisms. Also, mechanisms with such dynamic capabilities can find applications in entertainment systems or in the production of artistic performances.

This paper is structured as follows. Section 2.4 presents the kinematic and dynamic modelling of the three-dof mechanism. Section 2.5 describes the trajectory plane, in which any plane curve connecting the initial point to the final point is located. Section 2.6 introduces the formulation of the hypocycloid curve, which is the plane curve upon which the trajectory

is built, while Section 2.7 formally describes the time-based motion. Section 2.8 addresses the determination of the number of arcs of the hypocycloid that ensures positive tension in the cables along the motion. Section 2.9 provides simulation results of an example trajectory that connects a series of target points in sequence. Finally, a video demonstrating the implementation on a prototype is provided in order to validate the approach.

2.4 Mechanism Modelling

A spatial 3-dof cable-suspended mechanism is represented schematically in Fig. 2.1. The mechanism consists of three actuated spools mounted on a fixed structure which are used to control the extension of three cables. The cables are attached to a common end-effector which is considered as a point mass. By controlling the extension of the cables, the position of the point mass in a three-dimensional space can be controlled. The mechanism includes three actuators and three degrees of freedom and is therefore fully actuated. However, constraints must be imposed on the trajectory of the end-effector in order to ensure that it is feasible, i.e., that the trajectory does not require compression forces in the cables.

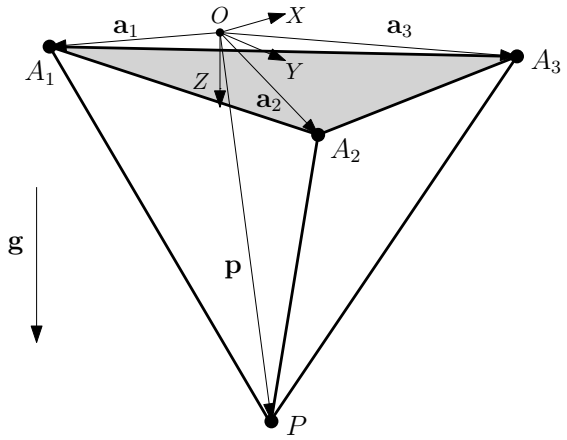

Figure 2.1 – Spatial three-dof cable-suspended mechanism.

Referring to the three-dof cable-suspended mechanism of Fig. 2.1, a fixed reference frame is first defined on the base of the mechanism. The Z axis of this reference frame points downwards, i.e., in the direction of gravity. The points corresponding to the cable outputs of the spools are noted A_k, $k = 1, 2, 3$, and the vector connecting the origin of the mechanism's fixed reference frame to point A_k is noted $\mathbf{a}_k$. The position vector of the end-effector of mass m with respect to the origin of the fixed reference frame is noted $\mathbf{p} = [x, y, z]^T$. The cable lengths, which are used as joint coordinates, are respectively noted ρ_k, $k = 1, 2, 3$. The inverse kinematic model can therefore be simply written as

$$\rho_k = \sqrt{(\mathbf{a}_k - \mathbf{p})^T(\mathbf{a}_k - \mathbf{p})}, \quad k = 1, 2, 3. \tag{2.1}$$

Since the mass and elasticity of the cables are neglected, the dynamic model of the mechanism is obtained by considering the force balance on the point-mass end-effector, namely (Gosselin, 2013)

$$\sum_{k=1}^{3}\left(\frac{\mathbf{a}_k-\mathbf{p}}{\rho_k}\right)f_k+m\mathbf{g}=m\ddot{\mathbf{p}}, \tag{2.2}$$

where f_k is the tension in cable k, and $\mathbf{g}=\begin{bmatrix}0 & 0 & g\end{bmatrix}^T$ is the vector of gravitational acceleration. Equation (2.2) can be rewritten in matrix form as

$$\mathbf{M}\boldsymbol{\mu}=\ddot{\mathbf{p}}-\mathbf{g}, \tag{2.3}$$

with

$$\boldsymbol{\mu}=\frac{1}{m}\begin{bmatrix}\frac{f_1}{\rho_1} & \frac{f_2}{\rho_2} & \frac{f_3}{\rho_3}\end{bmatrix}^T, \tag{2.4}$$

and where matrix $\mathbf{M}$ is defined as

$$\mathbf{M}=\begin{bmatrix}\boldsymbol{\rho}_1 & \boldsymbol{\rho}_2 & \boldsymbol{\rho}_2\end{bmatrix}, \tag{2.5}$$

with

$$\boldsymbol{\rho}_k=\mathbf{a}_k-\mathbf{p}, \qquad k=1,2,3. \tag{2.6}$$

Solving eq. (2.3) for vector $\boldsymbol{\mu}$ yields expressions for the cable forces, which must be positive to ensure dynamically feasible trajectories. One obtains

$$\boldsymbol{\mu}=\mathbf{M}^{-1}(\ddot{\mathbf{p}}-\mathbf{g})\succeq\mathbf{0}, \tag{2.7}$$

where $\succeq$ stands for the componentwise inequality. The inverse of matrix $\mathbf{M}$ is given by

$$\mathbf{M}^{-1}=\frac{\mathrm{Adj}(\mathbf{M})}{\det(\mathbf{M})}, \tag{2.8}$$

where $\mathrm{Adj}\,(\mathbf{M})$ stands for the adjoint matrix of $\mathbf{M}$ and $\det\,(\mathbf{M})$ is its determinant. Referring to eq. (2.5), the latter is given by

$$\det\,(\mathbf{M})=(\boldsymbol{\rho}_1\times\boldsymbol{\rho}_2)^T\boldsymbol{\rho}_3. \tag{2.9}$$

It can be noted, from eq. (2.9), that the determinant is positive as long as the end-effector remains below the plane passing through the fixed cable spools. This assumption is used here to simplify the positive tension constraints (2.7), yielding

$$\boldsymbol{\kappa}=\mathrm{Adj}(\mathbf{M})(\ddot{\mathbf{p}}-\mathbf{g})\succeq\mathbf{0}, \tag{2.10}$$

where the quantities $\boldsymbol{\kappa}=\begin{bmatrix}\kappa_1 & \kappa_2 & \kappa_3\end{bmatrix}^T$, referred to as pseudotensions, bear the same sign as the cable tensions and are introduced to simplify the analysis. The adjoint matrix of $\mathbf{M}$ being given by

$$\mathrm{Adj}(\mathbf{M})=\begin{bmatrix}(\boldsymbol{\rho}_2\times\boldsymbol{\rho}_3)^T\\(\boldsymbol{\rho}_3\times\boldsymbol{\rho}_1)^T\\(\boldsymbol{\rho}_1\times\boldsymbol{\rho}_2)^T\end{bmatrix}, \tag{2.11}$$

the pseudotensions can be expanded in the form (Gosselin, 2013)

$$\kappa_1 = [\mathbf{p} \times (\mathbf{a}_2 - \mathbf{a}_3) + (\mathbf{a}_2 \times \mathbf{a}_3)]^T (\ddot{\mathbf{p}} - \mathbf{g}) > 0 \tag{2.12}$$

$$\kappa_2 = [\mathbf{p} \times (\mathbf{a}_3 - \mathbf{a}_1) + (\mathbf{a}_3 \times \mathbf{a}_1)]^T (\ddot{\mathbf{p}} - \mathbf{g}) > 0 \tag{2.13}$$

$$\kappa_3 = [\mathbf{p} \times (\mathbf{a}_1 - \mathbf{a}_2) + (\mathbf{a}_1 \times \mathbf{a}_2)]^T (\ddot{\mathbf{p}} - \mathbf{g}) > 0. \tag{2.14}$$

The above inequalities represent the necessary and sufficient conditions to be satisfied in order to ensure that the cables are kept under tension. Therefore, satisfying the above inequalities at all points of a given trajectory ensures that the cables remain under tension throughout the trajectory.

2.4.1 Pendulum Constraint

As shown in Dion-Gauvin and Gosselin (2017), special kinematic states are obtained when the pseudotensions in the three cables are equal, namely

$$\kappa_1 = \kappa_2 = \kappa_3. \tag{2.15}$$

For such kinematic states, the resulting force produced by the three cables is directed toward the centroid of the cable spools, at the centre of the positive tension pyramid defined by the three cables. As a consequence, such kinematics states are the least likely to fall into negative tension states if an external disturbance were to occur and are thereby as dynamically stable as possible. It can be shown that such kinematic states satisfy the relation (Dion-Gauvin and Gosselin, 2017)

$$(\mathbf{p} - \mathbf{c}) \times (\ddot{\mathbf{p}} - \mathbf{g}) = \mathbf{0}, \tag{2.16}$$

where $\mathbf{c}$ stands for the position vector of the centroid of the cable spools. From a physical point of view, the foregone equation corresponds to the dynamic model, written in Cartesian coordinates, of a spatial pendulum suspended from point $\mathbf{c}$. Notably, a kinematic state that satifies eq. (2.16) has its acceleration vector pointing toward the vertical axis passing through the centroid of the cable spools. In dynamic trajectory planning, imposing this condition on end-point kinematic states maximizes the likelihood of obtaining feasible subsequent trajectory segments. This constraint is used in this manner in the proposed trajectory formulation.

2.4.2 Mechanism Architecture

The dynamic model and inequalities given above are general and do not assume a specific geometry. Moreover, the technique proposed here is general and can be applied to different mechanism geometries. However, in order to provide physical insight, a special symmetric mechanism architecture is used for the remainder of the paper. In this architecture, the three spools are located on the vertices of a horizontal equilateral triangle whose centroid is at the

origin of the fixed reference frame. The geometry is therefore defined as

$$\mathbf{a}_1 = \begin{bmatrix} \frac{\sqrt{3}a}{2} & -\frac{a}{2} & 0 \end{bmatrix}^T \tag{2.17}$$

$$\mathbf{a}_2 = \begin{bmatrix} -\frac{\sqrt{3}a}{2} & -\frac{a}{2} & 0 \end{bmatrix}^T \tag{2.18}$$

$$\mathbf{a}_3 = \begin{bmatrix} 0 & a & 0 \end{bmatrix}^T, \tag{2.19}$$

where a corresponds to the distance from one of the spools to the centroid. Substituting the above geometric parameters into inequalities (2.12) to (2.14), these inequalities can be rewritten as

$$\kappa_1 = -\frac{\sqrt{3}}{2}a\Big((a+\sqrt{3}x-y)(\ddot{z}-g)+z(\ddot{y}-\sqrt{3}\ddot{x})\Big) > 0 \tag{2.20}$$

$$\kappa_2 = -\frac{\sqrt{3}}{2}a\Big((a-\sqrt{3}x-y)(\ddot{z}-g)+z(\ddot{y}+\sqrt{3}\ddot{x})\Big) > 0 \tag{2.21}$$

$$\kappa_3 = -\frac{\sqrt{3}}{2}a\Big((a+2y)(\ddot{z}-g)-2z\ddot{y}\Big) > 0, \tag{2.22}$$

while the pendulum constraint (2.16), applied at the initial and final points of a point-to-point trajectory, is given in scalar form by:

$$\frac{\ddot{z}_j - g}{z_j} = \frac{\ddot{y}_j}{y_j} = \frac{\ddot{x}_j}{x_j}, \quad j = 1, 2, \tag{2.23}$$

where $j = 1$ refers to the initial point of the trajectory and $j = 2$ refers to its final point. In the next section, this relation is used to derive an expression for the acceleration at the endpoints of the trajectory.

2.5 Plane of the Trajectory

Let $\mathbf{p}_1$ and $\mathbf{p}_2$ be the position vectors of the initial and final points, respectively, and let $\ddot{\mathbf{p}}_1$ be the initial acceleration vector, which satisfies eq. (2.23) and which must correspond to the final acceleration of the preceding trajectory segment in order to ensure continuity in the cable forces. As it can be seen in Fig. 2.2, in three-dimensional space, the acceleration vector at the initial point (defining a line) as well as the final point (defining a point) define together a plane in which the proposed planar trajectory is embedded. The final acceleration vector $\ddot{\mathbf{p}}_2$, albeit undetermined yet, also lies in that plane. Let point $\mathbf{p}_0 = \begin{bmatrix} 0 & 0 & z_0 \end{bmatrix}^T$ be defined as the intersection of the trajectory plane with the Z axis. Since the initial and final acceleration vectors intersect the Z axis by virtue of eq. (2.23), they point toward point $\mathbf{p}_0$ and thereby can be written as

$$\ddot{\mathbf{p}}_j = -\lambda_j(\mathbf{p}_j - \mathbf{p}_0), \qquad j = 1, 2, \tag{2.24}$$

where the known parameter λ_1 and the undetermined parameter λ_2 are positive definite. The foregone equation can be rewritten in scalar form as

$$\lambda_j = -\frac{\ddot{z}_j}{z_j - z_0} = -\frac{\ddot{x}_j}{x_j} = -\frac{\ddot{y}_j}{y_j}, \qquad j = 1, 2. \tag{2.25}$$

Comparing eq. (2.25) with eq. (2.23) leads to expressions for z_0, namely:

$$z_0 = \frac{g}{g - \ddot{z}_j} z_j = \frac{g}{\lambda_j}, \qquad j = 1, 2, \tag{2.26}$$

and its value can be directly obtained by setting $j = 1$. Moreover, the value of z_0 being unique, eq. (2.26) leads to:

$$\lambda_1 = \lambda_2 = \lambda. \tag{2.27}$$

The above equation states that, by virtue of eq. (2.23) and of the trajectory being constrained to a plane, the final acceleration—and, in a context of point-to-point trajectory planning constructed as a sequence of trajectory segments, the acceleration at each subsequent target point—is no longer a free parameter but is rather completely determined by the initial kinematic state.

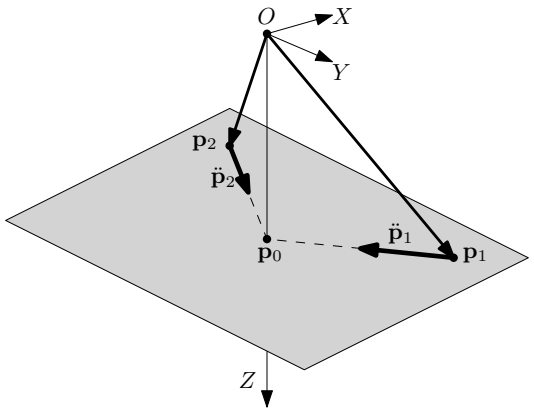

Figure 2.2 – Plane of the trajectory. The trajectory plane is defined by the quantities that are prescribed from the outset, i.e., the initial and final point, as well as the acceleration vector at the initial point. For the trajectory to be planar, the final acceleration vector must also lie in the plane.

A planar fixed reference frame is defined on the trajectory plane, whose origin is chosen to be at point $\mathbf{p}_0$ and whose X_h axis points in the direction of the initial point. The Y_h axis of this reference frame is located in the half of the trajectory plane that contains the final point (and is orthogonal to the X_h axis). The trajectory plane is spanned by vectors $(\mathbf{p}_1 - \mathbf{p}_0)$ and $(\mathbf{p}_2 - \mathbf{p}_0)$. This can be expressed by matrix $\mathbf{A}$, defined as

$$\mathbf{A} = \begin{bmatrix} (\mathbf{p}_1 - \mathbf{p}_0) & (\mathbf{p}_2 - \mathbf{p}_0) \end{bmatrix}. \tag{2.28}$$

Hence the matrix that maps the XY-plane of the mechanism reference frame onto the trajectory reference frame, denoted $\mathbf{Q}_h$, is composed of the first two columns of the orthogonal matrix obtained in the QR decomposition of $\mathbf{A}$. By virtue of the Gram-Schmidt process, this matrix is given by:

$$\mathbf{Q}_h = \begin{bmatrix} \mathbf{q}_{h1} & \mathbf{q}_{h2} \end{bmatrix}, \tag{2.29}$$

with

$$\mathbf{q}_{h1} = \frac{\mathbf{p}_1 - \mathbf{p}_0}{\|\mathbf{p}_1 - \mathbf{p}_0\|} \qquad \mathbf{q}_{h2} = \frac{(\mathbf{1} - \mathbf{q}_{h1}\mathbf{q}_{h1}^T)(\mathbf{p}_2 - \mathbf{p}_0)}{\|(\mathbf{1} - \mathbf{q}_{h1}\mathbf{q}_{h1}^T)(\mathbf{p}_2 - \mathbf{p}_0)\|}. \tag{2.30}$$

Hence, let $\mathbf{c} \in \mathbb{R}^2$ be a vector written in the trajectory reference frame and let $\mathbf{p} \in \mathbb{R}^3$ be the same vector written in the mechanism reference frame, one has:

$$\mathbf{p} = \mathbf{Q}_h\mathbf{c} + \mathbf{p}_0. \tag{2.31}$$

This relation is used in the following to write the parametric trajectory in the mechanism reference frame.

2.6 Hypocycloid Curve

In the trajectory plane, it is proposed that the point-to-point motion be following a hypocycloidal path. This curve has cusps that can be matched to the trajectory endpoints to satisfy the zero velocity constraints. The general parametric equations for a hypocycloid curve having a cusp at point $(1, 0)$ can be written as (Lawrence, 1972)

$$u(\tau) = \frac{(n_h - 1)\cos(\theta_h\tau) + \cos((n_h - 1)\theta_h\tau)}{n_h} \tag{2.32}$$

$$v(\tau) = \frac{(n_h - 1)\sin(\theta_h\tau) - \sin((n_h - 1)\theta_h\tau)}{n_h}, \tag{2.33}$$

where $u(\tau)$ and $v(\tau)$ are the parametric equations in the X_h and Y_h directions respectively, angle θ_h is the plotting range of the curve, and $\tau \in [0, 1]$ is the normalized parametric coordinate. Parameter $n_h \geq 2$ that appears in eqs. (2.32) and (2.33) corresponds to the number of arcs (cusps) that the curve traces (reaches) over one lap before closing in on itself. Figure 2.3 illustrates the hypocycloid curve for $\theta_h = -\frac{4\pi}{3}$ and $n_h = 3$.

As it can be seen from Fig. 2.3, the hypocycloid curve can be easily adjusted to be used as a point-to-point trajectory with an arbitrary number of arcs $p \in \mathbb{N}^+$ by matching two of its cusps to the trajectory endpoints. Expressing angle θ_h and parameter n_h as functions of the number of arcs yields

$$\theta_h = \psi_h + (-1)^{p-1}2\pi\left\lceil\frac{p-1}{2}\right\rceil \qquad p = 1, 2, 3, ..., \tag{2.34}$$

and

$$n_h = \frac{2\pi p}{|\theta_h|} \qquad p = 1, 2, 3, \ldots . \tag{2.35}$$

In eq. (2.34), angle ψ_h is the smallest angle formed by vectors $(\mathbf{p}_1 - \mathbf{p}_0)$ and $(\mathbf{p}_2 - \mathbf{p}_0)$, namely:

$$\psi_h = \arccos\left(\frac{(\mathbf{p}_1 - \mathbf{p}_0)^T(\mathbf{p}_2 - \mathbf{p}_0)}{\|(\mathbf{p}_1 - \mathbf{p}_0)\|\,\|(\mathbf{p}_2 - \mathbf{p}_0)\|}\right). \tag{2.36}$$

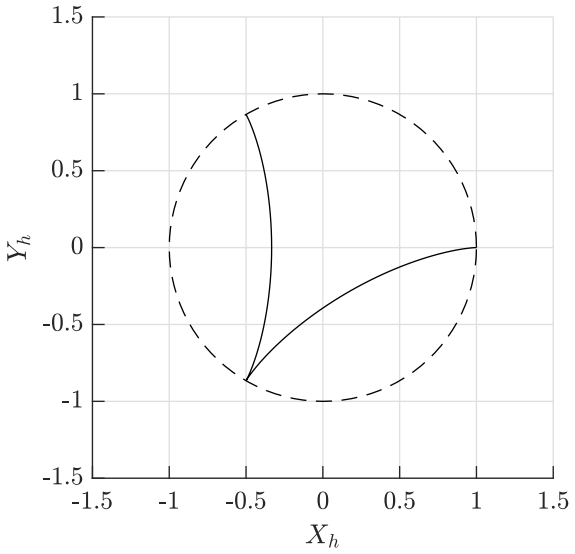

Figure 2.3 – Hypocycloid curve for $\theta_h = -\frac{4\pi}{3}$ and $n_h = 3$. The curve has 2 arcs over 2/3 laps, yielding $n_h = 3$.

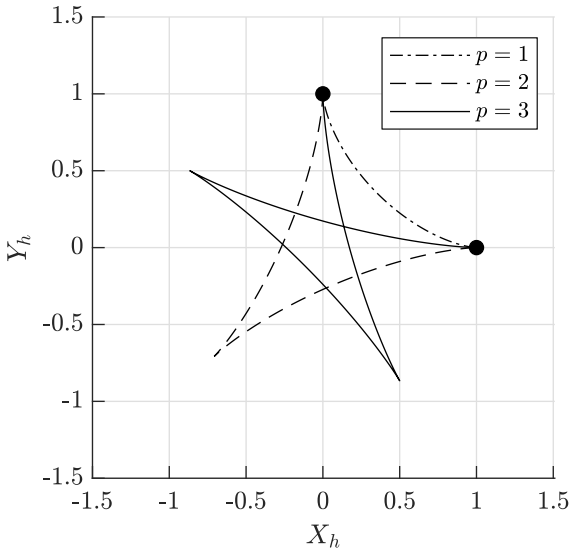

Figure 2.4 – Hypocycloid curve connecting two points having $\psi_h = \frac{\pi}{2}$ with one, two, and three arcs respectively.

Figure 2.4 illustrates the hypocycloid curve connecting two points having $\psi_h = \frac{\pi}{2}$ with one, two, and three arcs respectively. The advantage of this formulation is that as the number of arcs p increases, so does the likelihood of generating a feasible curve. Specifically, computing the limit of parameter n_h as the number of arcs approaches infinity yields

$$\lim_{p \to \infty} n_h = 2. \tag{2.37}$$

A hypocycloid curve admitting a value of $n_h = 2$ arcs per lap has each of its arcs being rectilinear and running parallel to the acceleration vector at its cusp. For this reason, one

could conjecture that a point-to-point trajectory based on the hypocycloid curve induces strictly positive cable tensions at all points of the motion as $p \to \infty$. This assumption is verified in Section 2.8.1.

2.7 Proposed Trajectory

Considering the hypocyloid curve defined in the preceding section, the proposed trajectory is given, in its reference frame, by:

$$\mathbf{c}(t) = \begin{bmatrix} r(\tau)u(\tau) \\ r(\tau)v(\tau) \end{bmatrix} \qquad \text{with} \qquad \tau = \frac{t}{T}, \tag{2.38}$$

where t is the time, T is the duration of the trajectory, and $r(\tau)$ is an amplitude function that allows to connect points located at different distances from the origin of the trajectory plane. Defining

$$r_1 = \|\mathbf{p}_1 - \mathbf{p}_0\| \qquad\qquad r_2 = \|\mathbf{p}_2 - \mathbf{p}_0\|, \tag{2.39}$$

the proposed trajectory must meet boundary conditions that can be written as

$$\mathbf{c}(0) = \begin{bmatrix} r_1 \\ 0 \end{bmatrix}, \qquad\qquad \dot{\mathbf{c}}(0) = \mathbf{0}, \qquad \ddot{\mathbf{c}}(0) = -\lambda \mathbf{c}(0), \tag{2.40}$$

and

$$\mathbf{c}(1) = \begin{bmatrix} r_2 \cos(\theta_h) \\ r_2 \sin(\theta_h) \end{bmatrix}, \qquad \dot{\mathbf{c}}(1) = \mathbf{0}, \qquad \ddot{\mathbf{c}}(1) = -\lambda \mathbf{c}(1), \tag{2.41}$$

where the acceleration constraints of eqs. (2.40) and (2.41) are obtained using eq. (2.24) along with eq. (2.31). On the other hand, the first two derivatives of eq. (2.38) are given by:

$$\dot{\mathbf{c}}(t) = \frac{\begin{bmatrix} r'(\tau)u(\tau) + r(\tau)u'(\tau) \\ r'(\tau)v(\tau) + r(\tau)v'(\tau) \end{bmatrix}}{T} \tag{2.42}$$

and

$$\ddot{\mathbf{c}}(t) = \frac{\begin{bmatrix} r''(\tau)u(\tau) + 2r'(\tau)u'(\tau) + r(\tau)u''(\tau) \\ r''(\tau)v(\tau) + 2r'(\tau)v'(\tau) + r(\tau)v''(\tau) \end{bmatrix}}{T^2}, \tag{2.43}$$

where $f'(\cdot)$ stands for the derivative of f with respect to its argument. Moreover, referring to eqs. (2.32) and (2.33), it can be easily found that:

$$\begin{aligned} &u(0) = 1, \qquad u(1) = \cos(\theta_h), \qquad u'(0) = u'(1) = 0, \\ &u''(0) = -\theta_h^2(n_h - 1), \qquad u''(1) = -\theta_h^2(n_h - 1)\cos(\theta_h), \end{aligned} \tag{2.44}$$

and

$$\begin{aligned} &v(0) = 0, \qquad v(1) = \sin(\theta_h), \qquad v'(0) = v'(1) = 0, \\ &v''(0) = 0, \qquad v''(1) = -\theta_h^2(n_h - 1)\sin(\theta_h). \end{aligned} \tag{2.45}$$

Considering eqs. (2.44) and (2.45), the substitution of eqs. (2.40) and (2.41) into eqs. (2.38), (2.42), and (2.43) leads to

$$r(0) = r_1, \qquad r(1) = r_2, \qquad r'(0) = r'(1) = r''(0) = r''(1) = 0, \tag{2.46}$$

and

$$T^2 = \frac{\theta_h^2(n_h - 1)}{\lambda}, \tag{2.47}$$

where it can be seen that the duration of the trajectory is positive definite, as desired. Considering eq. (2.46), the amplitude function $r(\tau)$ can be rewritten as

$$r(\tau) = (r_2 - r_1)A(\tau) + r_1, \tag{2.48}$$

where $A(\tau)$ is any normalized amplitude function that satisfies the boundary conditions

$$A(0) = 0, \qquad A(1) = 1, \qquad A'(0) = A'(1) = A''(0) = A''(1) = 0, \tag{2.49}$$

such as

$$A(\tau) = 6\tau^5 - 15\tau^4 + 10\tau^3, \tag{2.50}$$

which is the polynomial function of minimal degree that satisfies eq. (2.49) (Gosselin and Hadj-Messaoud, 1993). This amplitude function is used in the example trajectory of Section 2.9.

2.8 Trajectory Feasibility

As shown above, the selection of a proper amplitude function ensures that the trajectory meets all end-point kinematic conditions. However, it is left to verify that the tensions in the cables remain positive throughout the motion. To this end, the parametric trajectory given by eq. (2.38) is first written in the mechanism reference frame using eq. (2.31). The resulting expression and its second time derivative are thereafter substituted into the pseudotensions, eqs. (2.20)–(2.22). Finally, the duration of the trajectory T is eliminated from the set of equations using eq. (2.47), yielding pseudotensions that can be written as

$$\begin{aligned} \kappa_k = \frac{\sqrt{3}}{2}ga^2 - E_k + A_k\cos(\theta_h\tau) + B_k\sin(\theta_h\tau) + C_k\cos((n_h - 1)\theta_h\tau) + \\ D_k\sin((n_h - 1)\theta_h\tau) + E_k\cos(n_h\theta_h\tau) + F_k\sin(n_h\theta_h\tau), \qquad k = 1, 2, 3, \end{aligned} \tag{2.51}$$

where the expressions for coefficients $A_k, B_k, ..., F_k$, are too cumbersome to be explicited here but depend on z_0, matrix $\mathbf{Q}_h$, the amplitude function $r(\tau)$, and the number of arcs p. While the former three parameters are obtained using eqs. (2.26), (2.29), and (2.46) respectively,

the latter, i.e., the minimum number of arcs p that yields strictly positive cable tension, if it exists, is determined by computing eq. (2.51) with a candidate value and by ensuring that the three expressions are positive on the considered time interval. Starting with $p = 1$, the candidate for minimum feasible number of arcs is either conserved if all the pseudotensions are positive on $\tau \in [0, 1]$, or increased by one if otherwise. This process is repeated until a feasible number of arcs is found, or until the candidate value is deemed unfit (too large) to be used in practice.

2.8.1 Feasibility at Infinity

It was seen previously that, as the number of arcs increases, each arc of the hypocycloid curve tends to become rectilinear and to run parallel to the acceleration vector at its cusp, which increases the likelihood of obtaining a feasible trajectory. In this section, the pseudotensions in the cables are investigated as $p \to \infty$. First, the linear combination of the sine and cosine functions in eq. (2.51) can be rewritten as

$$\begin{aligned}\kappa_k = \frac{\sqrt{3}}{2} g a^2 - E_k + \sqrt{{A_k}^2 + {B_k}^2}\cos(\theta_h \tau + \alpha_k) + \\ \sqrt{{C_k}^2 + {D_k}^2}\cos((n_h - 1)\theta_h \tau + \beta_k) + \sqrt{{E_k}^2 + {F_k}^2}\cos(n_h \theta_h \tau + \gamma_k), \quad k = 1, 2, 3,\end{aligned} \tag{2.52}$$

where α_k, β_k, and γ_k, $k = 1, 2, 3$, are phase shifts. Given the bounds on trigonometric functions, the pseudotensions are positive definite if

$$\kappa_{e,k} = \frac{\sqrt{3}}{2} g a^2 - |E_k| - \sqrt{{A_k}^2 + {B_k}^2} - \sqrt{{C_k}^2 + {D_k}^2} - \sqrt{{E_k}^2 + {F_k}^2} > 0, \quad k = 1, 2, 3. \tag{2.53}$$

The above expressions represent the time-dependent lower envelope of the pseudotensions. On the considered time interval, these inequalities constitute a sufficient (but not necessary) condition for positive cable tensions. While using eq. (2.53) to determine a feasible number of arcs p would provide a too conservative value, the pseudotension lower envelopes are well suited for taking the limit as p approaches infinity since they do not contain sine nor cosine functions. Hence computing this limit for each inequality of eq. (2.53) yields the unique expression for $k = 1, 2, 3$:

$$\lim_{p \to \infty} \kappa_{e,k} = \frac{\sqrt{3}}{2} g a^2 \left(1 - r(\tau) \frac{\sqrt{{q_{h31}}^2 + {q_{h32}}^2}}{z_0}\right) > 0, \tag{2.54}$$

where q_{h31} and q_{h32} are the corresponding components of matrix $\mathbf{Q}_h$. For a monotonic amplitude function such as that of eq. (2.50), the left-hand side of the above inequality reaches its minimum value over the considered time interval at either trajectory endpoints, i.e., at $\tau = 0$ or $\tau = 1$. Ensuring that this minimum is positive definite leads to

$$1 - \max(r_1, r_2) \frac{\sqrt{{q_{h31}}^2 + {q_{h32}}^2}}{z_0} > 0. \tag{2.55}$$

The above equation corresponds to a circle of radius $r = \max(r_1, r_2)$ centred at the origin of the trajectory plane $\mathbf{p}_0$—which is illustrated in Fig. 2.3 for $r = 1$—that must be completely located below the spools for the inequality to be satisfied. Ensuring that eq. (2.55) is verified before computing the pseudotensions at each instant of the trajectory implies that a finite feasible number of arcs p can be found. However, since the above condition is predicated on the pseudotension lower envelopes constituting a sufficient but not necessary condition for trajectory feasibility, a number of arcs p may still exist when the above test fails.

2.8.2 Horizontal Trajectory

A horizontal trajectory occurs when the initial point, the final point and the initial acceleration vector are all located in the same horizontal plane. In such a case, computing matrix $\mathbf{Q}_h$ using eq. (2.29) leads to

$$q_{h31} = q_{h32} = 0, \tag{2.56}$$

and correspondingly eq. (2.55) becomes

$$1 > 0, \tag{2.57}$$

i.e., any horizontal trajectory is feasible. This is an important advantage of the proposed trajectory formulation. In particular, previously proposed formulations cannot guarantee such feasibility and generally fail for demanding horizontal trajectories. For example, the approach devised in Jiang and Gosselin (2016b) can only connect endpoints that are located at about the same distance from the central vertical axis—that is, having $r_1 \approx r_2$—and that form an angle ψ_h of about π radians. Hence the technique proposed here presents substantial improvements over existing formulations.

2.9 Example Trajectory

The proposed formulation was thoroughly validated in simulation for target points that are located asymetrically and at different distances with respect to the central vertical axis. This section presents the simulation that was performed experimentally to further verify the method. A prototype of a three-dof cable-suspended mechanism that was built for this purpose is shown in Fig. 2.5. Three servo-controlled winches are used to control the length of the cables. The distance between the centroid of the cable spools and one attachment point is $a = 0.26$ m, and the mass of the end-effector is $m = 0.198$ kg. The example trajectory is described in Table 2.1 as a list of target points that must be reached in sequence. At the beginning and at the end of the sequence, the first target point and the state of rest can be reached with either a transition trajectory (Dion-Gauvin and Gosselin, 2017) or the formulation proposed in this paper. Indeed, it can be shown that the point-to-point technique developed here reduces to the transition trajectories of Dion-Gauvin and Gosselin (2017) with

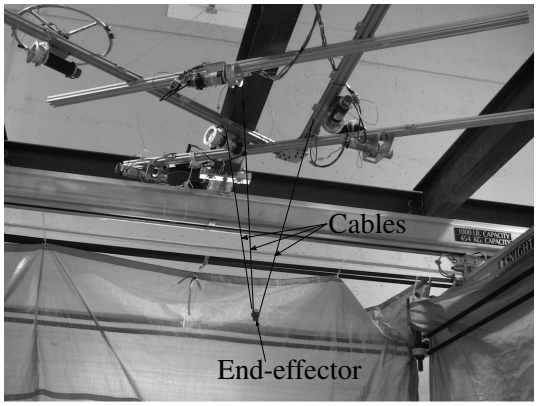

Figure 2.5 – Spatial 3-dof cable-suspended mechanism used to perform the experimental validation.

the appropriate changes of variables when either the initial point or the final point admits a zero acceleration.

Unlike in the modelling presented in the previous sections wherein the acceleration at point $\mathbf{p}_1$ is given, in practice no acceleration is imposed at the first of a sequence of target points. Referring to eq. (2.26), this implies that the position of point $\mathbf{p}_0$ in the static workspace can be chosen, and this selection governs the acceleration at each of the target points. Moreover, using point $\mathbf{p}_0$ as the static endpoint of the transition trajectories ensures continuity of the acceleration at the first and last target points.

In the selection of point $\mathbf{p}_0$, one approach consists in using a conservative value for z_0 that ensures from the outset that each segment is feasible. Considering the physical interpretation of eq. (2.55), such value for z_0 must satisfy, for a sequence of m target points noted $\mathbf{p}_1, \mathbf{p}_2, \ldots, \mathbf{p}_m$,

$$z_0 > \max\left(\frac{{\mathbf{p}_1}^T\mathbf{p}_1}{2z_1}, \frac{{\mathbf{p}_2}^T\mathbf{p}_2}{2z_2}, \ldots, \frac{{\mathbf{p}_m}^T\mathbf{p}_m}{2z_m}\right). \tag{2.58}$$

Therefore, provided that the value for z_0 satisfies the above constraint, strictly positive cable tension can be ensured throughout any trajectory described as a sequence of target points. However, depending on the target points chosen, such a value for z_0 might not be usable in practice, i.e., the motion that it yields, or even point $\mathbf{p}_0$ itself, may interfere with the floor. Besides, it may not lead to the most efficient motion, i.e., that which minimizes the minimum feasible number of arcs for each segment. Hence the decision on whether to use a value for z_0 that satisfies eq. (2.58) should be taken with discernment.

If a smaller value for z_0 is preferred, it should nevertheless be chosen sufficiently large such that none of the target points is proven from the outset to be unattainable. Referring to eq. (2.55), the value for z_0 must be larger that the half of the largest Z coordinate of all the

target points, i.e.:

$$z_0 > \max\left(\frac{z_1}{2}, \frac{z_2}{2}, \ldots, \frac{z_m}{2}\right). \tag{2.59}$$

Referring to the target points of Table 2.1, using the conservative value for z_0 provided by eq. (2.58) yielded trajectories that reached $z = 4.74$ m, whereas the floor was located at $z = 3.5$ m. Consequently, the average of the Z coordinate of the target points of Table 2.1 was calculated and, since it satisfies eq. (2.59), it was selected as the value for z_0 for the experimentation, yielding $\mathbf{p}_0 = \begin{bmatrix} 0 & 0 & 1.7 \end{bmatrix}^T$ m.

The value for z_0 being determined, matrix $\mathbf{Q}_h$, angle ψ_h, r_1, and r_2 are first calculated for each trajectory segment with eqs. (2.29), (2.36) and (2.39) respectively. The feasibility of each segment can then be verified using eq. (2.55), and the corresponding minimum feasible number of arcs is determined following the procedure explained in Section 2.8 for an amplitude function satisfying eq. (2.49). Table 2.1 shows the result of the feasibility test at infinity, the minimum feasible number of arcs, as well as the duration of each segment for $z_0 = 1.7$ m and the amplitude function given by eq. (2.50). As it can be seen, a feasible number of arcs can still exist when the feasibility test fails. In the event that a feasible number of arcs cannot be found to connect a given segment, another value for z_0 can be used, or intermediate points can be inserted in the sequence.

Target Point	Coordinates	$p \to \infty$	p	T(s)
1	(0.7, 0.7, 3)	-0.1557	5	6.54
2	(-1.1, -1.1, 0.5)	-0.1416	2	2.61
3	(-1.1, -0.9, 1.5)	0.2057	5	6.54
4	(0.8, 0.5, 1.5)	0.8208	5	6.53
5	(-0.6, 0.1, 1.9)	0.8494	5	6.52
6	(0.1, -0.6, 1.8)	0.5425	6	7.85
7	(0, -1.1, 1.7)	—	—	—

Table 2.1 – Feasibility test and minimum feasible number of arcs required for reaching the target points with $a = 0.26$ m, $z_0 = 1.7$ m, and for the amplitude function given by eq. (2.50).

The resulting trajectory, computed with the number of arcs of Table 2.1 along with eqs. (2.32), (2.33) and (2.31), is illustrated in Fig. 2.6, while Fig. 2.7 presents the tensions throughout the motion. It is clear from Fig. 2.6 that the end-effector reaches points that are located far beyond its static workspace. From Fig. 2.7, it can be observed that the tensions in the cables are continuous and positive at all instants of the trajectory.

In the experiment, the segment connecting the third and fourth target points was performed using 7 arcs instead of the minimum feasible value of 5 to reinforce that the value of p obtained from the procedure explained in Section 2.8 constitutes a lower bound for the feasible number of arcs. (The number of arcs was increased by an even number to ensure that angle θ_h given

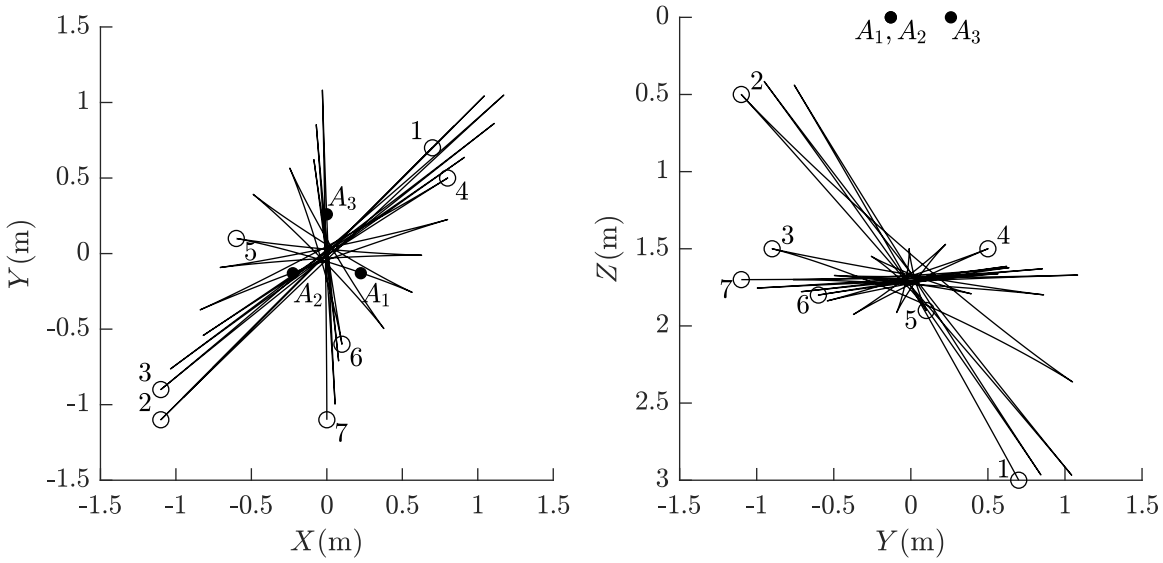

(a) Top view of the example trajectory.

(b) Front view of the example trajectory.

Figure 2.6 – Example trajectory.

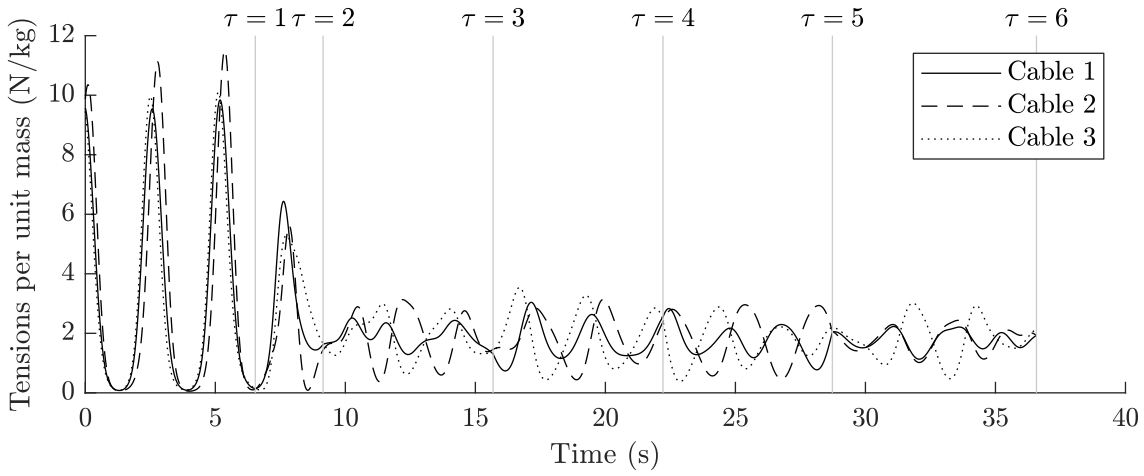

Figure 2.7 – Computed tensions along the trajectory.

by eq. (2.34) does not swap sign.) Figure 2.8 compares the tensions along this segment for these two numbers of arcs respectively. As it can be observed, the minimum tension reached along this segment is larger with 7 arcs than it is with 5 arcs, which enhances the dynamic stability of the end-effector. By virtue of the ideas developed in Section 2.8.1, augmenting the number of arcs of the hypocycloid by an even number is guaranteed to increase the minimum tension in the cables for any segment that satisfies eq. (2.55). In practice, this technique can therefore be used to avoid losing cable tension due to experimental and control error. A video showing this experimentation (*Chap2_3dofPointToPointTrajectory.mp4*) is available under [46] Pascal Dion-Gauvin at:

https://robot.gmc.ulaval.ca/publications/these-de-doctorat.

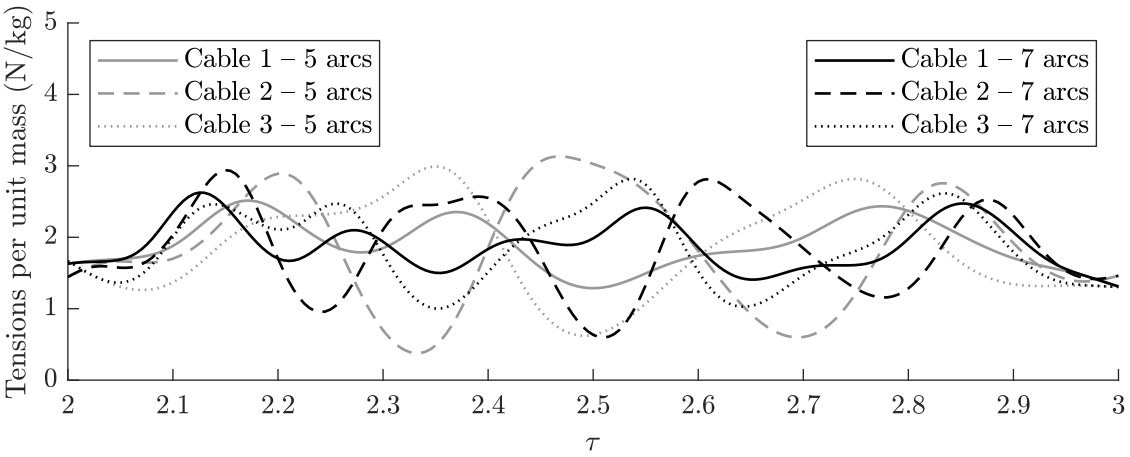

Figure 2.8 – Computed tensions along the third segment with 5 and 7 arcs respectively.

2.10 Conclusion

This paper proposes a point-to-point trajectory formulation for spatial three-dof cable-suspended mechanisms. The trajectory can be used in sequence to connect consecutive target points with zero instantaneous velocity that may lie beyond the static workspace of the mechanism. Moreover, the technique ensures continuity up to the acceleration level at the target points to avoid discontinuous cable forces. Compared to existing references, the proposed technique produces attainable regions of target points that are much larger. In particular, any horizontal trajectory is guaranteed to be feasible. The proposed trajectory path consists of a hypocycloidal curve that is located in the plane defined by the acceleration vector at the initial point and the final point. This curve is coupled to an amplitude function in order to connect target points that are located at different distances from point $\mathbf{p}_0$, defined on the vertical central axis. The trajectory parameters are designed such that the likelihood of generating a feasible trajectory increases with the number of arcs of the hypocycloid. An iterative procedure is thus provided to determine the minimum number of arcs allowing positive cable tensions for given initial and final points. In addition, a test derived from a sufficient but not necessary condition for trajectory feasibility is provided. This test demonstrates that target points located in the same horizontal plane can always be connected in sequence. Furthermore, it leads to a value for z_0 for which the proposed trajectory can successfully connect any sequence of target points. Because this value may not be usable in practice, other guidelines are provided to ensure a proper choice of z_0. Finally, the simulation results of an example trajectory are presented. This example trajectory was performed experimentally, which validates the approach. Broadly, the proposed approach appears to be well suited for any point-to-point trajectory whereby the acceleration at each target point is proportional to its distance from a unique point in space (e.g.: point $\mathbf{p}_0$ in the paper). Current work includes the dynamic point-to-point trajectory planning for six-dof cable-suspended parallel mechanisms.

2.11 Bibliography

J. Albus, R. Bostelman, and N. Dagalakis. The NIST Robocrane. *Journal of Robotic Systems*, 10(5):709–724, 1993. ISSN 07412223. doi:10.1002/rob.4620100509.

A. B. Alp and S. K. Agrawal. Cable suspended robots: Design, planning and control. In *Proceedings of the IEEE International Conference on Robotics and Automation*, volume 4, pages 4275–4280, Washington, DC, USA, 2002. doi:10.1109/ROBOT.2002.1014428.

G. Barrette and C. M. Gosselin. Determination of the dynamic workspace of cable-driven planar parallel mechanisms. *Journal of Mechanical Design, Transactions of the ASME*, 127 (2):242–248, 2005. ISSN 10500472. doi:10.1115/1.1830045.

S. Bouchard and C. Gosselin. A gravity-powered mechanism for extending the workspace of a cable-driven parallel mechanism: Application to the appearance modelling of objects. *International Journal of Automation Technology*, 4(4):372–379, 2010.

L. L. Cone. Skycam: An aerial robotic camera system. *Byte*, 10(10):122–132, 1985. ISSN 03605280.

D. Cunningham and H. H. Asada. The winch-bot: A cable-suspended, under-actuated robot utilizing parametric self-excitation. In *Proceedings of the 2009 IEEE International Conference on Robotics and Automation*, pages 1844–1850, 2009. doi:10.1109/ROBOT.2009.5152378.

P. Dion-Gauvin and C. Gosselin. Trajectory planning for the static to dynamic transition of point-mass cable-suspended parallel mechanisms. *Mechanism and Machine Theory*, 113: 158–178, 07 2017. doi:10.1016/j.mechmachtheory.2017.03.003.

C. Gosselin. Global planning of dynamically feasible trajectories for three-dof spatial cable-suspended parallel robots. In T. Bruckmann and A. Pott, editors, *Cable-Driven Parallel Robots*, pages 3–22. Springer Berlin Heidelberg, Berlin, Heidelberg, 2013. ISBN 978-3-642-31988-4. doi:10.1007/978-3-642-31988-4_1.

C. Gosselin and S. Foucault. Dynamic point-to-point trajectory planning of a two-dof cable-suspended parallel robot. *IEEE Transactions on Robotics*, 30(3):728 – 736, 2014. ISSN 1552-3098. doi:10.1109/TRO.2013.2292451.

C. Gosselin and A. Hadj-Messaoud. Automatic planning of smooth trajectories for pick-and-place operations. *Journal of Mechanical Design, Transactions of the ASME*, 115(3): 450–456, September 1993. doi:10.1115/1.2919211.

C. Gosselin, P. Ren, and S. Foucault. Dynamic trajectory planning of a two-dof cable-suspended parallel robot. In *Proceedings of the IEEE International Conference on Robotics and Automation*, pages 1476–1481, St. Paul, MN, USA, 2012. doi:10.1109/ICRA.2012.6224683.

M. Gouttefarde, S. Krut, F. Pierrot, and N. Ramdani. On the design of fully constrained parallel cable-driven robots. In *Advances in Robot Kinematics: Analysis and Design*, pages 71–78. Springer Netherlands, Dordrecht, 2008. ISBN 978-1-4020-8599-4. doi:10.1007/978-1-4020-8600-7_8.

X. Jiang and C. Gosselin. Dynamically feasible trajectories for three-dof planar cable-suspended parallel robots. In *Proceedings of the ASME Design Engineering Technical Conference*, volume 5A, Buffalo, NY, USA, 2014. doi:10.1115/DETC2014-34419. V05AT08A085.

X. Jiang and C. Gosselin. Trajectory generation for three-degree-of-freedom cable-suspended parallel robots based on analytical integration of the dynamic equations. *Journal of Mechanisms and Robotics*, 8(4), 2016a. ISSN 1942-4302. doi:10.1115/1.4031501.

X. Jiang and C. Gosselin. Dynamic point-to-point trajectory planning of a three-dof cable-suspended parallel robot. *IEEE Transactions on Robotics*, 32(6):1550–1557, Dec 2016b. ISSN 1552-3098. doi:10.1109/TRO.2016.2597315.

L. Kevac, M. Filipovic, and A. Rakic. The trajectory generation algorithm for the cable-suspended parallel robot—the cpr trajectory solver. *Robotics and Autonomous Systems*, 94:25–33, 2017. ISSN 0921-8890. doi:10.1016/j.robot.2017.04.018.

M. H. Korayem and H. Tourajizadeh. Maximum dlcc of spatial cable robot for a predefined trajectory within the workspace using closed loop optimal control approach. *Journal of Intelligent and Robotic Systems*, 63(1):75–99, jul 2011. ISSN 0921-0296. doi:10.1007/s10846-010-9521-9.

J. Lawrence. *A Catalog of Special Plane Curves*. Dover Books on Mathematics. Dover Publications, 1972. ISBN 9780486602882.

S. Lefrançois and C. Gosselin. Point-to-point motion control of a pendulum-like 3-dof underactuated cable-driven robot. In *Proceedings of the IEEE International Conference on Robotics and Automation*, pages 5187–5193, Anchorage, AK, USA, 2010. doi:10.1109/ROBOT.2010.5509656.

W. B. Lim, G. Yang, S. H. Yeo, S. K. Mustafa, and I. M. Chen. A generic tension-closure analysis method for fully-constrained cable-driven parallel manipulators. In *Proceedings of the IEEE International Conference on Robotics and Automation*, pages 2187–2192, May 2009. doi:10.1109/ROBOT.2009.5152772.

J. Pusey, A. Fattah, S. Agrawal, and E. Messina. Design and workspace analysis of a 6-6 cable-suspended parallel robot. *Mechanism and Machine Theory*, 39(7):761–778, 2004. ISSN 0094114X. doi:10.1016/j.mechmachtheory.2004.02.010.

A. T. Riechel and I. Ebert-Uphoff. Force-feasible workspace analysis for under-constrained, point-mass cable robots. In *Proceedings of the IEEE International Conference on Robotics and Automation*, volume 5, pages 4956–4962, April 2004. doi:10.1109/ROBOT.2004.1302503.

D. Zanotto, G. Rosati, and S. Agrawal. Modeling and control of a 3-dof pendulum-like manipulator. In *Proceedings of the IEEE International Conference on Robotics and Automation*, pages 3964–3969, Shanghai, China, 2011. doi:10.1109/ICRA.2011.5980198.

N. Zoso and C. Gosselin. Point-to-point motion planning of a parallel 3-dof underactuated cable-suspended robot. In *Proceedings of the IEEE International Conference on Robotics and Automation*, pages 2325–2330, St. Paul, MN, USA, 2012. doi:10.1109/ICRA.2012.6224598.

Chapitre 3

Beyond-the-static-workspace point-to-point trajectory planning of a 6-dof cable-suspended mechanism using oscillating SLERP

3.1 Résumé

Cet article présente un cadre général pour la planification de mouvements point à point s'étendant au-delà de l'espace de travail statique de mécanismes à câbles suspendus à 6 ddl. D'une part, la composante translationnelle du mouvement est basée sur une généralisation du mouvement hypocycloïdal introduit précédemment pour des mécanismes à cables suspendus à effecteur ponctuel à 3 ddl. D'autre part, la composante rotationnelle du mouvement repose sur l'interpolation linéaire sphérique, alors qu'une formulation novatrice est proposée afin de relier deux orientations complètement arbitraires par des oscillations angulaires passant par l'orientation de référence de l'effecteur. Pour les deux composantes du mouvement, la continuité de l'accélération est assurée aux poses cibles. Également, le concept d'états cinématiques idéaux est utilisé pour maximiser la probabilité de produire des trajectoires réalisables dynamiquement, soit des trajectoires induisant des forces exclusivement de tension dans les câbles. Il est montré que l'impact de la composante translationnelle du mouvement sur les contraintes de tension est dominant, comparativement à celui de la composante rotationnelle. Une procédure d'évaluation de la faisabilité de la trajectoire, qui inclut la vérification des interférences mécaniques et la détection des singularités, est aussi présentée. Finalement, un repère cylindrique décrivant de manière très intuitive la configuration du mécanisme est proposé, et des résultats de simulation sont présentés afin d'illustrer la pertinence de l'approche proposée.

3.2 Abstract

This paper presents a general framework for the planning of point-to-point motions that extend beyond the static workspace of 6-dof cable-suspended parallel mechanisms. The translational component of the motion is based on a generalization of the hypocycloidal motion previously introduced for 3-dof cable-suspended mechanisms. The rotational component of the trajectories uses spherical linear interpolation to connect two arbitrary orientations through oscillations going through the reference orientation. For both components of the motion, the continuity of the acceleration is ensured at the endpoints. Also, the concept of ideal kinematic state is used to maximize the chances of obtaining feasible trajectories, i.e., trajectories in which tension is maintained in the cables. It is shown that the impact of the translational trajectories on the tension constraints is largely dominant, compared to that of the rotational trajectories. A procedure for verifying the feasibility of the trajectory, which includes the detection of mechanical interferences and singularities, is provided. Finally, a natural cylindrical coordinate frame that yields a very intuitive description of the configuration of the mechanism is introduced and simulation results are given to illustrate the effectiveness of the proposed approach.

3.3 Introduction

Cable-suspended parallel robots (CSPRs) are a class of cable-driven parallel robots in which cable tension is generated by the gravitational force acting on the moving platform. Examples of application of CSPRs include the SkyCam (Cone, 1985), the NIST RoboCrane (Albus et al., 1993) and the FAST radio telescope (Zi et al., 2008). Most CSPRs are designed to be operated within their static workspace, namely the set of configurations in which the platform can be brought to rest with all cables in tension. Algorithms have been proposed for the trajectory planning and control of CSPRs in such a context (see for instance Barnett and Gosselin, 2015; Korayem and Bamdad, 2009). However, this approach limits the workspace of the platform to the footprint of the attachment points of the fixed winches.

In order to extend the capabilities and applications of CSPRs, researchers proposed the concept of dynamic workspace (Barrette and Gosselin, 2005), which includes all poses of the platform that can be reached with a controlled kinematic state (position, velocity, acceleration) while maintaining all cables in tension. Including kinematic states with non-zero acceleration drastically extends the workspace beyond the static workspace. This concept was first investigated for underactuated cable-suspended mechanisms. In Cunningham and Asada (2009), a basic model was developed and the necessity of using numerical integration was pointed out. In Lefrançois and Gosselin (2010), a 3-dof underactuated robot was developed and demonstrated experimentally. In Zanotto et al. (2011), some inconsistencies in the model proposed in Lefrançois and Gosselin (2010) were pointed out and a novel design was

introduced. In Zoso and Gosselin (2012), point-to-point motion planning was addressed and the concepts were generalized in Scalera et al. (2020) and Idà et al. (2019). Underactuated CSPRs yield complex control schemes requiring on-line numerical integration (Zanotto et al., 2011). In order to simplify the control, the concept was then applied to fully actuated CSPRs in Gosselin et al. (2012) and Gosselin (2013) where successful trajectories reaching target points beyond the static workspace were first demonstrated and mathematical techniques to globally assess the feasibility of trajectories were presented.

One of the challenges in the exploitation of the dynamic workspace of CSPRs is the design of trajectories that effectively reach prescribed poses of the platform while maintaining the cables in tension. Several techniques were proposed to design such trajectories for either periodic or point-to-point trajectories (see for instance Schmidt et al. (2014) and Zhang and Shang (2016) where ad hoc techniques are developed, Zhang et al. (2017) where a geometric approach is used, and Jiang et al. (2019) and Xiang et al. (2020b) where more standard numerical techniques are used).

In Mottola et al. (2019), such techniques were specifically developed for a purely translational CSPR based on parallelogram cable loops. In Mottola et al. (2018), elliptical trajectories were considered as a means of generalizing the trajectory planning. Also, in Xiang et al. (2021), trajectories going through singular orientations were treated and the application of the trajectory planning to throwing operations was addressed in Lin et al. (2020).

Among other proposed approaches, the analytical integration of the equations of motion was presented in Jiang and Gosselin (2016b,a), the use of natural frequencies was described in Jiang et al. (2018b,a) and the use of model predictive control was proposed in Xiang et al. (2020a).

In Dion-Gauvin and Gosselin (2017), the concepts of ideal kinematic states (pendulum constraint) and pseudo-tensions were introduced. These concepts provide great insight into the trajectory planning and provide tools for the development of globally effective approaches (Dion-Gauvin and Gosselin, 2017, 2018). Based on these results, the use of hypocycloidal trajectories was proposed in Dion-Gauvin and Gosselin (2018) for the trajectory planning of 3-dof CSPRs.

In this paper, the hypocycloidal trajectory proposed in Dion-Gauvin and Gosselin (2018) is generalized and a more flexible formulation is developed for the translational trajectories while remaining consistent with the pendulum constraint. In order to make the method applicable to 6-dof CSPRs, rotational trajectories are also handled. The proposed approach significantly extends the capabilities of existing methods: it can connect arbitrarily specified poses between which all six dofs are varied and controlled. Trajectory feasibility is ensured, including the detection of mechanical interferences and singularities and simulation results are provided to demonstrate the effectiveness of the proposed approach. Another important contribution of this paper is the definition of a cylindrical coordinate system that provides a very natural

means of computing and illustrating trajectories of CSPRs.

The paper is structured as follows. Section 3.4 recalls the kinematic and dynamic models, the architecture of 6-dof CSPRs and the ideal kinematic states. In Section 3.5, properties of quaternions and spherical linear interpolation are recalled. Sections 3.6 and 3.7 respectively present the proposed translational and rotational trajectories. Section 3.8 proposes relations on the trajectory endpoints to maximize the likelihood that the trajectory induces tensile-only forces in the cables. In Section 3.9, static-to-dynamic transition trajectories and the selection of the trajectory's starting and ending poses at rest in the static workspace are discussed. Section 3.10 deals with the workspace of cable-suspended mechanism while Section 3.11 discusses trajectory feasibility. Finally, Section 3.12 introduces the cylindrical coordinate system and presents simulation results to demonstrate the effectiveness of the proposed approach.

3.4 Introductory Concepts

3.4.1 Geometric Modelling

A general 6-dof cable-suspended parallel mechanism is represented schematically in Fig. 3.1. Six fixed actuated spools, whose cable outputs are represented by points $B_k,\ k = 1, ..., 6$ on the figure, are used to control the length of the cables, which are attached to a common platform at the attachment points $A_k,\ k = 1, ..., 6$. By adjusting the extension of the cables, the position and orientation of the platform can thus be controlled. The mechanism includes six actuators and six dofs and is therefore fully actuated. However, because of the unilaterality of the cable forces, the platform is not fully constrained and conditions must be imposed on the trajectory of the end-effector to ensure that it does not require compression forces in the cables.

Referring to Fig. 3.1, a fixed reference frame $OXYZ$ is defined on the base of the mechanism and a moving reference frame $PX'Y'Z'$ is attached to the centre of mass C_M of the platform. Without loss of generality, the origin of the fixed coordinate system is placed at the centroid of the cable spools [1] and the $Z-$axis is aligned with the direction of the gravity vector $\mathbf{g}$. In this reference frame, the position vector of point B_k is noted $\mathbf{b}_k$, while in the moving reference frame, the position vector of point A_k with respect to point P is noted $\mathbf{a}_k$. The position of the moving reference frame in the fixed reference frame—and thereby the position of the C_M of the platform in the fixed reference frame—is given by vector $\mathbf{p} = \begin{bmatrix} x & y & z \end{bmatrix}^T$, while the orientation of the moving reference frame with respect to the fixed reference frame—and thereby the orientation of the platform in the fixed reference frame—, is given by the rotation matrix $\mathbf{Q}$.

1. In the schematic representation of Fig. 3.1, the fixed frame is not located at the centroid of the spools, for better clarity of the figure, but all vectors are consistently defined.

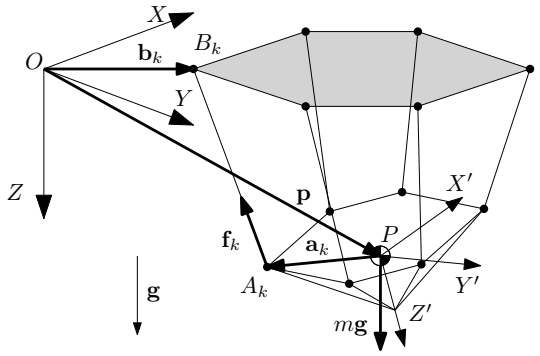

Figure 3.1 – Schematic representation of a general 6-dof cable-suspended parallel mechanism.

3.4.2 Kinematic and Dynamic Modelling

Vector $\boldsymbol{\rho}_k$ connecting point B_k to point A_k along the k-th cable can be written as

$$\boldsymbol{\rho}_k = \mathbf{p} + \mathbf{Q}\mathbf{a}_k - \mathbf{b}_k, \qquad k = 1, 2, ..., 6, \tag{3.1}$$

and hence the inverse kinematic model of the mechanism is given by:

$$\rho_k^2 = (\mathbf{p} + \mathbf{Q}\mathbf{a}_k - \mathbf{b}_k)^T(\mathbf{p} + \mathbf{Q}\mathbf{a}_k - \mathbf{b}_k), \qquad k = 1, 2, ..., 6, \tag{3.2}$$

where ρ_k stands for the magnitude of vector $\boldsymbol{\rho}_k$. Upon differentiating with respect to time and simplifying, one obtains

$$\rho_k\dot{\rho}_k = \boldsymbol{\rho}_k^T\dot{\mathbf{p}} + (\mathbf{Q}\mathbf{a}_k \times \boldsymbol{\rho}_k)^T\boldsymbol{\omega}, \qquad k = 1, 2, ..., 6, \tag{3.3}$$

where $\boldsymbol{\omega}$ stands for the angular velocity of the platform expressed in the fixed reference frame of the mechanism. Writing the above expressions in matrix form yields the velocity equation of the mechanism, namely

$$\mathbf{K}\dot{\boldsymbol{\rho}} = \mathbf{J}\mathbf{t}, \tag{3.4}$$

with

$$\mathbf{K} = \mathrm{diag}\left(\begin{bmatrix}\rho_1 & \rho_2 & \dots & \rho_6\end{bmatrix}\right) \qquad \text{and} \qquad \mathbf{J} = \begin{bmatrix}\boldsymbol{\rho}_1^T & (\mathbf{Q}\mathbf{a}_1 \times \boldsymbol{\rho}_1)^T \\ & \vdots \\ \boldsymbol{\rho}_6^T & (\mathbf{Q}\mathbf{a}_6 \times \boldsymbol{\rho}_6)^T\end{bmatrix}, \tag{3.5}$$

where $\mathbf{K}$ and $\mathbf{J}$ are the Jacobian matrices of the mechanism, $\dot{\boldsymbol{\rho}} = \begin{bmatrix}\dot{\rho}_1 & \dot{\rho}_2 & \dots & \dot{\rho}_6\end{bmatrix}^T$ is the vector of joint velocities and $\mathbf{t} = \begin{bmatrix}\dot{\mathbf{p}}^T & \boldsymbol{\omega}^T\end{bmatrix}^T$ is the vector of Cartesian velocities of the platform.

The dynamic model of the mechanism, obtained with the Newton-Euler equations of motion, can be written in the fixed reference frame of the mechanism as:

$$\sum_{k=1}^{6}\left(-f_k\frac{\boldsymbol{\rho}_k}{\rho_k}\right) + m\mathbf{g} = m\ddot{\mathbf{p}} \tag{3.6}$$

$$\sum_{k=1}^{6}\left(\mathbf{Q}\mathbf{a}_k \times \left(-f_k\frac{\boldsymbol{\rho}_k}{\rho_k}\right)\right) = \dot{\mathbf{h}}_G \tag{3.7}$$

with

$$\dot{\mathbf{h}}_G = \mathbf{Q}\mathbf{I}_G\mathbf{Q}^T\dot{\boldsymbol{\omega}} + \boldsymbol{\omega} \times \mathbf{Q}\mathbf{I}_G\mathbf{Q}^T\boldsymbol{\omega}. \tag{3.8}$$

In the above equations, f_k represents the tension in the k-th cable, m is the mass of the platform, and $\mathbf{I}_G$ is the inertia tensor of the platform with respect to the C_M of the platform and written in the reference frame attached to the platform. Referring to eq. (3.5) and defining $\boldsymbol{\tau} = \begin{bmatrix} f_1 & f_2 & \dots & f_6 \end{bmatrix}$ as the vector of joint (cable) forces, eqs. (3.6) and (3.7) can be simply written as

$$-\mathbf{J}^T\mathbf{K}^{-T}\boldsymbol{\tau} = m \begin{bmatrix} \ddot{\mathbf{p}} - \mathbf{g} \\ \frac{1}{m}\dot{\mathbf{h}}_G \end{bmatrix}, \tag{3.9}$$

where matrix $\mathbf{K}$ is invertible as long as none of the cable lengths goes to zero. Using the substitution

$$\boldsymbol{\mu} = \frac{1}{m}\mathbf{K}^{-T}\boldsymbol{\tau} = \begin{bmatrix} \frac{f_1}{m\rho_1} & \frac{f_2}{m\rho_2} & \dots & \frac{f_6}{m\rho_6} \end{bmatrix}^T, \tag{3.10}$$

the dynamic model of the platform finally becomes

$$-\mathbf{J}^T\boldsymbol{\mu} = \begin{bmatrix} \ddot{\mathbf{p}} - \mathbf{g} \\ \frac{1}{m}\dot{\mathbf{h}}_G \end{bmatrix}, \tag{3.11}$$

where vector $\boldsymbol{\mu}$ comprises the tensions in the cables per unit mass per unit cable length. For the sake of brevity however, this quantity is henceforth referred to simply as *cable tensions*, while tension forces measured in Newtons are referred to as *actual cable tensions*. Therefore, the positive tension constraints are obtained by inverting eq. (3.11) and by ensuring that

$$\boldsymbol{\mu} \succeq \mathbf{0}, \tag{3.12}$$

where $\succeq$ stands for the componentwise inequality. These constraints must be satisfied at all points of the trajectory for it to be feasible.

3.4.3 Architecture

In some other works on dynamic trajectory planning of cable-suspended mechanisms (Jiang et al., 2018b,a; Xiang et al., 2020b), the architecture (geometric arrangement) that is put forward is one that maximizes the static workspace of cable-suspended hexapods (Bouchard and Gosselin, 2010). However, standard architectures of 6-dof parallel mechanisms for which the base and the platform are coplanar, such as the TSSM architecture, the MSSM architecture (Merlet, 1988), or any architecture whose base and platform consist of semi-regular hexagons, should be preferred for dynamic trajectories. First of all, in order to maximize the static workspace, the architecture developed in Bouchard and Gosselin (2010) has its cables crisscrossing in between the platform and the base, thereby making the architecture more prone to interference between the cables when the platform is *outside* the static workspace. It is incidentally for this reason that Jiang et al. (2018b,a) and Xiang et al. (2020b) avoid planning trajectories that perform torsional motions. By contrast, standard architectures

of hexapods have their legs placed on the periphery of the space enclosed by the base and the platform, which circumscribes cable-intersecting poses to extreme configurations of the mechanism. Moreover, this arrangement of the legs effectively makes standard architectures articulated polyhedra, which offers the added advantage of yielding a reduced singularity locus since only non-convex configurations of polyhedra can be singular (Cauchy, 1813). Finally, the platform considered in Jiang et al. (2018b,a) and Xiang et al. (2020b) has its centre of mass, point C_M, positioned at a distance d below the centroid of the cable attachment points, noted C_A. Since point C_A is the estimated point of application of the resultant force applied by the cables, this geometry creates a lever arm between point C_A and point C_M that typically results in cable forces of similar magnitude exerting a moment of force with respect to the centre of mass of the platform. This is detrimental for dynamic trajectory planning since, conversely, applying a zero net moment of force to the platform so as to induce a purely translational motion can hardly be achieved, especially while ensuring tensile-only forces in the cables. Therefore, platforms with distinct centre of mass and centroid of the cable attachment points should be avoided when performing dynamic trajectories, and standard architectures of 6-dof parallel mechanisms with coinciding C_A and C_M should instead be preferred. In this paper, a cable-suspended mechanism satisfying these conditions with a horizontal base plane is assumed. Moreover, the reference orientation of the mechanism is defined as the orientation whereby the plane formed by the cable attachment points on the platform, is orthogonal to the direction of the gravity vector, and whereby the sum of the norms of the projection onto this horizontal plane of the unit vectors defined along each cable, is minimal. These cable attachment points thus all lie in the $X'Y'$ plane of the moving reference frame.

3.4.4 Ideal Kinematic States

For cable-suspended mechanisms, the kinematic states (pose, translational and angular velocity, acceleration) that are the least likely to yield a negative tension in one of the cables if an external disturbance were to occur can be considered as ideal and deserve special consideration. As pointed out in Dion-Gauvin and Gosselin (2017, 2018), end-effectors of cable mechanisms are as steady as the smallest tension relative to the others. Correspondingly, the locus of ideal kinematic states consists of the poses, velocities and accelerations that induce equal tensions in all cables. Therefore, substituting $\mu_k = \frac{\eta}{6}, k = 1, \ldots, 6$, into eq. (3.11) leads to the general expression

$$-\begin{bmatrix} \mathbf{p} + \mathbf{Q}\mathbf{c}_A - \mathbf{c}_B \\ \mathbf{Q}\mathbf{c}_A \times \mathbf{p} - \frac{1}{6}\sum\left(\mathbf{Q}\mathbf{a}_k \times \mathbf{b}_k\right) \end{bmatrix} \eta = \begin{bmatrix} \ddot{\mathbf{p}} - \mathbf{g} \\ \frac{1}{m}\dot{\mathbf{h}}_G \end{bmatrix}, \tag{3.13}$$

where $\mathbf{c}_B$ is the position vector of the centroid of the cable spools on the base expressed in the fixed reference frame and $\mathbf{c}_A$ is the position vector of the C_A of the platform with respect to its C_M expressed in the moving reference frame. Referring to the model presented in Section 3.4.1 and the assumptions made in Section 3.4.3, the fixed reference frame has its

origin placed at the centroid of the cable spools $\mathbf{c}_B = \mathbf{0}$ and the C_A of the platform coincides with its C_M $\mathbf{c}_A = \mathbf{0}$, thus simplifying the above expression into

$$\eta \begin{bmatrix} -\mathbf{p} \\ \mathbf{m} \end{bmatrix} = \begin{bmatrix} \ddot{\mathbf{p}} - \mathbf{g} \\ \frac{1}{m}\dot{\mathbf{h}}_G \end{bmatrix}, \tag{3.14}$$

with

$$\mathbf{m} = \tfrac{1}{6} \sum (\mathbf{Q}\mathbf{a}_k \times \mathbf{b}_k). \tag{3.15}$$

Eqs. (3.13) and (3.14) represent respectively a general and a simplified version of the ideal kinematic states relation for parallel cable-suspended mechanisms. They yield, for a given pose of the platform, the angular velocity and angular and translational accelerations of the end-effector that correspond to the state in which the cables are the least likely to have negative tension. These expressions reveal that, to allow end-effectors to be as dynamically stable as possible, the gravito-inertial vector appearing in the right-hand side of eqs. (3.13) and (3.14) must be parallel to the vector on the left-hand side of eqs. (3.13) and (3.14). This relation is restrictive, since it makes the rotational motion of the end-effector depend on its inertia matrix and on the architectural parameters $\mathbf{a}_k$ and $\mathbf{b}_k$ of the mechanism. For this reason, if at all possible, it would be very challenging to develop an analytical rotational trajectory formulation that complies with eq. (3.14). Nevertheless, this principle remains of great relevance by its very nature and in that respect, it is exploited in Section 3.8 to ensure that trajectory endpoints are located as far as possible from the zero-tension locus. Hence, the notion of ideal kinematic states should be kept in mind when working with cable mechanisms.

3.5 Properties of Quaternions

As one of the mathematical formalisms used to represent rotations in three dimensions, quaternions are particularly effective for handling general three-dimensional rotational motion. Thanks to their vector notation, quaternions allow for simple and powerful interpolation methods that are independent from the choice of coordinate system. Moreover, unlike Euler angles, quaternions are not subject to gimbal lock, which is a loss of dof occurring when two of the three Euler angles become dependent. Also, the correspondence between an orientation and the quaternion to be used in a quaternion-based trajectory can easily be established, whereas there is no clear basis for determining which of the two Euler angle triples corresponding to a given endpoint orientation should be used in a rotational trajectory formulation for the resulting motion to be feasible. In the following, the relations and properties of quaternions that are used in Section 3.7 to devise the rotational trajectory are recalled.

3.5.1 General Properties

Quaternions can be viewed as a four-dimensional extension of complex numbers comprising a scalar real part and a three-dimensional imaginary part that is written as

$$\mathbf{q} = q_0 + q_1\, i + q_2\, j + q_3\, k. \tag{3.16}$$

Alternatively, to allow matrix algebra operations, quaternions are also often given in vector form as

$$\mathbf{q} = \begin{bmatrix} q_0 \\ \mathbf{q}_v \end{bmatrix}, \tag{3.17}$$

where q_0 and $\mathbf{q}_v = \begin{bmatrix} q_1 & q_2 & q_3 \end{bmatrix}^T$ are the scalar and vector parts of the quaternion, respectively. While quaternion addition and substraction are performed componentwise, quaternion multiplication, noted with $\circ$, is defined as

$$\mathbf{q} \circ \mathbf{q}' = \begin{bmatrix} q_0 q_0' - {\mathbf{q}_v}^T \mathbf{q}_v' \\ q_0 \mathbf{q}_v' + q_0' \mathbf{q}_v + \mathbf{q}_v \times \mathbf{q}_v' \end{bmatrix} \tag{3.18}$$

which, due to its vector product, is non-commutative. The multiplicative identity of this number system, denoted in this paper by $\mathbf{q}_0$ and having the property $\mathbf{q}_0 \circ \mathbf{q} = \mathbf{q} \circ \mathbf{q}_0 = \mathbf{q}$, is

$$\mathbf{q}_0 = \begin{bmatrix} 1 \\ 0 \\ 0 \\ 0 \end{bmatrix} \tag{3.19}$$

or, expressed in a more intuitive way,

$$\mathbf{q}_0 = 1 + 0\, i + 0\, j + 0\, k = 1. \tag{3.20}$$

In terms of $\mathbf{q}_0$, the scalar part of a general quaternion $\mathbf{q}$ is thus given by

$$q_0 = \mathbf{q}_0^T \mathbf{q}, \tag{3.21}$$

while its vector part can be expressed as the matrix product

$$\mathbf{q}_v = \mathbf{T}\mathbf{q}, \tag{3.22}$$

where $\mathbf{T}$ is the 3×4 matrix extracting the last three components of a four-dimensional vector, namely:

$$\mathbf{T} = \begin{bmatrix} \mathbf{0}_3 & \mathbf{1}_{3\times 3} \end{bmatrix}. \tag{3.23}$$

Analogously to complex numbers, the conjugate of a quaternion $\mathbf{q} = \begin{bmatrix} q_0 & {\mathbf{q}_v}^T \end{bmatrix}^T$, noted $\mathbf{q}^*$, is defined as

$$\mathbf{q}^* = \begin{bmatrix} q_0 \\ -\mathbf{q}_v \end{bmatrix}, \tag{3.24}$$

which can be expressed in terms of $\mathbf{q}_0$ as

$$\mathbf{q}^* = -\mathbf{q} + 2q_0\mathbf{q}_0 = -\mathbf{q} + 2(\mathbf{q}_0^T\mathbf{q})\mathbf{q}_0 = (2\mathbf{q}_0\mathbf{q}_0^T - \mathbf{1})\mathbf{q}. \tag{3.25}$$

Finally, defining the norm of a quaternion as

$$\|\mathbf{q}\| = \sqrt{\mathbf{q}^* \circ \mathbf{q}} = \sqrt{\mathbf{q} \circ \mathbf{q}^*} = \sqrt{{q_0}^2 + \mathbf{q}_v^T\mathbf{q}_v}, \tag{3.26}$$

the inverse of a quaternion $\mathbf{q}$, denoted $\mathbf{q}^{-1}$ and having the property $\mathbf{q} \circ \mathbf{q}^{-1} = \mathbf{q}^{-1} \circ \mathbf{q} = \mathbf{q}_0$, is

$$\mathbf{q}^{-1} = \frac{\mathbf{q}^*}{\|\mathbf{q}\|^2}, \tag{3.27}$$

and hence the inverse of a unit quaternion is also its conjugate. By virtue of eq. (3.25), the inverse of a unit quaternion can therefore also be written in terms of $\mathbf{q}_0$ as

$$\mathbf{q}^{-1} = \mathbf{q}^* = (2\mathbf{q}_0\mathbf{q}_0^T - \mathbf{1})\mathbf{q} \qquad \text{for } \|\mathbf{q}\| = 1. \tag{3.28}$$

This expression is used in the formulation of the rotational trajectory.

3.5.2 Quaternion as a Representation of the Orientation

Let a rotation be described by a unit vector $\mathbf{e}$ representing the axis of rotation and a scalar γ representing the angle of rotation, whose matrix representation is the well-known expression

$$\mathbf{Q} = \mathbf{e}\mathbf{e}^T + (\mathbf{1} - \mathbf{e}\mathbf{e}^T)\cos(\gamma) + \mathbf{E}\sin(\gamma), \tag{3.29}$$

with $\mathbf{E}$ denoting the cross-product matrix of vector $\mathbf{e}$. The quaternion operator performing this rotation on a position vector $\mathbf{p}$ in $\mathbb{R}^3$ is

$$\begin{bmatrix} 0 \\ \mathbf{p}' \end{bmatrix} = \mathbf{q} \circ \begin{bmatrix} 0 \\ \mathbf{p} \end{bmatrix} \circ \mathbf{q}^{-1}, \tag{3.30}$$

where $\mathbf{p}'$ is the resulting rotated vector and where $\mathbf{q}$ is the unit quaternion

$$\mathbf{q} = \begin{bmatrix} \cos(\gamma/2) \\ \mathbf{e}\sin(\gamma/2) \end{bmatrix}. \tag{3.31}$$

The expression given in eq. (3.31) is the quaternion representation of a rotation. In this paper, it is used to describe the orientation of the platform by encapsulating the rotation of the moving reference frame with respect to the fixed reference frame of the mechanism. While any multiple of eq. (3.31) represents the same rotation and would yield the correct rotated vector in eq. (3.30), in practice only unit quaternions are employed. Hence in $\mathbb{R}^4$, the set of quaternions used to represent 3D orientations forms the surface of the four-dimensional unit sphere. Also, as it can be seen from the definition (3.31), the identity quaternion $\mathbf{q_0}$ unsurprisingly corresponds to the null rotation (reference orientation), while the inverse quaternion

$\mathbf{q}^{-1}$ describes the opposite orientation from that encoded by the quaternion $\mathbf{q}$, as it represents the rotation relative to the same axis of rotation $\mathbf{e}$ but by the opposite angle, $-\gamma$. Finally, it can be observed from the definition (3.31) and the rotation operator (3.30) that the quaternion $\mathbf{q}$ and its negative $-\mathbf{q}$ both describe the same orientation, and hence the quaternion to be used in a quaternion-based trajectory must imperatively be specified.

Let the quaternion $\mathbf{q}$ given by eq. (3.31) be varying over time, so as to denote the orientational motion of a rotating object, represented by its body frame, relative to a fixed reference frame. The angular velocity of the moving reference frame, obtained by differentiating eq. (3.30) with respect to time, is given in the fixed reference frame by (Graf, 2008)

$$\boldsymbol{\omega} = 2\mathbf{T}(\dot{\mathbf{q}} \circ \mathbf{q}^{-1}). \tag{3.32}$$

Likewise, differentiating the above relation with respect to time yields the expression for the angular acceleration of the moving reference frame expressed in the fixed reference frame, namely

$$\dot{\boldsymbol{\omega}} = 2\mathbf{T}(\ddot{\mathbf{q}} \circ \mathbf{q}^{-1}), \tag{3.33}$$

since it can be shown that $2\mathbf{T}(\dot{\mathbf{q}} \circ \dot{\mathbf{q}}^{-1}) = \mathbf{0}$.

3.5.3 Spherical Linear Interpolation

Spherical linear interpolation (SLERP) is an interpolation technique devised to connect two orientations expressed as quaternions. It links any two orientations through the straightest and shortest possible path (Dam et al., 1998). To the best of our knowledge, it is the only interpolation method having this property, which is why quaternions are adopted here to represent the orientation of the platform. Let quaternions $\mathbf{q}_O$ and $\mathbf{q}_{O'}$ denote the two end orientations to be connected, and let $\alpha(\tau)$ be a time function monotically increasing between 0 and 1 on the interval $\tau \in [0, 1]$. The SLERP joining $\mathbf{q}_O$ to $\mathbf{q}_{O'}$ can be written as (Shoemake, 1985)

$$\mathbf{q}(\tau) = \mathbf{q}_O \frac{\sin\left(\Psi(1-\alpha(\tau))\right)}{\sin(\Psi)} + \mathbf{q}_{O'} \frac{\sin\left(\Psi\alpha(\tau)\right)}{\sin(\Psi)} \qquad 0 \leq \alpha(\tau) \leq 1 \tag{3.34}$$

with

$$\Psi = \arccos({\mathbf{q}_O}^T \mathbf{q}_{O'}). \tag{3.35}$$

The above equation is the expression for SLERP that is put forward in this paper. It differs from the formulation usually seen in the literature in that the standard time parameter τ is replaced by the generic time function $\alpha(\tau)$ so as to allow the interpolated curve to satisfy the desired position, velocity and acceleration constraints (Jiang et al., 2018a). On the unit quaternion sphere, SLERP forms a great circle arc between the two end quaternions, and thereby follows the straightest and shortest path between two points on a sphere (Dam et al., 1998). For this shortest path between unit quaternions to also correspond to the shortest path between the two end orientations, it suffices that, of the two opposite quaternions $\mathbf{q}$ and $-\mathbf{q}$

that represent either end orientation, the pair chosen to appear in eq. (3.34) is one forming an acute angle, i.e., one satisfying ${\mathbf{q}_O}^T\mathbf{q}_{O'} > 0$. The motion thus obtained consists of a fixed-axis rotation of minimal angular amplitude between the two end orientations which is performed, if the conventional time function $\alpha(\tau) = \tau$ is used, with a constant angular velocity.

The formulation presented in eq. (3.34) can be used to generate a path that extends beyond the quaternions $\mathbf{q}_O$ and $\mathbf{q}_{O'}$ by not restricting the output range of the time function $\alpha(\tau)$ to the interval $[0, 1]$. For instance, the SLERP given by

$$\mathbf{q}(\tau) = \mathbf{q}_0 \frac{\sin\left(\Psi(1-\beta(\tau))\right)}{\sin(\Psi)} + \mathbf{q}_O \frac{\sin\left(\Psi\beta(\tau)\right)}{\sin(\Psi)} \qquad -1 \leq \beta(\tau) \leq 1 \tag{3.36}$$

with

$$\Psi = \arccos({\mathbf{q}_0}^T\mathbf{q}_O), \tag{3.37}$$

where $\mathbf{q}_0 = \begin{bmatrix} 1 & \mathbf{0}^T \end{bmatrix}^T$ is the reference orientation and where $\beta(\tau)$ is a continuous time function whose output covers the interval $[-1, 1]$, yields an interpolation curve connecting $\mathbf{q}_O$ to ${\mathbf{q}_O}^{-1}$ through $\mathbf{q}_0$. Indeed, substituting $\beta(\tau) = -1$ into eq. (3.36) leads to

$$\mathbf{q} = (2\mathbf{q}_0\mathbf{q}_0^T - \mathbf{1})\mathbf{q}_O, \tag{3.38}$$

which corresponds to the opposite orientation of $\mathbf{q}_O$ by virtue of eq. (3.28). This extended version of SLERP is used in Section 3.7 in the rotational trajectory formulation of the platform.

3.6 Translational Trajectory

The translational motion connects the prescribed initial point of the trajectory to the prescribed final point with zero instantaneous velocity at both endpoints. It also ensures the continuity of the acceleration at these endpoints to avoid discontinuous cable forces with the preceding and following trajectory segments. As demonstrated in Dion-Gauvin and Gosselin (2018) for point-mass end-effectors, a translational trajectory based on a hypocycloid curve is perfectly suited for connecting different target positions in 3D space since matching the initial and final cusps of the hypocycloid to the trajectory endpoints readily satisfies the zero velocity constraints. The trajectory developed in the above reference, however, fails to produce cusps of zero velocity *between* the arcs of the hypocycloid when connecting endpoints located at different distances from the centre of the curve. In addition, it imparts to each arc of the curve a travelling time that depends on its length, which is not consistent with the motion of a simple pendulum whose natural frequency, as it may be recalled, does not depend on the amplitude of the oscillation. In this paper, an upgraded version of the trajectory based on the (standard) hypocycloid presented in Dion-Gauvin and Gosselin (2018) is proposed. This newly developed hypocycloid of variable amplitude allows intermediate zero-velocity cusps to be generated when endpoints located at different distances from the centre of the curve are

to be connected. These cusps occurring at regular time intervals, the hypocyloid of variable amplitude also allows the travelling time along each arc to remain constant along the curve and independent from arc length. It is consequently observed empirically that the low cable tensions generated by the hypocycloid derived in this paper are of higher magnitude than those produced by the trajectory proposed in Dion-Gauvin and Gosselin (2018), which is the intended objective. In the next section, the plane in which the hypocycloid-based trajectory is embedded is defined. Then, the translational trajectory is established.

3.6.1 Plane of the Trajectory

Let $\mathbf{p}_1$ and $\mathbf{p}_2$ be the position vector of the initial point P_1 and final point P_2 of the trajectory, respectively. Also, let $\ddot{\mathbf{p}}_1$ be the initial acceleration vector, which must correspond to the final acceleration of the preceding trajectory segment in order to ensure continuity in the cable forces. As it can be observed from Fig. 3.2, the trajectory plane can be defined as the plane that contains both the acceleration vector at the initial point (defining a line), and the final point (defining a point). The acceleration vector at the final point $\ddot{\mathbf{p}}_2$, albeit undetermined yet, also lies in the trajectory plane. As a result, the two acceleration vectors necessarily meet at some point P_0 of the plane. Considering that these vectors must both be pointing toward the footprint of the base for tensile-only forces to be present in the cables, it is imposed—as is done in Dion-Gauvin and Gosselin (2018)—that they intersect on the central vertical axis of the static workspace of the mechanism, which passes through the centroid of the cable spools. Denoting the position vector of point P_0 as $\mathbf{p}_0 = \begin{bmatrix} 0 & 0 & z_0 \end{bmatrix}^T$, the initial and final acceleration vectors can be written as

$$\ddot{\mathbf{p}}_j = -\lambda_j(\mathbf{p}_j - \mathbf{p}_0), \qquad j = 1, 2, \tag{3.39}$$

where the known parameter λ_1 and the undetermined parameter λ_2 are positive definite. Hence the trajectory plane can alternatively be described as the plane containing points P_1, P_2, and P_0. The value of z_0 is determined in the implementation phase of trajectory planning as a function of the target points to ensure that the resulting translational motion remains entirely below the plane of the cable spools.

A planar fixed reference frame is defined on the trajectory plane, whose origin is chosen to be at point P_0 and whose X_h axis points in the direction of the initial point. The Y_h axis of this reference frame is located in the half of the trajectory plane that contains the final point (and is orthogonal to the X_h axis). The trajectory plane is thus spanned by vectors $(\mathbf{p}_1 - \mathbf{p}_0)$ and $(\mathbf{p}_2 - \mathbf{p}_0)$, which can be expressed by matrix $\mathbf{A}$ as

$$\mathbf{A} = \begin{bmatrix} (\mathbf{p}_1 - \mathbf{p}_0) & (\mathbf{p}_2 - \mathbf{p}_0) \end{bmatrix}. \tag{3.40}$$

Hence the matrix that maps the XY plane of the mechanism reference frame onto the trajectory reference frame, denoted $\mathbf{Q}_h$, is composed of the first two columns of the orthogonal

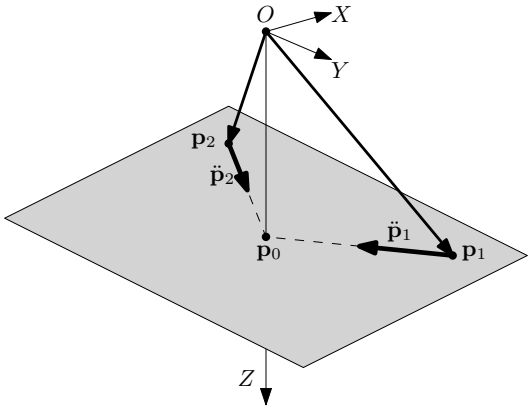

Figure 3.2 – Plane of the trajectory.

matrix obtained in the QR decomposition of $\mathbf{A}$. By virtue of the Gram-Schmidt process, this matrix is given by:

$$\mathbf{Q}_h = \begin{bmatrix} \mathbf{q}_{h1} & \mathbf{q}_{h2} \end{bmatrix}, \tag{3.41}$$

with

$$\mathbf{q}_{h1} = \frac{\mathbf{p}_1 - \mathbf{p}_0}{\|\mathbf{p}_1 - \mathbf{p}_0\|} \qquad \mathbf{q}_{h2} = \frac{(\mathbf{1} - \mathbf{q}_{h1}\mathbf{q}_{h1}^T)(\mathbf{p}_2 - \mathbf{p}_0)}{\|(\mathbf{1} - \mathbf{q}_{h1}\mathbf{q}_{h1}^T)(\mathbf{p}_2 - \mathbf{p}_0)\|}. \tag{3.42}$$

Hence, let $\mathbf{c} \in \mathbb{R}^2$ be a vector written in the trajectory reference frame and let $\mathbf{p} \in \mathbb{R}^3$ be the same vector written in the mechanism reference frame, one has:

$$\mathbf{p} = \mathbf{Q}_h \mathbf{c} + \mathbf{p}_0. \tag{3.43}$$

This relation is used in the following to write the parametric trajectory in the mechanism reference frame.

3.6.2 Hypocycloid Trajectory

In the trajectory plane, the general parametric equations of the hypocycloid of variable amplitude, whose complete derivation is provided in the Appendix (Section 3.14), can be written for a curve centred at point P_0 as

$$\mathbf{c}(t) = \frac{1}{n_h \theta_h} \begin{bmatrix} r(\tau)\theta_h \left((n_h - 1)\cos(\theta_h \tau) + \cos((n_h - 1)\theta_h \tau) \right) \\ r(\tau)\theta_h \left((n_h - 1)\sin(\theta_h \tau) - \sin((n_h - 1)\theta_h \tau) \right) \\ \qquad - r'(\tau)\left(\sin(\theta_h \tau) + \sin((n_h - 1)\theta_h \tau) \right) \\ \qquad + r'(\tau)\left(\cos(\theta_h \tau) - \cos((n_h - 1)\theta_h \tau) \right) \end{bmatrix}, \tag{3.44}$$

with

$$\tau = \frac{t}{T}, \tag{3.45}$$

where t is the time, T is the duration of the trajectory, $\tau \in [0, 1]$ is the normalized parametric coordinate, and $r(\tau)$ is the normalized expression of the spiral-like envelope of the curve. In

addition, angle θ_h that appears in eq. (3.44) is the plotting range of the curve while parameter $n_h \geq 2$ corresponds to the number of arcs (cusps) that the curve traces (reaches) over one lap before closing in on itself. Figure 3.3 illustrates the hypocycloid curve of variable amplitude and its spiral-like envelope for $\theta_h = -\frac{4\pi}{3}$, $n_h = 3$, $r(0) = 1$, and $r(1) = 1.5$. As it can be observed from the figure, it is the spiral-like nature of the envelope of the hypocycloid that enables points located at different distances from the origin to be connected. This spiral-like envelope also allows the velocity and acceleration boundary constraints to be satisfied.

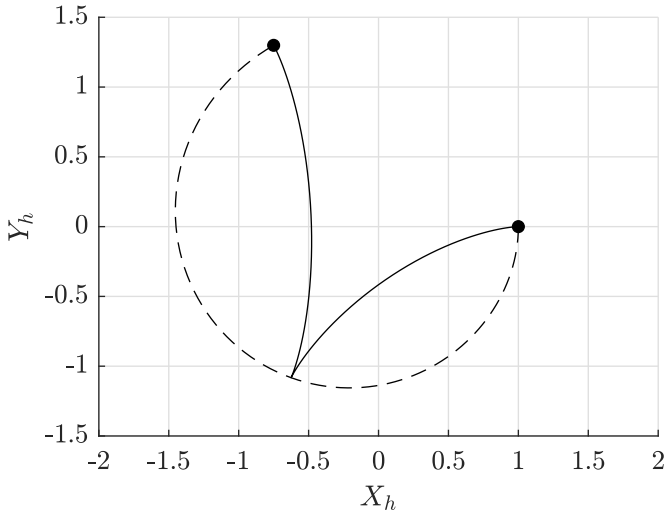

Figure 3.3 – Hypocycloid curve for $\theta_h = -\frac{4\pi}{3}$ and $n_h = 3$. The curve has 2 arcs over $^2/_3$ laps, yielding $n_h = 3$.

Defining r_1 and r_2 as

$$r_1 = \|\mathbf{p}_1 - \mathbf{p}_0\|, \qquad r_2 = \|\mathbf{p}_2 - \mathbf{p}_0\|, \tag{3.46}$$

the boundary conditions of the translational motion can be written in the trajectory reference frame as

$$\mathbf{c}(0) = \begin{bmatrix} r_1 \\ 0 \end{bmatrix}, \qquad \dot{\mathbf{c}}(0) = \mathbf{0}, \qquad \ddot{\mathbf{c}}(0) = -\lambda_1 \mathbf{c}(0), \tag{3.47}$$

and

$$\mathbf{c}(T) = \begin{bmatrix} r_2 \cos(\theta_h) \\ r_2 \sin(\theta_h) \end{bmatrix}, \qquad \dot{\mathbf{c}}(T) = \mathbf{0}, \qquad \ddot{\mathbf{c}}(T) = -\lambda_2 \mathbf{c}(T), \tag{3.48}$$

where the acceleration constraints of eqs. (3.47)–(3.48) are obtained using eq. (3.39) along with eq. (3.43). Substituting eqs. (3.47)–(3.48) into eq. (3.44) and its first two time derivatives leads to conditions on the spiral-like envelope of the hypocycloid, namely

$$r(0) = r_1, \qquad r(1) = r_2, \qquad r'(0) = r'(1) = r''(0) = r''(1) = 0, \tag{3.49}$$

as well as an expression for λ_1 and λ_2, given by

$$\lambda_1 = \lambda_2 = \frac{\theta_h^2(n_h - 1)}{T^2} = \lambda. \tag{3.50}$$

Considering eq. (3.49), the amplitude function $r(\tau)$ can be rewritten as

$$r(\tau) = (r_2 - r_1)A(\tau) + r_1, \tag{3.51}$$

where $A(\tau)$ is any normalized amplitude function that satisfies the boundary conditions

$$A(0) = 0, \qquad A(1) = 1, \qquad A'(0) = A'(1) = A''(0) = A''(1) = 0, \tag{3.52}$$

such as

$$A(\tau) = 6\tau^5 - 15\tau^4 + 10\tau^3, \tag{3.53}$$

which is the polynomial function of minimal degree that satisfies eq. (3.52). This amplitude function is used in the example trajectory of Section 3.12.

The spiral-like envelope of the hypocycloid being set, the initial and final points of the trajectory can be connected as illustrated in Fig. 3.4 through an arbitrary number of arcs $p \in \mathbb{N}^+$ by matching two of the hypocycloid cusps to the trajectory endpoints. Angle θ_h and parameter n_h being governed by the number of arcs of the hypocycloid, they can be written as (Dion-Gauvin and Gosselin, 2018)

$$\theta_h = \psi_h + (-1)^{p-1} 2\pi \left\lceil \frac{p-1}{2} \right\rceil \qquad p = 1, 2, 3, ..., \tag{3.54}$$

and

$$n_h = \frac{2\pi p}{|\theta_h|} \qquad p = 1, 2, 3, ..., \tag{3.55}$$

where angle ψ_h in eq. (3.54) is the smallest angle formed by vectors $(\mathbf{p}_1 - \mathbf{p}_0)$ and $(\mathbf{p}_2 - \mathbf{p}_0)$, namely

$$\psi_h = \arccos\left(\frac{(\mathbf{p}_1 - \mathbf{p}_0)^T (\mathbf{p}_2 - \mathbf{p}_0)}{\|(\mathbf{p}_1 - \mathbf{p}_0)\| \, \|(\mathbf{p}_2 - \mathbf{p}_0)\|} \right). \tag{3.56}$$

As it can be observed from Fig. 3.4, the advantage of devising a translational trajectory based on the number of arcs p is that as this parameter is increased, each arc of the hypocycloid curve tends to become rectilinear and to run parallel to the acceleration vector at its cusp, which in turn increases the likelihood that the trajectory induces positive tensions in the cables. In that respect, it is demonstrated in Dion-Gauvin and Gosselin (2018) that for a point-mass end-effector following a hypocycloidal path, a number of arcs p yielding positive tensions in the cables can always be found provided that the outer circle of the standard hypocycloid is completely located below the spools. This condition can be cast for the hypocycloid of variable amplitude of this paper as

$$1 - \max(r_1, r_2) \frac{\sqrt{{q_{h31}}^2 + {q_{h32}}^2}}{z_0} > 0, \tag{3.57}$$

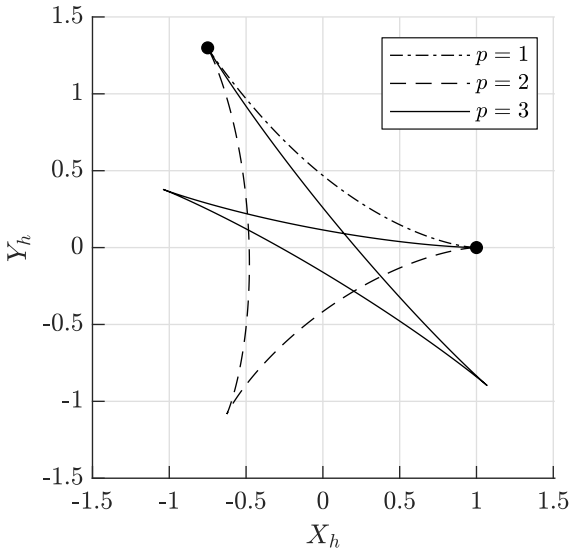

Figure 3.4 – Hypocycloid curve connecting two points having $\psi_h = \frac{2\pi}{3}$ with one, two, and three arcs respectively.

where z_0 is the Z-coordinate of point P_0, and where q_{h31} and q_{h32} are the corresponding components of matrix $\mathbf{Q}_h$. In particular, the above condition is always met for horizontal trajectories in which the initial and final points as well as the initial acceleration vector are located in the same horizontal plane. Hence it can be asserted that the translational component of the proposed trajectory never produces horizontal motions that would yield negative tensions in the cables.

It should be pointed out that this is an important advantage of the trajectory defined in eq. (3.44). In particular, previously proposed formulations cannot guarantee such feasibility and generally fail for demanding horizontal trajectories. For example, the approach devised in Jiang et al. (2018a) can only connect endpoints that are located at about the same distance from the central vertical axis—that is, having $r_1 \approx r_2$—and that form an angle ψ_h of about π radians. Hence, the technique proposed here presents substantial improvements over existing formulations.

3.7 Rotational Trajectory

The rotational trajectory yields the orientation of the platform at each instant of the motion. It connects the prescribed orientation of the platform at the initial point of the trajectory to the prescribed orientation at the final point with zero instantaneous angular velocity at both endpoints. It must also ensure the continuity of the angular acceleration at both endpoints to avoid undesirable discontinuous cable forces between trajectory segments. In addition, the rotational trajectory being performed while the platform undergoes the motion devised in the preceding section, its formulation must be based on the hypocycloidal curve since the

orientations it prescribes are enforced at the positions visited by the translational motion. In this context, one could conjecture that a likely feasible rotational motion for the platform is one in which it oscillates between opposite orientations along the arcs of the hypocycloidal trajectory. On any given arc, this motion reduces to connecting the orientation given at the first cusp to its opposite at the following cusp. The configuration at the beginning of the arc is assumed to be attainable since it has been reached by the preceding trajectory segment, while the configuration at the end of the arc is considered to be attainable since it is the exact symmetric counterpart of the configuration at the beginning of the arc. Moreover, these two orientations can be connected by a fixed-axis rotation (see Section 3.5.3) passing through the reference orientation. Hence, by replicating this rotation along each arc, a motion in which the platform alternates between opposite orientations at each cusp in sync with the oscillations of the hypocycloidal trajectory, is obtained. This proposition going hand-in-hand with the hypocycloidal nature of the translational trajectory, all that remains is to ensure that the kinematic constraints are satisfied at the endpoints. This can be accomplished by allowing the orientation at the cusps to slowly vary so as to match the initial and final boundary constraints at the first and last cusp of the hypocycloid, respectively.

It should be noted at this point that, since the orientation at the cusps is not kept constant throughout the motion to satisfy the boundary constraints, the orientation reached at the end of each arc does not quite correspond to the opposite of the orientation existing at the beginning of these arcs. This gap between the orientation at one cusp and its opposite at the following cusp however gets reduced as the number of arcs increases, since the increase in the number of arcs allows the difference between the prescribed initial and final orientations of the trajectory to be divided into a larger number of intermediate cusp orientations. As a result, increasing the number of arcs of the trajectory can be used as a strategy to increase the likelihood that the resulting motion be feasible. The design of the rotational motion is therefore consistent with that of its translational counterpart since, as it can be recalled, increasing the number of arcs also increases the likelihood that the trajectory be feasible (since it causes each arc of the hypocycloid to tend to become rectilinear and to run parallel to the acceleration vector at its cusp).

The proposed rotational motion is represented schematically in Fig. 3.5 for odd and even numbers of arcs. Quaternions $\mathbf{q}_1$ and $\mathbf{q}_2$ as defined in eq. (3.31) denote respectively the prescribed initial and final orientations of the platform in the fixed reference frame with, for the rotational oscillations to be of minimal angular amplitude, $\gamma_1, \gamma_2 \in [-\pi, \pi]$. As depicted in the figure, the rotational motion of the platform $\mathbf{q}(\tau)$ has its oscillations bounded by the curves passing by the orientation at the cusps, which thus constitute the envelopes of the oscillating trajectory. Accordingly, they are denoted $\mathbf{q}_{env}(\tau)$ and $\mathbf{q}_{-env}(\tau)$, where $\mathbf{q}_{env}(\tau)$ is defined as the envelope passing through $\mathbf{q}_1$, and with $\mathbf{q}_{-env}(\tau) = \mathbf{q}_{env}(\tau)^{-1}$. It can also be observed from Fig. 3.5 that envelope $\mathbf{q}_{env}(\tau)$ ends at $\mathbf{q}_2$ for even numbers of arcs and at

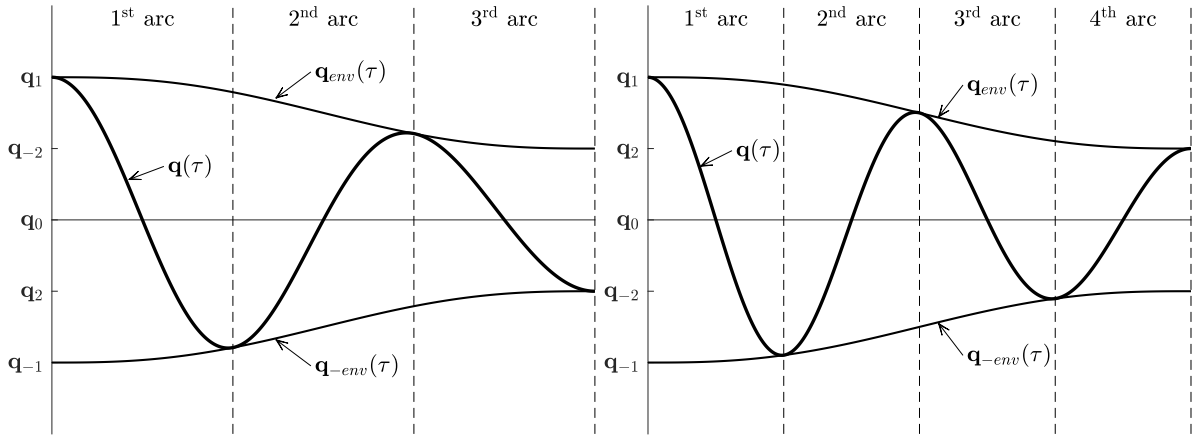

(a) Odd number of arcs. (b) Even number of arcs.

Figure 3.5 – Schematic representation of the proposed rotational trajectory.

$\mathbf{q}_{-2} = \mathbf{q}_2{}^{-1}$ for odd numbers of arcs. Hence, the final point of envelope $\mathbf{q}_{env}(\tau)$, denoted $\mathbf{q}_{\pm 2}$, can be expressed in compact form as

$$\mathbf{q}_{\pm 2} = \begin{bmatrix} \cos\left(\dfrac{\gamma_2}{2}\right) \\ (-1)^p \mathbf{e}_2 \sin\left(\dfrac{\gamma_2}{2}\right) \end{bmatrix} = \mathbf{q}_0 \mathbf{q}_0^T \mathbf{q}_2 + (-1)^p (\mathbf{1} - \mathbf{q}_0 \mathbf{q}_0^T) \mathbf{q}_2, \tag{3.58}$$

which is valid whether the number of arcs p is odd or even, and where eq. (3.28) has been employed to write the rightmost side of the above relation. As a result, envelope $\mathbf{q}_{env}(\tau)$ can be modeled using the standard definition of SLERP (3.34) as

$$\mathbf{q}_{env}(\tau) = \mathbf{q}_1 \frac{\sin\left(\Theta_{env}(1 - A_O(\tau))\right)}{\sin(\Theta_{env})} + \mathbf{q}_{\pm 2} \frac{\sin(\Theta_{env} A_O(\tau))}{\sin(\Theta_{env})}, \tag{3.59}$$

with

$$\Theta_{env} = \arccos(\mathbf{q}_1^T \mathbf{q}_{\pm 2}), \tag{3.60}$$

and where the amplitude function $A_O(\tau)$ is a smooth monotonic function that admits

$$A_O(0) = 0 \qquad \text{and} \qquad A_O(1) = 1 \tag{3.61}$$

for envelope (3.59) to satisfy $\mathbf{q}_{env}(0) = \mathbf{q}_1$ and $\mathbf{q}_{env}(1) = \mathbf{q}_{\pm 2}$, as required. In addition, it can be shown that function $A_O(\tau)$ must also have

$$A_O'(0) = A_O'(1) = A_O''(0) = A_O''(1) = 0, \tag{3.62}$$

where $f'(\cdot)$ stands for the derivative of f with respect to its argument. The above equation ensures that the trajectory admits a zero angular velocity at its endpoints and the continuity of the angular acceleration at the junction with the preceding and following trajectory segments. Indeed, the endpoint angular acceleration can be different from zero despite having $A_O''(0) = A_O''(1) = 0$ because of the form of eq. (3.59). In light of eq. (3.52) and eqs. (3.61)–(3.62), the

same amplitude function can be used for both the translational and rotational motion, i.e., one can use

$$A_O(\tau) = A(\tau). \tag{3.63}$$

This approach is used in the simulations of Section 3.12.

The expressions for the envelopes $\mathbf{q}_{env}(\tau)$ and $\mathbf{q}_{-env}(\tau)$ being determined, the oscillating motion of the platform between them can be cast, by virtue of eq. (3.36), as an extended SLERP between $\mathbf{q}_0$ and $\mathbf{q}_{env}(\tau)$ in which the time function $\beta(\tau)$ oscillates between 1 and -1, namely

$$\mathbf{q}(\tau) = \mathbf{q}_0 \frac{\sin\left(\Theta(\tau)(1-\beta(\tau))\right)}{\sin(\Theta(\tau))} + \mathbf{q}_{env}(\tau) \frac{\sin\left(\Theta(\tau)\beta(\tau)\right)}{\sin(\Theta(\tau))} \qquad -1 < \beta(\tau) < 1, \tag{3.64}$$

with

$$\Theta(\tau) = \arccos(\mathbf{q}_0^T \mathbf{q}_{env}(\tau)), \tag{3.65}$$

where $\mathbf{q}(\tau) = \mathbf{q}_0$ when the oscillating function $\beta(\tau) = 0$, $\mathbf{q}(\tau) = \mathbf{q}_{env}(\tau)$ when $\beta(\tau) = 1$ and $\mathbf{q}(\tau) = \mathbf{q}_{-env}(\tau)$ when $\beta(\tau) = -1$. Naturally, function $\beta(\tau)$ must be oscillating with the same frequency and in phase with the translational motion and, for eq. (3.64) to satisfy the boundary constraints, must in addition have $\beta(0) = 1$, $\beta(1) = (-1)^p$, and $\beta'(0) = \beta'(1) = 0$. Numerous continuous functions meet these constraints, for instance

$$\beta_1(\tau) = \cos(p\pi\tau) \tag{3.66}$$

$$\beta_0(\tau) = \frac{9\cos(p\pi\tau) - \cos(3p\pi\tau)}{8} \tag{3.67}$$

$$\beta_f(\tau) = \frac{\left(9 + \frac{\ddot{\beta}_{ep}}{p^2\pi^2}\right)\cos(p\pi\tau) - \left(1 + \frac{\ddot{\beta}_{ep}}{p^2\pi^2}\right)\cos(3p\pi\tau)}{8}. \tag{3.68}$$

The expressions defined above are put forward as candidates for the oscillating time function of the rotational motion since they each exhibit a special characteristic in addition to satisfying the aforementioned constraints. First of all, eq. (3.66) is a function that uses only one term to match all kinematic constraints, which in itself is worth pointing out. Secondly, function $\beta_0(\tau)$ is a simple function that ensures $\beta''(0) = \beta''(1) = 0$ in addition to satisfying the mandatory constraints, thus making the angular acceleration vanish at the endpoints. Finally, eq. (3.68) keeps the value of its second derivative free at the endpoints so that it can be fixed independently for each point-to-point trajectory by adjusting parameter $\ddot{\beta}_{ep}$. In the next section, among other things, a procedure for selecting the value of $\ddot{\beta}_{ep}$ that maximizes the likelihood of generating a feasible trajectory is proposed.

3.8 Trajectory Endpoints

For cable-suspended mechanisms, special attention must be devoted to endpoints of point-to-point trajectories since the prescribed pose and zero velocity constraint ensure that only the

translational and angular accelerations can be adjusted to guarantee positive tensions in the cables. Specifically, the zero angular velocity constraint reshapes eq. (3.11) as

$$-\mathbf{J}^T\boldsymbol{\mu} = \begin{bmatrix} \ddot{\mathbf{p}}_{ep} - \mathbf{g} \\ \frac{1}{m}\mathbf{Q}\mathbf{I}_G\mathbf{Q}^T\dot{\boldsymbol{\omega}}_{ep} \end{bmatrix}, \tag{3.69}$$

where the subscript *ep* stands for the endpoint pose of the platform. The above expression encapsulates the six equations of the dynamic model of the mechanism at a trajectory endpoint. These expressions comprise two free parameters, the acceleration vector $\ddot{\mathbf{p}}_{ep}$ and the angular acceleration vector $\dot{\boldsymbol{\omega}}_{ep}$, which account for six independent variables. Therefore, by fixing these six parameters appropriately, the six equations of eq. (3.69) can be satisfied for any given endpoint pose of the platform for any vector of positive tension $\boldsymbol{\mu} \succeq \mathbf{0}$. Hence, the unilaterality of the forces in the cables does not prevent any endpoint pose from being accessed with a zero endpoint velocity. In particular, vectors $\ddot{\mathbf{p}}_{ep}$ and $\dot{\boldsymbol{\omega}}_{ep}$ can be set such that the ideal kinematic states—relation (3.14)—is fulfilled at the endpoint. In doing so, the endpoint kinematic state is the farthest away from zero-tension loci, thereby maximizing the likelihood that the next trajectory segment be achieved with tensile-only forces in the cables (Dion-Gauvin and Gosselin, 2017, 2018). Therefore, the following important result is obtained: *in cable-suspended parallel mechanisms, the unilaterality constraint of the forces in the cables does not limit the space of end-effector poses that can be reached with zero velocity and, furthermore, the translational and angular accelerations at a given pose can be adjusted to maximize the likelihood that the incoming and outgoing trajectory segments be achieved with tensile-only forces in the cables.*

This statement, however, does not hold for endpoints reached by the trajectory planning procedure developed in this paper. Specifically, the trajectory formulation presented in Sections 3.6 and 3.7 does not keep the endpoint translational and angular accelerations free but rather sets them to, respectively,

$$\ddot{\mathbf{p}}_{ep} = -\frac{\theta_h^2(n_h - 1)}{T^2}(\mathbf{p}_{ep} - \mathbf{p}_0) \tag{3.70}$$

and

$$\dot{\boldsymbol{\omega}}_{ep} = \frac{2\ddot{\beta}_{ep}\gamma_{ep}}{T^2}\mathbf{e}_{ep}. \tag{3.71}$$

In eqs. (3.70)–(3.71), parameters n_h, θ_h, $\mathbf{p}_0$, $\mathbf{p}_{ep}$, γ_{ep}, and $\mathbf{e}_{ep}$ all either depend on the trajectory or the endpoint pose, and hence only the duration of the trajectory T and parameter $\ddot{\beta}_{ep}$ can be adjusted to generate positive tensions in the cables. Since, for a trajectory connecting two endpoint poses, eq. (3.69) comprises more constraint equations at the endpoints (12) than there are parameters to be adjusted (3) [2], it cannot be guaranteed that there exists values of these parameters that induce positive tensions in the six cables at the two endpoint poses of a trajectory. In particular, the direction of the angular acceleration being fully determined

2. a unique duration T (1) and parameters $\ddot{\beta}_1$ and $\ddot{\beta}_2$ at the initial and final points (2).

by the trajectory formulation, the ideal kinematic states relation (3.14) can only be fulfilled for certain endpoint poses of the platform. Still, this idea remains key to generating tensile-only trajectory segments and in the next sections, it is nevertheless put to use to determine, when they exist, the values of T and $\ddot{\beta}_{ep}$ that bring endpoint kinematic states as far from zero-tension loci as the trajectory formulation permits it.

3.8.1 Duration of the Trajectory

While the ideal kinematic states relation (3.14) cannot be fully imposed at the endpoints of a trajectory performed under the proposed formulation, the duration of the trajectory T can be set such that the translational components of eq. (3.14) be equal to one another. Moreover, these components being much greater than their rotational counterparts, prescribing that they be equal essentially fulfills eq. (3.14). Reproducing for quick reference the ideal kinematic states relation (3.14) as

$$\eta \begin{bmatrix} -\mathbf{p} \\ \mathbf{m} \end{bmatrix} = \begin{bmatrix} \ddot{\mathbf{p}} - \mathbf{g} \\ \frac{1}{m}\dot{\mathbf{h}}_G \end{bmatrix}, \tag{3.72}$$

it can be observed, for typical point-to-point motions of cable-suspended mechanisms [3], that

$$\frac{\|\mathbf{p}\|}{\|\mathbf{m}\|} \approx \frac{\|\ddot{\mathbf{p}} - \mathbf{g}\|}{\frac{1}{m}\|\dot{\mathbf{h}}_G\|} > 50. \tag{3.73}$$

Hence the rotational components of the ideal kinematic states relation are negligible in comparison to their translational counterparts. Neglecting their contribution in eq. (3.72) leads to the relation

$$-\eta \begin{bmatrix} \mathbf{p} \\ \mathbf{0} \end{bmatrix} = \begin{bmatrix} \ddot{\mathbf{p}} - \mathbf{g} \\ \mathbf{0} \end{bmatrix}, \tag{3.74}$$

which can be described as the translational approximation of the ideal kinematic states relation. The accuracy of this approximation with respect to the exact relation can be estimated by evaluating the relative error between the vectors on the left-hand side (or the right-hand side) of the two expressions, namely

$$e = \frac{\left\| \begin{bmatrix} -\mathbf{p} \\ \mathbf{0} \end{bmatrix} - \begin{bmatrix} -\mathbf{p} \\ \mathbf{m} \end{bmatrix} \right\|}{\left\| \begin{bmatrix} -\mathbf{p} \\ \mathbf{m} \end{bmatrix} \right\|} = \frac{\left\| \begin{bmatrix} \mathbf{0} \\ \mathbf{m} \end{bmatrix} \right\|}{\left\| \begin{bmatrix} -\mathbf{p} \\ \mathbf{m} \end{bmatrix} \right\|} \approx \frac{\|\mathbf{m}\|}{\|\mathbf{p}\|}, \tag{3.75}$$

and thus amounts to, by virtue of eq. (3.73),

$$e < 0.02. \tag{3.76}$$

3. For example, for the mechanism used in the example trajectory (see Section 3.12.2), a position of the end-effector $\mathbf{p} = \begin{bmatrix} 1.5b & 1.5b & 1.5 \end{bmatrix}^T$, and an orientation in the T&T angle convention ($\phi = 45°, \theta = 30°, \sigma = 15°$), one gets $\|\mathbf{p}\| / \|\mathbf{m}\| > 100$.

Hence the relative error made by using the translational approximation of the ideal kinematic states relation in place of the exact expression corresponds to the ratio of the magnitudes of the rotational components to the translational components obtained in eq. (3.73) and is below 2%. Correspondingly, applying eq. (3.74) at a trajectory endpoint instead of the exact relation equivalently maximizes the likelihood that the preceding and following trajectory segments be achieved with tensile-only forces in the cables. Solving eq. (3.74) at a trajectory endpoint for the duration of the trajectory T yields, using eq. (3.70),

$$T^2 = \theta_h^2(n_h - 1)\frac{z_0}{g}, \tag{3.77}$$

along with

$$\eta = \frac{g}{z_0}. \tag{3.78}$$

The above two equations represent respectively the duration of trajectory and the *combined* tension in the six cables that allow the ideal kinematic states relation to be nearly fulfilled at the trajectory endpoints. For this reason, eq. (3.77) is used to set the duration of the trajectory with the proposed formulation. Moreover, considering that, by virtue of eqs. (3.54)–(3.55), $\theta_h^2(n_h - 1) \approx \pi^2 p^2$ for all but small values of p, it is apparent that eq. (3.77) is akin to the equation of the period of a simple pendulum, in that the duration increases linearly with the number of arcs (half-oscillations).

3.8.2 Parameter $\ddot{\beta}_{ep}$

Parameter $\ddot{\beta}_{ep}$ represents the value of the second derivative of the interpolation function $\beta(\tau)$ at the endpoint. Referring to eq. (3.71), this parameter governs the magnitude of angular acceleration at the endpoint, and thereby opting for an interpolation function $\beta(\tau)$ that keeps this parameter free allows to control the magnitude of the rotational component of the force-balance equation (3.69) at the endpoint. This expression can be rewritten, using eqs. (3.71), (3.74), (3.77) and (3.78), as

$$-\mathbf{J}^T\boldsymbol{\mu} = \begin{bmatrix} -\frac{g}{z_0}\mathbf{p}_{ep} \\ \hat{\ddot{\beta}}_{ep}\boldsymbol{\phi}_{ep} \end{bmatrix}, \tag{3.79}$$

where vector $\boldsymbol{\phi}_{ep}$ and parameter $\hat{\ddot{\beta}}_{ep}$ are respectively given by

$$\boldsymbol{\phi}_{ep} = \frac{2}{m}\frac{g}{z_0}\gamma_{ep}\mathbf{Q}\mathbf{I}_G\mathbf{e}_{ep} \tag{3.80}$$

and

$$\hat{\ddot{\beta}}_{ep} = \frac{\ddot{\beta}_{ep}}{\theta_h^2(n_h - 1)}, \tag{3.81}$$

and where parameter $\hat{\ddot{\beta}}_{ep}$ is a function of parameter $\ddot{\beta}_{ep}$ and the trajectory parameters θ_h and n_h that remain to be determined. Hence, by determining parameter $\hat{\ddot{\beta}}_{ep}$ first, parameter $\ddot{\beta}_{ep}$ can be retrieved from eq. (3.81) once a feasible number of arcs is found. In this regard,

recalling that ideal kinematic states are characterized by having equal tension in all six cables, a sensible approach for fixing $\hat{\ddot{\beta}}_{ep}$ is to minimize the sum of the squared differences between each cable tension μ_i and the tension $\eta/6$ of the preceding section that nearly fulfils the ideal kinematic states relation. Specifically, letting vector $\boldsymbol{\delta} = \begin{bmatrix} \delta_1 & \delta_2 & \dots & \delta_6 \end{bmatrix}^T$ denote the deviation of each cable tension with respect to the tension of reference, namely

$$\boldsymbol{\mu} = \frac{\eta}{6}\mathbf{1}_6 + \boldsymbol{\delta} \tag{3.82}$$

where $\mathbf{1}_n = \begin{bmatrix} 1 & 1 & \dots & 1 \end{bmatrix}^T \in \mathbb{R}^n$, the previously described objective function can be expressed as

$$f(\hat{\ddot{\beta}}_{ep}) = \frac{1}{2}\boldsymbol{\delta}^T\boldsymbol{\delta}, \tag{3.83}$$

and correspondingly the optimization problem can be formulated as

$$\begin{aligned} \text{minimize} \qquad & f(\hat{\ddot{\beta}}_{ep}) = \frac{1}{2}\boldsymbol{\delta}^T\boldsymbol{\delta} && \text{(3.84a)} \\ \text{subject to} \qquad & \boldsymbol{\mu} = \frac{\eta}{6}\mathbf{1}_6 + \boldsymbol{\delta}, && \text{(3.84b)} \\ & -\mathbf{J}^T\boldsymbol{\mu} = \begin{bmatrix} -\frac{g}{z_0}\mathbf{p}_{ep} \\ \hat{\ddot{\beta}}_{ep}\boldsymbol{\phi}_{ep} \end{bmatrix}, && \text{(3.84c)} \\ & \boldsymbol{\mu} \succeq \mathbf{0}. && \text{(3.84d)} \end{aligned}$$

The above problem consists of a univariate quadratic program that can be solved analytically. First of all, substituting eq. (3.84b) into the force balance equation at the endpoint (3.84c) and making use of the ideal kinematic states relation yield an equation depending only on vector $\boldsymbol{\delta}$, namely

$$-\mathbf{J}^T\boldsymbol{\delta} = \begin{bmatrix} \mathbf{0} \\ \boldsymbol{\xi} \end{bmatrix}, \tag{3.85}$$

with

$$\boldsymbol{\xi} = \hat{\ddot{\beta}}_{ep}\boldsymbol{\phi}_{ep} - \eta\mathbf{m}. \tag{3.86}$$

Moreover, eq. (3.85) having its first three components equal to zero, a symbolic expression for vector $\boldsymbol{\delta}$ is readily obtained as

$$\boldsymbol{\delta} = \begin{bmatrix} -\mathbf{A}^{-1}\mathbf{B}\mathbf{E}^{-1}\boldsymbol{\xi} \\ \mathbf{E}^{-1}\boldsymbol{\xi} \end{bmatrix}, \tag{3.87}$$

where the 3×3 matrices $\mathbf{A}$, $\mathbf{B}$, $\mathbf{C}$, and $\mathbf{D}$ partition matrix $-\mathbf{J}^T$ as

$$-\mathbf{J}^T = \begin{bmatrix} \mathbf{A} & \mathbf{B} \\ \mathbf{C} & \mathbf{D} \end{bmatrix}, \tag{3.88}$$

and where $\mathbf{E} = \mathbf{D} - \mathbf{C}\mathbf{A}^{-1}\mathbf{B}$ is the Schur complement of block $\mathbf{A}$ of matrix $-\mathbf{J}^T$ (Zhang, 2005). Finally, rewriting eq. (3.87) as

$$\boldsymbol{\delta} = \mathbf{u} + \hat{\ddot{\beta}}_{ep}\mathbf{v}, \tag{3.89}$$

with

$$\mathbf{u} = \eta \begin{bmatrix} \mathbf{A}^{-1}\mathbf{B}\mathbf{E}^{-1}\mathbf{m} \\ -\mathbf{E}^{-1}\mathbf{m} \end{bmatrix} \qquad \text{and} \qquad \mathbf{v} = \begin{bmatrix} -\mathbf{A}^{-1}\mathbf{B}\mathbf{E}^{-1}\boldsymbol{\phi}_{ep} \\ \mathbf{E}^{-1}\boldsymbol{\phi}_{ep} \end{bmatrix}, \tag{3.90}$$

the substitution of eq. (3.89) into the objective function and into the equation setting to zero the first derivative of f with respect to $\ddot{\hat{\beta}}_{ep}$ yields, upon solving for $\ddot{\hat{\beta}}_{ep}$,

$$\ddot{\hat{\beta}}_{ep} = -\frac{\mathbf{u}^T\mathbf{v}}{\mathbf{v}^T\mathbf{v}}. \tag{3.91}$$

The above equation is the expression of the lone critical point of eq. (3.84a). It can be shown that it corresponds to the global minimum of the objective function f, and hence it is the solution to the optimization problem (3.84) provided that it satisfies the inequality constraints (3.84d). Using eq. (3.84b) and eq. (3.89), these constraints can be expressed in terms of parameter $\ddot{\hat{\beta}}_{ep}$ as

$$\eta\mathbf{1}_6 + \mathbf{u} + \ddot{\hat{\beta}}_{ep}\mathbf{v} \succeq \mathbf{0}, \tag{3.92}$$

which describes the interval of values of $\ddot{\hat{\beta}}_{ep}$ that lead to positive tensions in the six cables. The value for $\ddot{\hat{\beta}}_{ep}$ given by eq. (3.91) is the preferred solution in the trajectory formulation, provided that it lies in this interval. However, should this not be the case, then either other solutions for $\ddot{\hat{\beta}}_{ep}$ exist, in which case a central point of the interval can be used, or eq. (3.92) corresponds to the empty interval, in which case no value of $\ddot{\hat{\beta}}_{ep}$ produces tensile-only forces at the endpoint and the proposed formulation cannot be employed to reach the considered endpoint pose. Obviously, if the interval (3.92) is non-empty but the selected value fails to produce a feasible motion, other values of $\ddot{\hat{\beta}}_{ep}$ in the interval can be tested before inferring that the proposed trajectory formulation cannot be used to reach the considered endpoint pose.

Hence, the procedure described above yields the best value of parameter $\ddot{\hat{\beta}}_{ep}$ for given initial and final poses of the point-to-point trajectory. However, this is problematic since the oscillating functions $\beta(\tau)$ developed in Section 3.7 are based on sinusoidal functions that admit the same second derivative at both endpoints. To circumvent this issue, the following can be used

$$\beta_{ff}(\tau) = (1-\tau)\beta_{f1}(\tau) + \tau\beta_{f2}(\tau), \tag{3.93}$$

where $\beta_{f1}(\tau)$ and $\beta_{f2}(\tau)$ are the interpolation function $\beta_f(\tau)$ given in eq. (3.68) in which parameter $\ddot{\beta}_{ep}$ takes the value obtained for the initial and final endpoint pose, respectively. As expected, the above expression complies with all the necessary boundary constraints since it consists of a linear combination of function $\beta_{f1}(\tau)$ that satisfies the conditions at the initial pose and $\beta_{f2}(\tau)$ that satisfies the conditions at the final pose. The effectiveness of the relations derived in this section is demonstrated in Section 3.12.

3.9 Static-to-Dynamic Transition Trajectory

Static-to-dynamic transition trajectories constitute a special case of point-to-point trajectories, whereby a pose with non-zero final acceleration in the dynamic workspace is reached from a pose at rest in the static workspace of the mechanism. A static-to-dynamic trajectory segment can be used to reach the first of a series of target poses in a dynamic state or, by reversing it, to return the end-effector to the static workspace once all prescribed target poses have been reached.

By contrast with trajectory planning intended for general parallel mechanisms, great care must be taken in the selection of the pose at rest in the static workspace for trajectory planning of cable-suspended mechanisms. Specifically, because of the unilaterality of the cable forces, it must be ensured that the starting and ending poses of the trajectory correspond to static equilibrium poses of the platform.

The trajectory formulation derived in the preceding sections can be integrally used to perform static-to-dynamic transition trajectories. The resulting motion consists of translational and rotational oscillations of progressively increasing amplitude centred at the static pose, similar in its translational component to the formulation derived in Dion-Gauvin and Gosselin (2017) for the point-mass end-effector of a 3-dof cable-suspended mechanism. With regards to the determination of the pose at rest in the static workspace, the translational component of the transition trajectory must start or end at point P_0 in the static workspace for the translational acceleration to be continuous at the pose to be reached in a dynamic state. For this static position, the platform is in static equilibrium when the plane of its cable attachment points is parallel to the horizontal base plane and when the sum of the projections of unit vectors defined along the cables onto this horizontal plane is minimal, i.e., when the platform is in the reference orientation, and hence this orientation imposes itself as the starting and ending orientation at rest of the end-effector. These static position and orientation of the platform together satisfy the ideal kinematic states relation (3.14), thereby increasing the likelihood that the transition trajectory be feasible.

3.10 Workspace Analysis

Before evaluating the feasibility of the above trajectory formulation for different target poses, the workspace of the mechanism must be determined in order to identify which final poses of the platform may or may not be attainable by the cable-suspended mechanism. For general parallel mechanisms, the workspace is usually defined as the set of all poses of the platform that are accessible without the (active and passive) joints exceeding their mechanical limits nor the legs and platform interfering (colliding) with one another. For cable-suspended mechanisms however, the passive rotational joints consisting of eyelets on the base and on the platform, along with the commonly accepted assumption that the cables, the actuated

translational joints, are of infinite length, ensure that neither passive nor active joints have a restricted range of motion. As a result, only the interference between the cables and with the platform circumscribes the workspace of cable-driven mechanisms. However, since singularities usually complexify navigating through this workspace, its subregions whose access entails their crossing are sometimes not considered as belonging to the set of accessible poses, leading to the notion of singularity-free workspace. Since, to the best of our knowledge, no general trajectory planning procedure exists for crossing singularities of cable-suspended hexapods whose actuators can only exert unilateral forces, the detection of this type of singularity is added here to the determination of the workspace.

3.10.1 Translational Workspace

The translational workspace consists of the set of all the positions of the platform that can be reached with at least one orientation. Considering the absence of restriction on the range of cable-mechanism joints, the translational workspace of cable-suspended mechanisms is quite large, which is a well-known non-negligible advantage of this type of mechanism. Moreover, for standard polyhedral architectures, any configuration with the reference orientation $\mathbf{Q} = \mathbf{1}$ is indeed convex (see Section 3.4.3), which prevents cable interference, platform interference, and singularities from occurring below the plane of the base. Thus the translational workspace of cable-suspended hexapods is limited by neither joint ranges, nor mechanical interferences, nor singularity crossings and hence comprises all the points that are located below the plane of the cable spools.

3.10.2 Orientational Workspace

The orientational workspace is defined as the set of all the accessible orientations of the platform about a predetermined point. The algorithm proposed by Bonev (Bonev and Ryu, 2001) is perfectly suited for computing the orientational workspace of cable-suspended mechanisms. This algorithm exploits the benefits of the tilt and torsion (T&T) angle convention, which is a convention that uses two rotations defined by three angles to represent an arbitrary orientation: first, a tilt by an angle θ about an axis of rotation which is constrained to a given plane and whose direction in that plane is given by the azimuth angle ϕ; and second, a torsion by an angle σ about an axis perpendicular to the (now rotated) plane. With respect to general parallel mechanisms, ensuring that the tilt axis is contained in the base plane allows the tilt and torsion rotations to correspond to the actual physical rotations of the platform, thus making the T&T convention ideal for representing the orientation for this type of mechanism. The T&T angle convention is equivalent to the $Z_\phi X_\theta Z_{\sigma-\phi}$ Euler angle convention for a base plane normal to the fixed Z-axis and an azimuth angle ϕ measured with respect to the positive direction of the X–axis.

The workspace algorithm developed by Bonev unveils feasible orientations by iterating through

the (ϕ, θ, σ) space from a starting orientation $(\phi_s, \theta_s, \sigma_s)$ that is accessible from the static workspace. Referring to the translational workspace analysis, the reference orientation $\mathbf{Q} = \mathbf{1}$ is known to be accessible regardless of the position of the platform, and hence it constitutes a suitable choice for the starting point of the algorithm. First, the starting value of the torsion angle σ_s is incremented toward π and then toward $-\pi$ to obtain the upper and lower part of the orientational workspace, respectively. For each value of angle σ, a scan of the azimuth angle ϕ is performed; for each value of angle ϕ, the tilt angle θ is incremented from θ_s toward $\theta_s + \pi$, until either mechanical interferences or singularities are detected. The maximum feasible value of angle θ for each (ϕ, σ) pair is then recorded. Once each cross-section $\sigma = \text{const}$ is completed, its geometric center (ϕ_c, θ_c) is calculated for it to be used as the first orientation to be tested for the next value of angle σ, $(\phi_s, \theta_s) \leftarrow (\phi_c, \theta_c)$. This is of particular importance for cable-suspended mechanisms since the zero-tilt of the reference orientation $(\phi_s, \theta_s) = (0, 0)$ gets farther from the centre of each cross-section $\sigma = \text{const}$ as the platform gets farther from the static workspace. As a whole, the stored (ϕ, θ, σ) values constitute the envelope of the orientational workspace for the chosen position of the platform.

It should be pointed out here that, unlike for general parallel mechanisms, the purely rotating motion connecting two orientations of a given orientation workspace is not feasible for cable-suspended mechanisms. Indeed, except in the very special case where the platform is in the static workspace, a purely rotational motion of the platform requires compressive forces in some of the cables to ensure that the centre of mass remains stationary. In order to connect two orientations belonging to the same orientational workspace, it is therefore necessary that the platform also perform a translational motion, either by returning to the static workspace or, referring to the notion of translational workspace, by moving to any other pose that is accessible from the static workspace. Nonetheless, the determination of the orientational workspace remains relevant for cable-suspended mechanisms since it provides all the *target* orientations of a predetermined point that are accessible from any other position of the translational workspace. In the next sections, tests detecting cable interference, platform interference, and singularities are presented.

Cable Interference

Poses that are inaccessible because of cable interference are poses that cannot be attained from the initial configuration of the mechanism without cables previously colliding with one another. For a given pair of cables, let $\mathbf{d}$ be the vector of shortest distance connecting the vectors $\boldsymbol{\rho}_k$ associated with the two cables. Then, cable interference can be verified for each pair of cables that may collide by comparing, between two neighbouring poses, the direction of vector $\mathbf{d}$ at the two poses. This method is preferred here over the more common approach of calculating the minimum distance between each cable since the latter would require a prohibitively small discretization to reliably detect all cable interferences, whereas

a reasonably-sized mesh can be used with the approach preferred in this paper. For every pair of cables, vector $\mathbf{d}$ is obtained by first determining the vector of shortest distance that connects the two straight lines supporting these vectors, which is orthogonal to both straight lines. Then, if necessary, each endpoint of this vector is slid along its respective straight line until it finds itself on the line segment coinciding with vector $\boldsymbol{\rho}_k$, yielding vector $\mathbf{d}$. Let $\mathbf{d}_i$ be the vector for the pose currently visited by the algorithm, and let $\mathbf{d}_{i-1}$ be the vector for an adjacent pose that is known to be accessible.

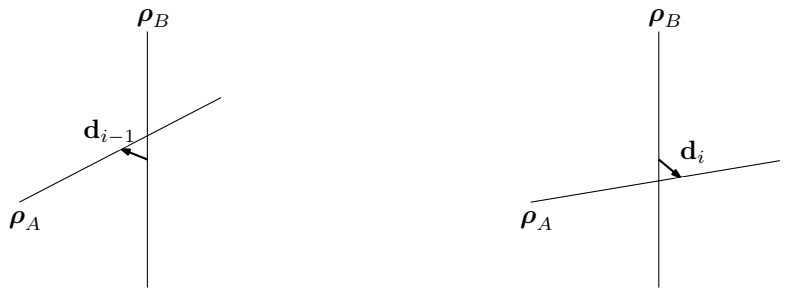

(a) Position at pose $i-1$. (b) Position at pose i.

Figure 3.6 – Relative position of two given vectors $\boldsymbol{\rho}_k$ for corresponding cables interfering between poses $i-1$ and i.

Then, as it is indicated in Fig. 3.6, two cables colliding with one another between poses $i-1$ and i have vectors $\mathbf{d}_{i-1}$ and $\mathbf{d}_i$ pointing in opposite directions, which is to say that vectors $\mathbf{d}_{i-1}$ and $\mathbf{d}_i$ pointing toward the same direction denotes cables not interfering with one another, namely

$$\mathbf{d}_{i-1}{}^T\mathbf{d}_i > 0. \tag{3.94}$$

The above inequality is satisfied for a given pair of cables when no collision of these cables is present between the current orientation and the rest of the workspace [4]. Therefore, it must be satisfied for all the combinations of two cables of the mechanism for an orientation not to be ruled out from the workspace because of cable interference.

Platform Interference

Poses that are inaccessible because of platform interference are poses that cannot be attained from the initial configuration of the mechanism without at least one cable colliding with the platform. For each cable k, let $\boldsymbol{\nu}_k = -\boldsymbol{\rho}_k$ be the vector associated with the corresponding cable that emanates from the cable attachment point A_k on the platform. Then, as the trajectory is carried out, the motion of vector $\boldsymbol{\nu}_k$ in three dimensional space defines a surface and platform interference can be verified by determining whether this surface intersects the

4. Although unlikely, a very brief interference between two cables with a very short 'crossing' distance could still go undetected by the method presented here. However, in practice, the compliance of the cable mechanism can be assumed to passively and easily handle this situation. This is often advocated as an advantage of cable mechanisms. It is deemed reasonable to neglect such a case.

platform. As it can be observed from Fig. 3.7, this surface can be approximated between two neighbouring poses by the plane spanned by the vectors $\boldsymbol{\nu}_k$ at the two poses, respectively denoted $\boldsymbol{\nu}_{k,i-1}$ and $\boldsymbol{\nu}_{k,i}$, while a second plane can also be constructed for representing the platform, namely by defining the vectors $\mathbf{s}_{k1}$ and $\mathbf{s}_{k2}$ connecting the attachment point A_k to the two adjacent attachment points along the edges of the platform. Clearly, these two planes necessarily intersect since they share a common point A_k, and hence verifying the interference between the platform and the k-th cable amounts to determining whether the straight line intersecting the two planes is both 1) in the portion of the plane spanned by vector $\boldsymbol{\nu}_k$ that is actually swept by this vector between poses $i-1$ and i; and 2) in the portion of the platform plane that is physically occupied by the platform. While the equation of the straight line belonging to both planes is readily obtained, it suffices that it can be written as both a linear combination *with positive weights* of the vectors $\boldsymbol{\nu}_{k,i-1}$ and $\boldsymbol{\nu}_{k,i}$, and a linear combination *with positive weights* of the vectors $\mathbf{s}_{k1}$ and $\mathbf{s}_{k2}$, for this straight line to be located in the critical region of each plane. In this instance, the cable associated with the corresponding vector $\boldsymbol{\nu}_k$ collides with the platform between poses $i-1$ and i and, if one of these poses is known to be accessible, the other can be excluded from the workspace with certainty. Ensuring that no platform interference occurs with any of the cables is necessary for a pose not to be ruled out from the orientational workspace because of platform interference.

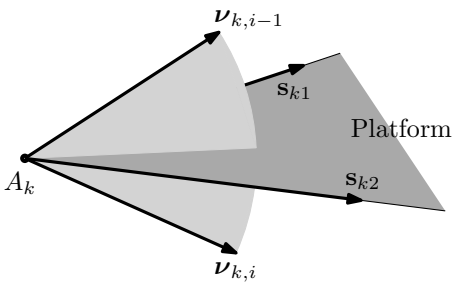

Figure 3.7 – Position of vector $\boldsymbol{\nu}_k$ for a corresponding cable k interfering with the platform between poses $i-1$ and i.

It should be pointed out that using this platform interference detection technique corresponds exactly to testing whether each cable k intersects the edges of the platform that are not incident to its attachment point A_k, i. e., segment $\overline{A_{k-1}A_{k+1}}$ on the platform. Therefore, employing this technique along with the cable interference detection technique on cable $k-1$, segment $\overline{A_{k-1}B_{k-1}}$, and cable $k+1$, segment $\overline{A_{k+1}B_{k+1}}$, creates for each cable k an impenetrable boundary $\overline{B_{k-1}A_{k-1}A_{k+1}B_{k+1}}$ that prevents from being connectable any two poses for which any cable would have to go around the platform. Hence, each cable k cannot go around the platform without interfering with its adjacent cables $k-1$ or $k+1$.

Singularities

Singular configurations are poses of a mechanism for which not all velocities can be produced at the end-effector or poses for which some non-zero velocities are possible at the end-effector with zero velocities of the actuators. Recalling eq. (3.4), Type I singularities are characterised by $\det(\mathbf{K}) = 0$, while Type II singularities are characterised by $\det(\mathbf{J}) = 0$. Singularities may impede the trajectory planning of the end-effector.

It should be pointed out, however, that it is not impossible for an end-effector to cross Type II singularities (Hesselbach et al., 2002; Hill et al., 2017). Indeed, it suffices that, as in nonsingular configurations, the velocity relation (3.4) and the dynamic model (3.11) be satisfied by having their right-hand side vector in the column space of matrix $\mathbf{J}$ and $\mathbf{J}^T$ respectively; this is possible, despite the fact that the Jacobian matrix $\mathbf{J}$ is not of full rank in singular configurations.

From a kinematic perspective, eq. (3.4), a singular matrix $\mathbf{J}$ implies the existence of a nonempty nullspace, meaning that some velocity of the end-effector can be achieved with zero velocity of the actuated joints. From a dynamic perspective, eq. (3.11), which is of greater relevance for dynamic trajectory planning, a singular matrix $\mathbf{J}$ implies that some inertial vector (or, in the static case, some external wrench) cannot be supported by the actuated joints. Furthermore, still with regard to eq. (3.11), the Gaussian elimination of matrix $\mathbf{J}^T$ augmented by the gravito-inertial vector on the right-hand side of eq. (3.11) yields in singular configurations a matrix whose last row(s) consist(s) of only zeros, except in the last column where the corresponding entry(ies) contain(s) dynamic expression(s) depending on the inertial properties of the platform, the angular velocity as well as the translational and angular acceleration of the platform. This(These) dynamic equation(s) is(are) akin to the dynamic expressions associated with the unactuated joints of an underactuated mechanism. Thus, a fully-actuated mechanism in a singular configuration can be construed as a mechanism having some of its dofs unactuated, and its other dofs redundantly actuated. Therefore, a trajectory planning procedure intended for crossing Type II singularities must at a singularity satisfy the dynamic equation of each unactuated dof as well as include a control strategy to manage the actuation redundancy of the redundantly actuated dofs. For cable-suspended mechanisms, this actuation redundancy means that the forces in the cables are no longer independent, making it more challenging (if not impossible?) to ensure positive tensions in a number of cables that is sufficient to maintain controllability.

All in all, there is, to our knowledge, no trajectory planning procedure meeting all the constraints required for crossing Type II singularities of cable-suspended hexapods. In particular, the trajectory proposed in this paper and its oscillating nature were devised with the sole purpose of maintaining positive tensions in the cables, and not with the aim of manoeuvering through Type II singularities. Consequently, Type II singularity crossing is regarded from the

outset as unfeasible, and thus any target pose separated by this type of singularity is deemed inaccessible by the mechanism.

Regarding the determination of the orientational workspace, two orientations separated by a Type II singularity admit Jacobian matrices $\mathbf{J}$ with determinants of opposite signs, and therefore any orientation whose matrix $\mathbf{J}$ has a determinant that differs in sign from that of an orientation known to be accessible, for example the reference orientation, is excluded from the workspace.

3.11 Trajectory Feasibility

The workspace obtained by the method described in the preceding section provides the final target poses that are accessible by cable-suspended hexapods. These target poses, however, may not all be attainable with the trajectory planning procedure described in this paper. In particular, for some target poses, the trajectory produced by the proposed formulation may at some point of the motion be also going through mechanical interferences or Type II singularities that prevent it from being feasible. Furthermore, the trajectory may induce negative tension in one or more cables along its path, thus making it unusable for reaching certain final poses of the platform. In the next section, tests detecting negative tension, cable interference, platform interference, and Type II singularity crossing that occur *along* the motion are provided.

3.11.1 Cable Tensions

Since the duration of a trajectory segment increases linearly with the number of arcs p (see Section 3.8.1), assessing the feasibility of the trajectory with regards to cable tensions amounts to determining, if it exists, the minimum number of arcs that yield positive tensions in all cables throughout the motion. Correspondingly, the trajectory is first attempted for $p = 1$ arc, which is progressively increased until a tensile-only motion is found. On the one hand, the translational trajectory given by eq. (3.44) is first written in the mechanism reference frame using eq. (3.43) and is differentiated twice with respect to time to yield the acceleration of the moving platform. The rotational trajectory, on the other hand, is obtained by first determining the appropriate value for $\ddot{\beta}_1$ and $\ddot{\beta}_2$ with the procedure described in Section 3.8.2. Then, the quaternions representing the orientations at the cusps $\mathbf{q}_{env}(\tau)$ and the rotational trajectory $\mathbf{q}(\tau)$ are consecutively calculated using eqs. (3.58)–(3.60) and eqs. (3.68), (3.64)–(3.65), respectively. The rotation matrix $\mathbf{Q}$, as well as the angular velocity and acceleration are thereafter determined with eqs. (3.29), (3.31)–(3.33) respectively. Then, the translational and rotational trajectories and their derivatives are temporally discretized. Then, for each time step $\tau_i \in [0, 1]$, the discrete trajectory values are substituted into the dynamic model (3.11), which is thereafter inverted numerically to yield the cable tensions at each time step, $\boldsymbol{\mu}_i$.

If the components of this vector are all positive for all $\tau_i \in [0,1]$, the trajectory is deemed satisfying the cable forces constraint. If, however, a negative tension is found in one or more cables at any particular time step, the trajectory is unfeasible and the computation of the cable forces is repeated with a number of arcs increased by one. This process is carried on until a number of arcs producing positive tensions in all cables is found, or until the candidate value is deemed unfit (too large) to be used in practice. Trajectories that have no suitable number of arcs that can produce tensile-only forces in all cables at all instants of the motion are deemed unfeasible for the considered target pose.

3.11.2 Cable Interference

The cable interference detection technique proposed in Section 3.10.2 for the determination of the orientational workspace can also be used to determine whether a given trajectory is collision-free. At each time step τ_i, vector $\mathbf{d}_i$ is computed for each combination of two cables and is compared with the corresponding one obtained at the preceding time step τ_{i-1}. If eq. (3.94) is violated for any pair of cables at any time step, the trajectory necessarily includes a configuration where two cables intersect and is thereby unfeasible.

3.11.3 Platform Interference

Platform interference occurring along a trajectory can be assessed by applying the detection technique developed in Section 3.10.2 between each time steps τ_i and τ_{i-1} along the motion. If such interference is detected between any time steps with any cable, the trajectory necessarily includes an inadmissible configuration and is thereby unfeasible.

3.11.4 Singularities

Similarly to what was done for the determination of the orientational workspace, the determinant of the Jacobian matrix $\mathbf{J}$ can be exploited to detect Type II singularity crossings occuring along the trajectory. Specifically, if at any particular time step $\tau_i \in [0,1]$ the determinant of matrix $\mathbf{J}$ differs in sign from that of a pose known to be accessible, such as the initial pose of reference, then the proposed trajectory includes Type II singularity configurations along its path and is unfeasible.

3.12 Simulations

In this section, results of computer simulations are presented to 1) demonstrate the feasibility of the proposed trajectory formulation and 2) assess the performance of the proposed rotational formulation in reaching a wide range of orientations for a given final point. These

simulations were performed for a MSSM architecture whose dimensions are given by

$$\mathbf{b}_1 = \mathbf{b}_2 = b \begin{bmatrix} 0 \\ 1 \\ 0 \end{bmatrix}; \qquad \mathbf{b}_3 = \mathbf{b}_4 = b \begin{bmatrix} -\frac{\sqrt{3}}{2} \\ -\frac{1}{2} \\ 0 \end{bmatrix}; \qquad \mathbf{b}_5 = \mathbf{b}_6 = b \begin{bmatrix} \frac{\sqrt{3}}{2} \\ -\frac{1}{2} \\ 0 \end{bmatrix}, \tag{3.95}$$

and

$$\mathbf{a}_1 = \mathbf{a}_6 = a \begin{bmatrix} \frac{\sqrt{3}}{2} \\ \frac{1}{2} \\ 0 \end{bmatrix}; \qquad \mathbf{a}_2 = \mathbf{a}_3 = a \begin{bmatrix} -\frac{\sqrt{3}}{2} \\ \frac{1}{2} \\ 0 \end{bmatrix}; \qquad \mathbf{a}_4 = \mathbf{a}_5 = a \begin{bmatrix} 0 \\ -1 \\ 0 \end{bmatrix}. \tag{3.96}$$

with $b = 0.86$ m and $a = 0.173$ m. Additionally, considering the triangular shape of the end-effector and assuming a thin platform, it is readily found that the inertia matrix of the platform with respect to its centre of mass is given in its reference frame by:

$$\mathbf{I}_G = \begin{bmatrix} \frac{1}{24}m(\sqrt{3}a)^2 & 0 & 0 \\ 0 & \frac{1}{24}m(\sqrt{3}a)^2 & 0 \\ 0 & 0 & \frac{1}{12}m(\sqrt{3}a)^2 \end{bmatrix}. \tag{3.97}$$

In the remainder of this section, the orientations are displayed using the T&T angle convention rather than in quaternion form to provide physical insight. Moreover, to illustrate the orientations that the proposed formulation can reach with respect to the central vertical axis of the mechanism, the T&T angle convention is expressed in a cylindrical coordinate system rather than in the fixed reference frame of the mechanism. This cylindrical coordinate system is introduced in the next subsection. Then, an example trajectory that comprises several point-to-point trajectory segments connected in sequence is examined. Finally, the proportion of orientations that can be reached from the static workspace by the proposed point-to-point motion is provided for some positions of the platform as a means of demonstrating the relevance of the proposed trajectory formulation.

3.12.1 Cylindrical Coordinate System

The proposed cylindrical reference frame is represented schematically in Fig. 3.8. Its origin is positioned at the centroid of the base attachment points and the axial Z_c–axis is perpendicular to the base plane and points in the direction of the reference pose of the end-effector. Moreover, the X_c–axis is aligned with the projection of the position vector of the platform in the XY–plane of the fixed reference frame such that the angle δ defined between the X_c–axis and the fixed X–axis is given by

$$\delta = \text{atan2}(y, x). \tag{3.98}$$

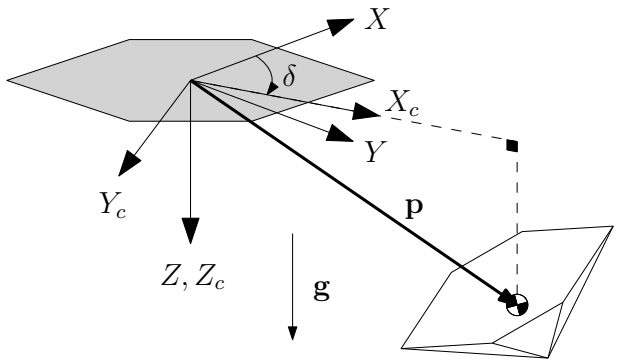

Figure 3.8 – Cylindrical reference frame.

Hence, expressing the orientation of the platform in the proposed cylindrical coordinate system yields the representation of the orientation of the end-effector with respect to the axis normal to the base plane passing by the centroid of the base attachment points, that is, with respect to the central axis of the mechanism. The main advantage of the proposed coordinate frame is that it is far more intuitive to envision orientations with respect to the central axis—and conceptualize rotations with respect to the axial, radial, and circumferential axes of the proposed cylindrical reference frame—than with respect to the arbitrary directions of the horizontal axes of any fixed reference frame.

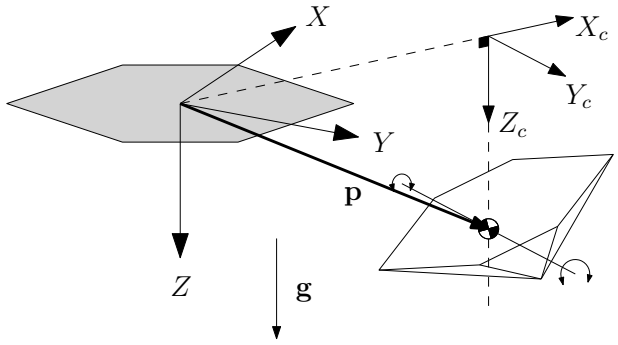

Figure 3.9 – Rotation with respect to the circumferential axis Y_c.

For example, consider the orientation illustrated in Fig. 3.9 whereby the platform is rotated toward the base of the mechanism. This orientation corresponds, in the cylindrical reference frame, to a rotation with respect to the circumferential axis Y_c and that, regardless of the position of the platform in the workspace. By contrast, no fixed reference frame provides a unique and intuitive description of this orientation.

Furthermore, when the T&T angle convention is used to describe the orientation of a body, casting this convention in the cylindrical reference frame makes it completely independent from the directions of the axes of the fixed reference frame and thus yields a fully intuitive understanding of the orientation. The importance of using such a representation should

not be underestimated. Specifically, one of the valuable characteristics of the T&T angle convention—and one of its main advantages over a standard Euler Angle representation—is that both the tilt and torsion rotations have physical meanings that correspond to the actual movement of the robot. By contrast, the rotations of a Euler Angle convention have no real physical basis since they are defined with respect to the axes of a fixed coordinate system, whose directions are fixed somewhat arbitrarily. Indeed, in order to reach a given orientation, the platform of general parallel mechanisms performs rotations that correspond to a pure tilt and a pure torsion, of magnitude respectively given by angles θ and σ that are used in the T&T angle convention. The third angle of this convention however—the azimuth angle ϕ representing the direction of the tilt axis in the base plane—has no real physical meaning since it is usually defined with respect to either the X– or Y–axis of the fixed coordinate frame. Accordingly, using the T&T angle convention in conjunction with the proposed cylindrical coordinate system allows to set the baseline of the azimuth angle to either the radial or circumferential axis, thereby providing a clear physical meaning to this angle, namely the angle between the tilt axis and either the circumferential or the radial direction of the mechanical system. In this framework, the T&T angle convention becomes completely independent from the arbitrary directions of the horizontal axes of the fixed reference frame and thus fully rooted in the physical reality of the mechanical system. In this respect, the proposed cylindrical reference frame can be construed as a natural extension to the T&T convention. In the next section, an example trajectory that connects a series of target points in sequence is examined.

3.12.2 Point-to-Point Trajectory

The example trajectory is described in Table 3.1 as a list of prescribed target poses—all located outside the static workspace—to be reached in sequence. The table, which also includes the starting and ending poses of the trajectory at rest as defined in Section 3.9, displays the endpoint positions of the platform in the fixed reference frame of the mechanism and the endpoint orientations by their T&T angle representation (ϕ, θ, σ) in the cylindrical reference frame. For this set of target positions, a value of $z_0 = 1.4$ m has been selected, which satisfies the necessary condition for feasibility but not the sufficient condition for translational feasibility. Specifically, as explained in Dion-Gauvin and Gosselin (2018), parameter z_0 must satisfy

$$z_0 > \max\left(\frac{z_1}{2}, \frac{z_2}{2}, \ldots, \frac{z_m}{2}\right) \tag{3.99}$$

for none of the m target points to be proven to be unattainable from the outset, while using a value for z_0 that satisfies

$$z_0 > \max\left(\frac{\mathbf{p}_1{}^T\mathbf{p}_1}{2z_1}, \frac{\mathbf{p}_2{}^T\mathbf{p}_2}{2z_2}, \ldots, \frac{\mathbf{p}_m{}^T\mathbf{p}_m}{2z_m}\right) \tag{3.100}$$

guarantees that the translational component of each trajectory segment can be performed by a point-mass end-effector with tensile-only forces in the cables. However, a value of z_0 satisfying condition (3.100) may not lead to the most efficient motion, i.e., that which minimizes the minimum feasible number of arcs for each trajectory segment. Hence, the decision on whether to use a value for z_0 that satisfies eq. (3.100) should be taken with some care.

Endpoint	Positions (m)	Orientations (ϕ, θ, σ)
0	$(0, 0, 1.4)$	(0,0,0)
1	$(3.464, 0, 1.3)$	$(\frac{\pi}{2}, \frac{5\pi}{6}, 0)$
2	$(-0.866, -1.5, 1.3)$	$(\pi, \frac{\pi}{3}, \frac{\pi}{2})$
3	$(-1.732, 3, 1.7)$	$(\frac{3\pi}{4}, \frac{\pi}{2}, \frac{\pi}{4})$
4	$(-3, -1.732, 1)$	$(\frac{\pi}{4}, \frac{\pi}{3}, -\frac{\pi}{4})$
5	$(1.5, -0.866, 1)$	$(0, \frac{\pi}{3}, -\frac{\pi}{2})$
6	$(0, 1.732, 1.7)$	$(\frac{\pi}{2}, -\frac{\pi}{6}, 0)$
0	$(0, 0, 1.4)$	(0,0,0)

Table 3.1 – Endpoint positions and orientations of the example trajectory.

The feasibility of each trajectory segment is verified following the procedure detailed in Section 3.11. Table 3.2 presents the minimum feasible number of arcs obtained in this process along with the duration of each trajectory segment and the feasible value of $\hat{\ddot{\beta}}_{ep}$ used at each endpoint for identical translational and rotational amplitude functions given by eq. (3.53). In the event that a feasible number of arcs cannot be found to connect a given segment, other values for $\hat{\ddot{\beta}}_{ep}$ can be used, or intermediate points can be inserted in the sequence (Jiang et al., 2018a). Alternatively, the whole trajectory can be reattempted from the start with a different value of z_0.

Target Point	$\hat{\ddot{\beta}}$	p	Duration $T(s)$
0	-1	8	9.4944
1	-2.9872	9	10.6739
2	-7.5394	9	10.6740
3	-0.1401	12	14.2291
4	-5.1933	9	10.6732
5	-6.5391	13	15.4236
6	-14.6701	4	4.7472
0	-1	—	—

Table 3.2 – Value of parameter $\hat{\ddot{\beta}}$ used at each endpoint, as well as number of arcs p and duration T of each trajectory segment for a translational and a rotational amplitude function given by eq. (3.53).

The translational and rotational components of the trajectory, computed with the number of arcs of Table 3.2, are illustrated in Figs. 3.10 and 3.11 respectively, while Fig. 3.12 presents

the tensions throughout the motion. It is clear from Fig. 3.10a that the platform reaches positions that are located far beyond its static workspace. From Fig. 3.12, it can be observed that the tensions in the cables are continuous and positive at all instants of the trajectory. In this regard, it is recalled that the trajectory is devised such that, if the tensions are deemed of unacceptably low magnitude along a given segment, augmenting the number of arcs of the hypocycloid by an even number is guaranteed—if the newly generated motion is feasible—to increase the minimum tension in the cables. Hence, this technique can be used in practice to avoid losing cable tension due to experimental or control error.

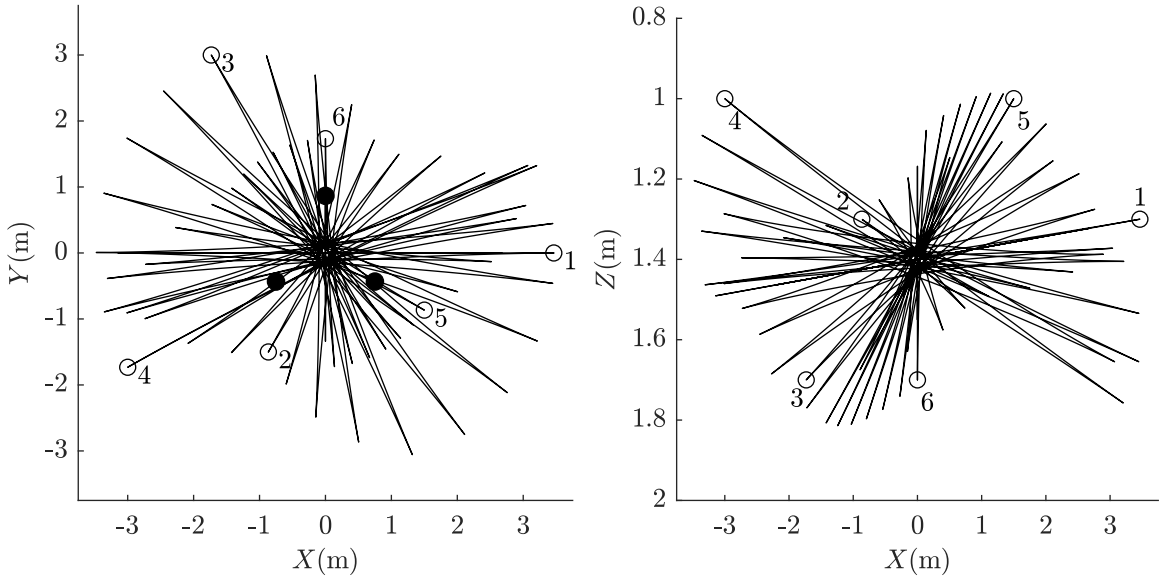

(a) Top view of the example trajectory. The dark circles represent the fixed attachment points of the mechanism (position of the spools).

(b) Side view of the example trajectory.

Figure 3.10 – Translational component of the example trajectory.

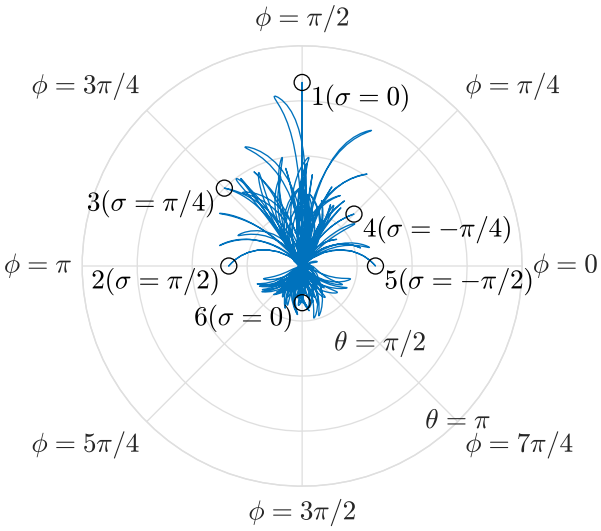

Figure 3.11 – Orientational component of the example trajectory.

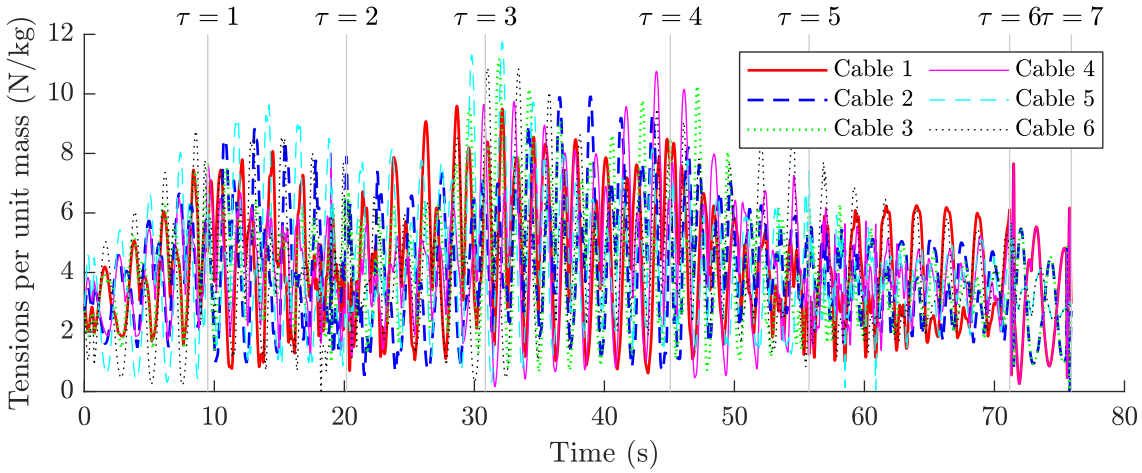

Figure 3.12 – Computed tensions along the trajectory.

3.12.3 Performance of the Rotational Trajectory Motion

In this section, the proportion of attainable target orientations is evaluated for some final positions of the platform in order to assess the performance of the rotational trajectory motion. To this end, the orientational workspace of the mechanism is first computed for the said position using the procedure described in Section 3.10.2. Then, the orientational workspace is uniformly discretized and, for each discrete orientation, a horizontal static-to-dynamic transition trajectory is attempted using the proposed trajectory formulation for multiple numbers of arcs p and values of parameter $\widehat{\ddot{\beta}}_1$ at the final pose. If, for at least one pair of values of p and $\widehat{\ddot{\beta}}_1$, no cable and platform interferences, singularity crossing and negative tension in the cables is encountered along the motion, then the trajectory is deemed feasible by virtue of Section 3.11 and the considered target orientation is considered to be attainable by the proposed

formulation. Moreover, using the same discretization of the orientational workspace for more than one final position of the platform, numbers of accessible and attainable orientations can be compared for multiple final positions and conclusions can be drawn.

Table 3.3 presents the number of accessible orientations of the mechanism, as well as the number and proportion of attainable orientations by the trajectory for some final positions of the platform. In the computation of the orientational workspace, angles (ϕ, θ, σ) were each incremented by steps of $\pi/32$ rad until mechanical interferences or singularities were encountered. This orientational workspace was only evaluated for target positions on the X– and Y–axes since final positions on the Y–axis account for positions lying in a plane passing by a cable spool and the central vertical axis of the mechanism (referred to as a spool plane) while final positions on the X–axis correspond to positions lying in a plane bisecting two spool planes. Therefore, for a given final orientation defined with respect to the central vertical axis of the mechanism, final positions on the X– and Y–axes generate the two most different arrangements of cables possible, and as such can be expected to yield the maximum and minimum proportions of attainable orientations by the proposed trajectory at the corresponding distance from the central vertical axis.

$z_1 = 1.7$	$x_1 = 1.5b$ $y_1 = 0$	$x_1 = 3b$ $y_1 = 0$	$x_1 = 0$ $y_1 = 1.5b$	$x_1 = 0$ $y_1 = 3b$
Number of accessible orientations	27610	32141	25788	30290
Number of attainable orientations	26816	29375	25482	28383
Proportion of attainable orientations	97.1%	91.4%	98.8%	93.7%

Table 3.3 – Number of accessible orientations, and number and proportion of attainable orientations by the proposed trajectory for some final points.

Overall, Table 3.3 shows that the proposed trajectory can reach over 90% of the accessible orientations of the mechanism for each of the four final positions evaluated. This result is all the more significant that, as it should be reiterated, orientational workspaces of cable-suspended mechanisms are quite large since neither the passive nor the active joints have a restricted range of motion. For example, although not shown in any figure, the orientational workspace of each final position of Table 3.3 comprises orientations whose tilt angle surpasses 90° everywhere in the range $\phi \in [30^\circ, 150^\circ]$ as well as orientations whose torsion angle exceeds 100° in both directions. These large orientational workspaces, combined with the high pro-

portions of attainable orientations by the trajectory, imply that the proposed formulation is capable of reaching orientations located far away from the reference orientation while keeping tensile-only forces in the cables. As a matter of fact, it was observed, while processing the data that led to Table 3.3, that the proposed trajectory can feasibly reach orientations with torsion angle of 95° or tilt angles of 125° and this, for each position appearing in Table 3.3.

Specifically, the number of accessible orientations of the mechanism seems to increase as the end-effector 1) gets closer to a plane passing by a cable spool and the central vertical axis of the mechanism and 2) gets farther from the central vertical axis. Moreover, since the additional accessible orientations that large orientational workspaces admit over smaller orientational workspaces are not found near the reference orientation but rather on the outer layer of the workspace, and since the proposed trajectory is less likely to yield a feasible motion for these far away orientations, it should come as no surprise that final positions with large orientational workspaces have a lower proportion of attainable orientations than final positions with smaller orientational workspaces.

Moreover, since the final positions of Table 3.3 on the X– and Y–axes produce the two most different arrangements of cables for a given orientation, it is expected that any other position of the platform located between $1.5b$ and $3b$ from the central vertical axis would yield numbers of accessible and attainable orientations bounded by the values given in Table 3.3. Correspondingly, in the annulus defined by the two radii, it can be conjectured that the proposed trajectory formulation is capable of reaching more than 90% of the accessible orientations of every final position of the platform while maintaining tension in the cables. Table 3.4 gives the minimum proportion of attainable orientations in the annulus defined by radii $1.5b$ and $3b$ for different heights of the platform. As it can be observed from the table, comparable minimum proportions of attainable orientations are obtained for the different heights of the end-effector, and hence the performance of the trajectory is sustained inside the vertical hollow cylinder defined by the radii $1.5b$ and $3b$.

z_1 (m)	Minimum proportion of attainable orientations
1	81.7%
1.4	88.0%
1.7	91.4%
2	92.8%
2.4	95.1%

Table 3.4 – Minimum proportion of attainable orientations in the annulus defined by radii $1.5b$ and $3b$ for different heights of the platform.

3.13 Conclusion

This paper proposes a general approach for the planning of point-to-point trajectories that extend beyond the static workspace for 6-dof cable-suspended parallel mechanisms. First, it is pointed out that, although it maximizes the static workspace, the architecture used in Jiang et al. (2018b,a) and Xiang et al. (2020b) is not ideal for maximizing the dynamic workspace, i.e., for producing trajectories that extend beyond the static workspace. A generalization of the hypocycloidal trajectory proposed in Dion-Gauvin and Gosselin (2018) is presented for the planning of the translational component of the trajectories. Quaternions and spherical linear interpolation are then proposed for the rotational component of the trajectories and a novel formulation to connect two arbitrary orientations through oscillations going through the reference orientation is proposed. It is also shown that the impact of the translational component of the trajectories on the cable tension constraints is much more significant than that of the rotational component. A method is then presented for the verification of the feasibility of the trajectory. A cylindrical coordinate system that provides a very natural description of the trajectories is then proposed and simulation results are given. The proposed method is shown to be very effective at generating feasible trajectories that can connect arbitrary points using a minimum number of intermediate oscillations. Future work includes the implementation of the method on a real cable-suspended robot. Potential applications include pick and place tasks in industrial environments, the displacement of objects in entertainment systems and the support of drones for extended flying time.

3.14 Appendix: Derivation of the hypocycloid of variable amplitude

The hypocycloid of variable amplitude consists of a generalization of the standard hypocycloid (Lawrence, 1972) in which the cusps can be positioned at different distances from the centre of the curve. As represented in Fig. 3.13, it is generated by the trace of a fixed point on the circumference of a small circle whose radius varies as it rolls on the inside of a larger spiral-like curve. While the spiral-like curve $R(\theta)$ passes through the desired position of the first and last cusp and thus must have its expression known from the outset, the variation of the radius of the inner circle $r(\theta)$ as it rolls without slipping is determined through the derivation.

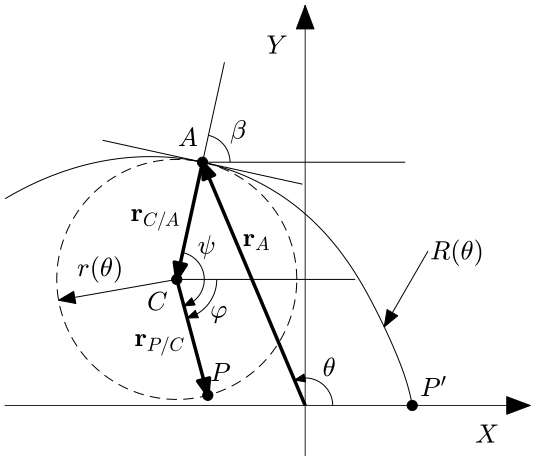

Figure 3.13 – Construction of the hypocycloid of variable amplitude.

Referring to Fig. 3.13, the parametric equations of the hypocycloid of variable amplitude are given by the coordinates of point P, whose position vector $\mathbf{r}_P$ can be decomposed as

$$\mathbf{r}_P = \mathbf{r}_A + \mathbf{r}_{C/A} + \mathbf{r}_{P/C}, \tag{3.101}$$

where $\mathbf{r}_A$ is the position vector of the contact point A between the circle and the spiral-like shape $R(\theta)$, $\mathbf{r}_{C/A}$ is the position vector of the centre of the circle with respect to point A, and $\mathbf{r}_{P/C}$ is the position vector of point P relative to point C. First of all, vector $\mathbf{r}_A$ is readily given by

$$\mathbf{r}_A = \begin{bmatrix} R(\theta)\cos\theta \\ R(\theta)\sin\theta \end{bmatrix}. \tag{3.102}$$

Considering that the tangent of the curve at point A is given by the derivative of the curve at point A, namely

$$\frac{d\mathbf{r}_A}{d\theta} = \begin{bmatrix} R'(\theta)\cos\theta - R(\theta)\sin\theta \\ R'(\theta)\sin\theta + R(\theta)\cos\theta \end{bmatrix}, \tag{3.103}$$

vector $\mathbf{r}_{C/A}$, which is perpendicular to the tangent at point A, can be written as

$$\mathbf{r}_{C/A} = \frac{r(\theta)}{\sqrt{R(\theta)^2 + R'(\theta)^2}} \begin{bmatrix} -R'(\theta)\sin\theta - R(\theta)\cos\theta \\ R'(\theta)\cos\theta - R(\theta)\sin\theta \end{bmatrix}, \tag{3.104}$$

which simply consists of eq. (3.103) rotated 90° counterclockwise with the appropriate scaling. Finally, vector $\mathbf{r}_{P/C}$ is readily written as

$$\mathbf{r}_{P/C} = \begin{bmatrix} r(\theta)\cos\varphi \\ -r(\theta)\sin\varphi \end{bmatrix}, \tag{3.105}$$

where angle φ is the angle of vector $\mathbf{r}_{P/C}$ with respect to the positive direction of the X–axis, measured clockwise. In accordance with Fig. 3.13, defining β as the angle of the outward perpendicular of the spiral-like curve at point A with respect to positive direction of the X–axis and angle ψ as the angle of vector $\mathbf{r}_{P/C}$ with respect to vector $-\mathbf{r}_{C/A}$, measured clockwise, angle φ can be written as

$$\varphi = \psi - \beta, \tag{3.106}$$

and hence vector $\mathbf{r}_{P/C}$ becomes

$$\mathbf{r}_{P/C} = \begin{bmatrix} r(\theta)\cos\psi\cos\beta + r(\theta)\sin\psi\sin\beta \\ -r(\theta)\sin\psi\cos\beta + r(\theta)\cos\psi\sin\beta \end{bmatrix}. \tag{3.107}$$

Furthermore, observing from Fig. 3.13 that vector $\mathbf{r}_{C/A}$ given by eq. (3.104) can also be written as

$$\mathbf{r}_{C/A} = -r(\theta) \begin{bmatrix} \cos\beta \\ \sin\beta \end{bmatrix}, \tag{3.108}$$

angle β can be eliminated from eq. (3.107), yielding

$$\mathbf{r}_{P/C} = \frac{r(\theta)}{\sqrt{R(\theta)^2 + R'(\theta)^2}} \begin{bmatrix} R(\theta)(\cos\psi\cos\theta + \sin\psi\sin\theta) + R'(\theta)(\cos\psi\sin\theta - \sin\psi\cos\theta) \\ R(\theta)(\cos\psi\sin\theta - \sin\psi\cos\theta) - R'(\theta)(\cos\psi\cos\theta + \sin\psi\sin\theta) \end{bmatrix}. \tag{3.109}$$

The above equation expresses the position vector of point P relative to point C as a function of the angles θ and ψ. On the small circle, point P is the point that is in contact with the spiral-like curve at the start of the rolling motion, i.e., when $\theta = 0$. Therefore, were the circle not having its radius vary along the spiral-like curve, the length of the irregular arc segment on the spiral-like curve AP' would correspond to the length of the circular arc AP. This condition nevertheless remains true infinitesimally, namely

$$dS_{AP} = dS_{AP'}, \tag{3.110}$$

where dS_{AP} is a differential element of length along the circle, which is given by

$$dS_{AP} = r(\theta)d\psi, \tag{3.111}$$

and where, making use of the arc length formula in polar coordinates, a differential element of length along the spiral-like curve $dS_{AP'}$ can be written as

$$dS_{AP'} = \sqrt{R(\theta)^2 + R'(\theta)^2}\, d\theta. \tag{3.112}$$

Equating the last two equations, separating the variables and integrating yields an expression for ψ, namely

$$\psi = \int_0^\theta \frac{\sqrt{R(\theta)^2 + R'(\theta)^2}}{r(\theta)}\, d\theta, \tag{3.113}$$

whose closed-form solution does not appear to exist for arbitrary spiral-like curve $R(\theta)$ and circle of variable radius $r(\theta)$. However, setting the undetermined function $r(\theta)$ such that the integrand of the foregone equation does not depend on θ, i.e.,

$$\frac{\sqrt{R(\theta)^2 + R'(\theta)^2}}{r(\theta)} = n_h = \text{const.}, \tag{3.114}$$

eq. (3.113) becomes

$$\psi = n_h \theta, \tag{3.115}$$

which is an expression that is also found in the derivation of the standard hypocycloid. Therefore, substituting eqs. (3.114) and (3.115) into eq. (3.109) and adding the resulting expression to eqs. (3.102) and (3.104) to fulfill eq. (3.101) yields the equation for the position vector of point P as a function of θ only, namely

$$\mathbf{r}_P = \frac{1}{n_h} \begin{bmatrix} R(\theta)\left((n_h - 1)\cos\theta + \cos((n_h - 1)\theta)\right) - R'(\theta)\left(\sin\theta + \sin((n_h - 1)\theta)\right) \\ R(\theta)\left((n_h - 1)\sin\theta - \sin((n_h - 1)\theta)\right) + R'(\theta)\left(\cos\theta - \cos((n_h - 1)\theta)\right) \end{bmatrix}. \tag{3.116}$$

The above expression represents the parametric equations of the hypocyloid of variable amplitude. As expected, these parametric equations simplify to those of the standard hypocycloid for a spiral-like curve that reduces to a circle, as circles are described by the polar equation $R'(\theta) = 0$. Using eq. (3.115), it can be shown that parameter n_h appearing in eq. (3.116) denotes the number of cusps per lap of the curve or, alternatively, its number of arcs per lap. In Section 3.6, it is proposed to use this curve for the translational path of point-to-point trajectories of 6-dof cable-suspended mechanisms.

3.15 Bibliography

J. Albus, R. Bostelman, and N. Dagalakis. The NIST Robocrane. *Journal of Robotic Systems*, 10(5):709–724, 1993. ISSN 07412223. doi:10.1002/rob.4620100509.

E. Barnett and C. Gosselin. Time-optimal trajectory planning of cable-driven parallel mechanisms for fully specified paths with G1-discontinuities. *Journal of Dynamic Systems, Measurement, and Control*, 137(7), 07 2015. ISSN 0022-0434. doi:10.1115/1.4029769.

G. Barrette and C. M. Gosselin. Determination of the dynamic workspace of cable-driven planar parallel mechanisms. *Journal of Mechanical Design, Transactions of the ASME*, 127 (2):242–248, 2005. ISSN 10500472. doi:10.1115/1.1830045.

I. A. Bonev and J. Ryu. A new approach to orientation workspace analysis of 6-dof parallel manipulators. *Mechanism and Machine Theory*, 36(1):15–28, 2001. ISSN 0094-114X. doi:10.1016/S0094-114X(00)00032-X.

S. Bouchard and C. Gosselin. A gravity-powered mechanism for extending the workspace of a cable-driven parallel mechanism: Application to the appearance modelling of objects. *International Journal of Automation Technology*, 4(4):372–379, 2010.

A.-L. Cauchy. Deuxième mémoire sur les polygones et les polyèdres. *Journal de l'École Polytechnique*, pages 87–98, May 1813.

L. L. Cone. Skycam: An aerial robotic camera system. *Byte*, 10(10):122–132, 1985. ISSN 03605280.

D. Cunningham and H. H. Asada. The winch-bot: A cable-suspended, underactuated robot utilizing parametric self-excitation. In *Proceedings of the 2009 IEEE International Conference on Robotics and Automation*, pages 1844–1850, 2009. doi:10.1109/ROBOT.2009.5152378.

E. B. Dam, M. Koch, and M. Lillholm. Quaternions, interpolation and animation. Technical report, Datalogisk Institut, Københavns Universitet, 1998.

P. Dion-Gauvin and C. Gosselin. Trajectory planning for the static to dynamic transition of point-mass cable-suspended parallel mechanisms. *Mechanism and Machine Theory*, 113: 158–178, 07 2017. doi:10.1016/j.mechmachtheory.2017.03.003.

P. Dion-Gauvin and C. Gosselin. Dynamic point-to-point trajectory planning of a three-dof cable-suspended mechanism using the hypocycloid curve. *IEEE/ASME Transactions on Mechatronics*, 23(4):1964–1972, 2018. doi:10.1109/TMECH.2018.2840051.

C. Gosselin. Global planning of dynamically feasible trajectories for three-dof spatial cable-suspended parallel robots. In T. Bruckmann and A. Pott, editors, *Cable-Driven Parallel Robots*, pages 3–22. Springer Berlin Heidelberg, Berlin, Heidelberg, 2013. ISBN 978-3-642-31988-4. doi:10.1007/978-3-642-31988-4_1.

C. Gosselin, P. Ren, and S. Foucault. Dynamic trajectory planning of a two-dof cable-suspended parallel robot. In *Proceedings of the IEEE International Conference on Robotics and Automation*, pages 1476–1481, St. Paul, MN, USA, 2012. doi:10.1109/ICRA.2012.6224683.

B. Graf. Quaternions and dynamics, 2008.

J. Hesselbach, M. B. Helm, and S. Soetebier. *Connecting Assembly Modes for Workspace Enlargement*, pages 347–356. Springer Netherlands, Dordrecht, 2002. ISBN 978-94-017-0657-5. doi:10.1007/978-94-017-0657-5_37.

R. B. Hill, D. Six, A. Chriette, S. Briot, and P. Martinet. Crossing type 2 singularities of parallel robots without pre-planned trajectory with a virtual-constraint-based controller. In *Proceedings of the IEEE International Conference on Robotics and Automation*, pages 6080–6085, 2017. doi:10.1109/ICRA.2017.7989721.

E. Idà, T. Bruckmann, and M. Carricato. Rest-to-rest trajectory planning for underactuated cable-driven parallel robots. *IEEE Transactions on Robotics*, 35(6):1338–1351, 2019. doi:10.1109/TRO.2019.2931483.

X. Jiang and C. Gosselin. Trajectory generation for three-degree-of-freedom cable-suspended parallel robots based on analytical integration of the dynamic equations. *Journal of Mechanisms and Robotics*, 8(4), 2016a. ISSN 1942-4302. doi:10.1115/1.4031501.

X. Jiang and C. Gosselin. Dynamic point-to-point trajectory planning of a three-dof cable-suspended parallel robot. *IEEE Transactions on Robotics*, 32(6):1550–1557, Dec 2016b. ISSN 1552-3098. doi:10.1109/TRO.2016.2597315.

X. Jiang, E. Barnett, and C. Gosselin. Dynamic point-to-point trajectory planning beyond the static workspace for six-dof cable-suspended parallel robots. *IEEE Transactions on Robotics*, 34(3):781–793, 2018a. doi:10.1109/TRO.2018.2794549.

X. Jiang, E. Barnett, and C. Gosselin. Periodic trajectory planning beyond the static workspace for 6-dof cable-suspended parallel robots. *IEEE Transactions on Robotics*, 34 (4):1128–1140, 2018b. doi:10.1109/TRO.2018.2819668.

X. Jiang, D. Lin, and Q. Li. Dynamically feasible transition trajectory planning for three-dof cable-suspended parallel robots. In *2019 IEEE 9th Annual International Conference on CYBER Technology in Automation, Control, and Intelligent Systems (CYBER)*, pages 789–794. IEEE, 2019. doi:10.1109/CYBER46603.2019.9066724.

M. Korayem and M. Bamdad. Dynamic load-carrying capacity of cable-suspended parallel manipulators. *The International Journal of Advanced Manufacturing Technology*, 44(7): 829–840, 10 2009. doi:10.1007/s00170-008-1890-x.

J. Lawrence. *A Catalog of Special Plane Curves*. Dover Books on Mathematics. Dover Publications, 1972. ISBN 9780486602882.

S. Lefrançois and C. Gosselin. Point-to-point motion control of a pendulum-like 3-dof underactuated cable-driven robot. In *Proceedings of the IEEE International Conference on Robotics and Automation*, pages 5187–5193, Anchorage, AK, USA, 2010. doi:10.1109/ROBOT.2010.5509656.

D. Lin, G. Mottola, M. Carricato, X. Jiang, and Q. Li. Dynamically-feasible trajectories for a cable-suspended robot performing throwing operations. In *ROMANSY 23 - Robot Design, Dynamics and Control*, pages 547–555. Springer, 2020. ISBN 978-3-030-58379-8. doi:10.1007/978-3-030-58380-4_65.

J.-P. Merlet. Parallel manipulators. Part 2 : Theory. Singular configurations and Grassmann geometry. Research Report RR-0791, INRIA, 1988.

G. Mottola, C. Gosselin, and M. Carricato. Dynamically-feasible elliptical trajectories for fully constrained 3-dof cable-suspended parallel robots. In *Cable-Driven Parallel Robots*, pages 219–230. Springer, 07 2018. ISBN 978-3-319-61430-4. doi:10.1007/978-3-319-61431-1_19.

G. Mottola, C. Gosselin, and M. Carricato. Dynamically feasible motions of a class of purely-translational cable-suspended parallel robots. *Mechanism and Machine Theory*, 132:193–206, 2019. ISSN 0094-114X. doi:10.1016/j.mechmachtheory.2018.10.017.

L. Scalera, A. Gasparetto, and D. Zanotto. Design and experimental validation of a 3-dof underactuated pendulum-like robot. *IEEE/ASME Transactions on Mechatronics*, 25(1): 217–228, 2020. doi:10.1109/TMECH.2019.2947915.

V. Schmidt, W. Kraus, W. Y. Ho, J. Seon, A. Pott, J.-O. Park, and A. Verl. Extending dynamic trajectories of cable-driven parallel robots as a novel robotic roller coaster. In *Proceedings for the Joint Conference of ISR 2014 - 45th International Symposium on Robotics and Robotik 2014 - 8th German Conference on Robotics, ISR/ROBOTIK 2014*, pages 367–373, Munich, Germany, 2014.

K. Shoemake. Animating rotation with quaternion curves. In *Proceedings of the 12th Annual Conference on Computer Graphics and Interactive Techniques*, SIGGRAPH '85, page 245–254, New York, NY, USA, 1985. Association for Computing Machinery. ISBN 0897911660. doi:10.1145/325334.325242.

S. Xiang, H. Gao, Z. Liu, and C. Gosselin. Dynamic transition trajectory planning of three-dof cable-suspended parallel robots via linear time-varying MPC. *Mechanism and Machine Theory*, 146:103715, 2020a. ISSN 0094-114X. doi:10.1016/j.mechmachtheory.2019.103715.

S. Xiang, H. Gao, Z. Liu, and C. Gosselin. Trajectory optimization for a six-dof cable-suspended parallel robot with dynamic motions beyond the static workspace. In *Proceedings of the IEEE International Conference on Robotics and Automation*, pages 3903–3908. IEEE, 2020b. doi:10.1109/ICRA40945.2020.9196803.

Y. Xiang, Q. Li, and X. Jiang. Dynamic rotational trajectory planning of a cable-driven parallel robot for passing through singular orientations. *Mechanism and Machine Theory*, 158:104223, 04 2021. ISSN 0094-114X. doi:10.1016/j.mechmachtheory.2020.104223.

D. Zanotto, G. Rosati, and S. Agrawal. Modeling and control of a 3-dof pendulum-like manipulator. In *Proceedings of the IEEE International Conference on Robotics and Automation*, pages 3964–3969, Shanghai, China, 2011. doi:10.1109/ICRA.2011.5980198.

F. Zhang. *The Schur Complement and its Applications*, volume 4 of *Numerical Methods and Algorithms*. Springer, New York, 2005. ISBN 0387242716 9780387242712 0387242732 9780387242736 1280337451 9781280337451. doi:10.1007/b105056.

N. Zhang and W. Shang. Dynamic trajectory planning of a 3-dof under-constrained cable-driven parallel robot. *Mechanism and Machine Theory*, 98:21–35, 2016. ISSN 0094-114X. doi:10.1016/j.mechmachtheory.2015.11.007.

N. Zhang, W. Shang, and S. Cong. Geometry-based trajectory planning of a 3-3 cable-suspended parallel robot. *IEEE Transactions on Robotics*, 33(2):484–491, 2017. doi:10.1109/TRO.2016.2631591.

B. Zi, B. Duan, J. Du, and H. Bao. Dynamic modeling and active control of a cable-suspended parallel robot. *Mechatronics*, 18(1):1 – 12, 2008. doi:10.1016/j.mechatronics.2007.09.004.

N. Zoso and C. Gosselin. Point-to-point motion planning of a parallel 3-dof underactuated cable-suspended robot. In *Proceedings of the IEEE International Conference on Robotics and Automation*, pages 2325–2330, St. Paul, MN, USA, 2012. doi:10.1109/ICRA.2012.6224598.

Conclusion

Résumé et contributions de la thèse

La présente thèse propose des planifications de trajectoires analytiques de type point à point pour des mécanismes à cables suspendus à 2, 3 et 6 degrés de liberté. Pour chacun des mécanismes étudiés, une relation d'états cinématiques idéaux permettant de positionner l'effecteur le plus loin possible des lieux de tension nulle est développée. Ce concept général peut être mis à profit dans la résolution de problématiques variées relatives à tous les types de mécanismes entraînés par câbles, et constitue donc en soi un important résultat de ce travail de recherche. En particulier, dans cette thèse, pour chaque planification de trajectoire développée, la relation d'états cinématiques idéaux ou une approximation de celle-ci est imposée aux points limites de la trajectoire afin d'augmenter la probabilité que le mouvement résultant induise des forces exclusivement de tension dans les câbles.

Une trajectoire point à point de transition pour mécanismes à effecteur ponctuel à 2 et à 3 ddl est d'abord proposée dans le Chapitre 1. Celle-ci consiste en des oscillations rectilignes d'amplitude croissante centrées à la pose au repos, dont il ne suffit que le tracé se trouve entièrement sous le plan des enrouleurs pour que sa faisabilité soit garantie. Cette trajectoire constitue un cas particulier de la planification point à point classique pour mécanismes spatiaux à 3 ddl qui est développée dans le Chapitre 2. Cette dernière trajectoire consiste en une hypocycloïde augmentée d'une fonction d'amplitude qui peut joindre n'importe quelles deux positions de l'espace tridimensionnel. Similairement aux mouvements de transition proposés dans le Chapitre 1, il est démontré que la trajectoire hypocycloïdale est nécessairement réalisable lorsque son enveloppe circulaire demeure strictement sous le plan formé par les enrouleurs. Enfin, une évolution naturelle de cette formulation est articulée comme composante translationnelle de la trajectoire à 6 ddl dans le Chapitre 3. Cette trajectoire en translation est adjointe à une composante en rotation constituée d'oscillations angulaires le long des arcs de l'hypocycloïde. Les avantages et limites du tracé hypocycloïdal étant évalués dans le Chapitre 2, seule la pertinence de la composante rotationnelle du mouvement est examinée dans le Chapitre 3 : il est obtenu que, au moyen d'une trajectoire horizontale partant d'une pose au repos, cette planification parvient à joindre, pour certaines positions typiques de la plate-forme, environ 90% de l'espace atteignable en orientation du mécanisme.

Ainsi, chaque planification ayant comme assise les planifications de trajectoires plus élémentaires, les résultats obtenus des planifications comptant un plus petit nombre de degrés de liberté tiennent également pour les planifications plus sophistiquées. Par exemple, la planification de trajectoires de transition du Chapitre 1 établit des paramètres de conception de la fonction d'amplitude dans le but d'en améliorer l'efficacité, lesquels paramètres de conception s'appliquent également intégralement aux fonctions d'amplitude des planifications de trajectoires des mécanismes à 3 et à 6 ddl des Chapitres 2 et 3, parce que celles-ci sont développées aux mêmes fins et sont soumises aux mêmes contraintes aux points limites. En outre, les lignes directrices établies dans le Chapitre 2 visant à postionner le foyer de l'hypocycloïde de manière à assurer la faisabilité de la trajectoire souhaitée, s'appliquent en totalité à la planification du mécanisme hexapodal du Chapitre 3 puisque la composante translationnelle de chacun des mouvements est de la même nature. Enfin, dans le Chapitre 3, la planification de trajectoire du mécanisme à 6 ddl présente une étude du mouvement en orientation d'une plate-forme à l'extérieur de l'emprise de la base du mécanisme qui est à l'origine de contributions pouvant s'étendre à d'autres travaux portant sur le même type de mouvement. Parmi ces contributions figurent 1) un exposé que les architectures classiques de mécanismes hexapodaux sont à prioriser pour réaliser des trajectoires dynamiques avec des mécanismes à câbles suspendus ; 2) la démonstration que la contrainte de l'unilatéralité des forces dans les câbles ne restreint pas l'ensemble des poses qu'un mécanisme à câbles suspendus peut atteindre à vitesse nulle et accélération non-nulle ; et 3) l'introduction d'un repère novateur permettant une visualisation plus intuitive de la configuration du mécanisme.

Ainsi, les planifications de trajectoires développées dans le cadre de ce travail de recherche répondent aux objectifs et forment un tout cohérent, complet et intégré. Il reste maintenant à en dénicher des applications réelles afin d'en exploiter le plein potentiel.

Avenues de recherche futures

Les trajectoires proposées dans cette thèse s'appuyant sur le mouvement d'un pendule, elles ne sont pas optimisées pour accomplir certains types de mouvement dans certains contextes. Par exemple, comme un pendule, les trajectoires induisent une accélération translationnelle maximale—à la pose cible à atteindre—et une vitesse translationnelle maximale—à la position d'équilibre du système oscillant—qui sont proportionnelles à l'amplitude du mouvement oscillatoire. Par conséquent, d'importantes vitesses et accélérations maximales sont générées lorsque la pose cible à atteindre se trouve à une grande distance de l'axe central vertical du mécanisme. Or, puisqu'il suffit que la force transmise dans les cables soit dirigée entre les enrouleurs d'un mécanisme à effecteur ponctuel pour que des forces exclusivement de tension y soient induites, il devrait être possible, pour un mécanisme disposant d'une grande base, d'admettre en des positions situées loin de son axe central vertical mais près de la frontière de son espace de travail statique des accélérations translationnelles plus modérées que celles

prédites par le modèle d'un pendule simple dont l'unique point d'attache se trouve au centroïde des enrouleurs du mécanisme. Ainsi, une avenue de recherche potentielle consiste en le développement de planifications de trajectoires dynamiques qui tirent profit de la taille du mécanisme pour induire à l'effecteur des vitesses et accélérations translationnelles maximales plus faibles que celles générées par les formulations proposées dans cette thèse.

Enfin, un aspect des trajectoires dynamiques de mécanismes à cables suspendus qui présente possiblement un certain intérêt pratique réside en la réalisation d'opérations de lancement de projectiles en cours de trajectoire. Puisque le projectile suit, une fois relâché de l'effecteur, une trajectoire balistique facilement calculable, l'exercice consiste à établir l'instant de largage afin que le projectile atteigne une position cible prédéterminée. Plusieurs enjeux demeurent à être résolus avant que cette stratégie puisse être mise en oeuvre, notamment la minimisation de la fluctuation des forces dans les câbles au moment du relâchement du projectile, la conception d'un mécanisme de relâchement du projectile, une analyse de l'erreur engendrée sur la position finale atteinte par le projectile pour des erreurs de position, vitesse et accélération du largage, et la construction d'un prototype. Ainsi, des investigations plus approfondies sont requises dans ce domaine.

Bibliographie

J. Albus, R. Bostelman, and N. Dagalakis. The NIST Robocrane. *Journal of Robotic Systems*, 10(5) :709–724, 1993. ISSN 07412223. doi:10.1002/rob.4620100509.

A. B. Alp and S. K. Agrawal. Cable suspended robots : Design, planning and control. In *Proceedings of the IEEE International Conference on Robotics and Automation*, volume 4, pages 4275–4280, Washington, DC, USA, 2002. doi:10.1109/ROBOT.2002.1014428.

E. Barnett and C. Gosselin. Time-optimal trajectory planning of cable-driven parallel mechanisms for fully specified paths with G1-discontinuities. *Journal of Dynamic Systems, Measurement, and Control*, 137(7), 07 2015. ISSN 0022-0434. doi:10.1115/1.4029769.

G. Barrette and C. M. Gosselin. Determination of the dynamic workspace of cable-driven planar parallel mechanisms. *Journal of Mechanical Design, Transactions of the ASME*, 127 (2) :242–248, 2005. ISSN 10500472. doi:10.1115/1.1830045.

A. Berti, M. Gouttefarde, and M. Carricato. Dynamic recovery of cable-suspended parallel robots after a cable failure. In *Proceedings of the 2016 ARK Conference*, pages 338–344, 2016.

I. A. Bonev and J. Ryu. A new approach to orientation workspace analysis of 6-dof parallel manipulators. *Mechanism and Machine Theory*, 36(1) :15–28, 2001. ISSN 0094-114X. doi:10.1016/S0094-114X(00)00032-X.

S. Bouchard and C. Gosselin. A gravity-powered mechanism for extending the workspace of a cable-driven parallel mechanism : Application to the appearance modelling of objects. *International Journal of Automation Technology*, 4(4) :372–379, 2010.

A.-L. Cauchy. Deuxième mémoire sur les polygones et les polyèdres. *Journal de l'École Polytechnique*, pages 87–98, May 1813.

L. L. Cone. Skycam : An aerial robotic camera system. *Byte*, 10(10) :122–132, 1985. ISSN 03605280.

D. Cunningham and H. H. Asada. The winch-bot : A cable-suspended, under-actuated robot utilizing parametric self-excitation. In *Proceedings of the 2009 IEEE International Conference on Robotics and Automation*, pages 1844–1850, 2009. doi:10.1109/ROBOT.2009.5152378.

E. B. Dam, M. Koch, and M. Lillholm. Quaternions, interpolation and animation. Technical report, Datalogisk Institut, Københavns Universitet, 1998.

P. Dion-Gauvin and C. Gosselin. Trajectory planning for the static to dynamic transition of point-mass cable-suspended parallel mechanisms. *Mechanism and Machine Theory*, 113 : 158–178, 07 2017. doi:10.1016/j.mechmachtheory.2017.03.003.

P. Dion-Gauvin and C. Gosselin. Dynamic point-to-point trajectory planning of a three-dof cable-suspended mechanism using the hypocycloid curve. *IEEE/ASME Transactions on Mechatronics*, 23(4) :1964–1972, 2018. doi:10.1109/TMECH.2018.2840051.

P. Dion-Gauvin and C. Gosselin. Beyond-the-static-workspace point-to-point trajectory planning of a 6-dof cable-suspended mechanism using oscillating SLERP. *Mechanism and Machine Theory*, 174 :104894, 2022. ISSN 0094-114X. doi:10.1016/j.mechmachtheory.2022.104894.

C. Gosselin. Global planning of dynamically feasible trajectories for three-dof spatial cable-suspended parallel robots. In T. Bruckmann and A. Pott, editors, *Cable-Driven Parallel Robots*, pages 3–22. Springer Berlin Heidelberg, Berlin, Heidelberg, 2013. ISBN 978-3-642-31988-4. doi:10.1007/978-3-642-31988-4_1.

C. Gosselin and S. Foucault. Dynamic point-to-point trajectory planning of a two-dof cable-suspended parallel robot. *IEEE Transactions on Robotics*, 30(3) :728 – 736, 2014. ISSN 1552-3098. doi:10.1109/TRO.2013.2292451.

C. Gosselin and A. Hadj-Messaoud. Automatic planning of smooth trajectories for pick-and-place operations. *Journal of Mechanical Design, Transactions of the ASME*, 115(3) : 450–456, September 1993. doi:10.1115/1.2919211.

C. Gosselin, P. Ren, and S. Foucault. Dynamic trajectory planning of a two-dof cable-suspended parallel robot. In *Proceedings of the IEEE International Conference on Robotics and Automation*, pages 1476–1481, St. Paul, MN, USA, 2012. doi:10.1109/ICRA.2012.6224683.

M. Gouttefarde, S. Krut, F. Pierrot, and N. Ramdani. On the design of fully constrained parallel cable-driven robots. In *Advances in Robot Kinematics : Analysis and Design*, pages 71–78. Springer Netherlands, Dordrecht, 2008. ISBN 978-1-4020-8599-4. doi:10.1007/978-1-4020-8600-7_8.

B. Graf. Quaternions and dynamics, 2008.

J. Hesselbach, M. B. Helm, and S. Soetebier. *Connecting Assembly Modes for Workspace Enlargement*, pages 347–356. Springer Netherlands, Dordrecht, 2002. ISBN 978-94-017-0657-5. doi:10.1007/978-94-017-0657-5_37.

R. B. Hill, D. Six, A. Chriette, S. Briot, and P. Martinet. Crossing type 2 singularities of parallel robots without pre-planned trajectory with a virtual-constraint-based controller. In *Proceedings of the IEEE International Conference on Robotics and Automation*, pages 6080–6085, 2017. doi:10.1109/ICRA.2017.7989721.

E. Idà, T. Bruckmann, and M. Carricato. Rest-to-rest trajectory planning for underactuated cable-driven parallel robots. *IEEE Transactions on Robotics*, 35(6) :1338–1351, 2019. doi:10.1109/TRO.2019.2931483.

X. Jiang and C. Gosselin. Dynamically feasible trajectories for three-dof planar cable-suspended parallel robots. In *Proceedings of the ASME Design Engineering Technical Conference*, volume 5A, Buffalo, NY, USA, 2014. doi:10.1115/DETC2014-34419. V05AT08A085.

X. Jiang and C. Gosselin. Trajectory generation for three-degree-of-freedom cable-suspended parallel robots based on analytical integration of the dynamic equations. *Journal of Mechanisms and Robotics*, 8(4), 2016a. ISSN 1942-4302. doi:10.1115/1.4031501.

X. Jiang and C. Gosselin. Dynamic point-to-point trajectory planning of a three-dof cable-suspended parallel robot. *IEEE Transactions on Robotics*, 32(6) :1550–1557, Dec 2016b. ISSN 1552-3098. doi:10.1109/TRO.2016.2597315.

X. Jiang, E. Barnett, and C. Gosselin. Dynamic point-to-point trajectory planning beyond the static workspace for six-dof cable-suspended parallel robots. *IEEE Transactions on Robotics*, 34(3) :781–793, 2018a. doi:10.1109/TRO.2018.2794549.

X. Jiang, E. Barnett, and C. Gosselin. Periodic trajectory planning beyond the static workspace for 6-dof cable-suspended parallel robots. *IEEE Transactions on Robotics*, 34(4) : 1128–1140, 2018b. doi:10.1109/TRO.2018.2819668.

X. Jiang, D. Lin, and Q. Li. Dynamically feasible transition trajectory planning for three-dof cable-suspended parallel robots. In *2019 IEEE 9th Annual International Conference on CYBER Technology in Automation, Control, and Intelligent Systems (CYBER)*, pages 789–794. IEEE, 2019. doi:10.1109/CYBER46603.2019.9066724.

L. Kevac, M. Filipovic, and A. Rakic. The trajectory generation algorithm for the cable-suspended parallel robot—the cpr trajectory solver. *Robotics and Autonomous Systems*, 94 :25–33, 2017. ISSN 0921-8890. doi:10.1016/j.robot.2017.04.018.

M. Korayem and M. Bamdad. Dynamic load-carrying capacity of cable-suspended parallel manipulators. *The International Journal of Advanced Manufacturing Technology*, 44(7) : 829–840, 10 2009. doi:10.1007/s00170-008-1890-x.

M. H. Korayem and H. Tourajizadeh. Maximum dlcc of spatial cable robot for a predefined trajectory within the workspace using closed loop optimal control approach. *Journal of Intelligent and Robotic Systems*, 63(1) :75–99, jul 2011. ISSN 0921-0296. doi:10.1007/s10846-010-9521-9.

R. Kurtz and V. Hayward. Dexterity measure for tendon actuated parallel mechanisms. In *Proceedings of the Fifth International Conference on Advanced Robotics*, volume 2, pages 1141 – 1146, 07 1991. ISBN 0-7803-0078-5. doi:10.1109/ICAR.1991.240402.

J. Lawrence. *A Catalog of Special Plane Curves*. Dover Books on Mathematics. Dover Publications, 1972. ISBN 9780486602882.

S. Lefrançois and C. Gosselin. Point-to-point motion control of a pendulum-like 3-dof underactuated cable-driven robot. In *Proceedings of the IEEE International Conference on Robotics and Automation*, pages 5187–5193, Anchorage, AK, USA, 2010. doi:10.1109/ROBOT.2010.5509656.

W. B. Lim, G. Yang, S. H. Yeo, S. K. Mustafa, and I. M. Chen. A generic tension-closure analysis method for fully-constrained cable-driven parallel manipulators. In *Proceedings of the IEEE International Conference on Robotics and Automation*, pages 2187–2192, May 2009. doi:10.1109/ROBOT.2009.5152772.

D. Lin, G. Mottola, M. Carricato, X. Jiang, and Q. Li. Dynamically-feasible trajectories for a cable-suspended robot performing throwing operations. In *ROMANSY 23 - Robot Design, Dynamics and Control*, pages 547–555. Springer, 2020. ISBN 978-3-030-58379-8. doi:10.1007/978-3-030-58380-4_65.

J.-P. Merlet. Parallel manipulators. Part 2 : Theory. Singular configurations and Grassmann geometry. Research Report RR-0791, INRIA, 1988.

G. Mottola, C. Gosselin, and M. Carricato. Dynamically-feasible elliptical trajectories for fully constrained 3-dof cable-suspended parallel robots. In *Cable-Driven Parallel Robots*, pages 219–230. Springer, 07 2018. ISBN 978-3-319-61430-4. doi:10.1007/978-3-319-61431-1_19.

G. Mottola, C. Gosselin, and M. Carricato. Dynamically feasible motions of a class of purely-translational cable-suspended parallel robots. *Mechanism and Machine Theory*, 132 :193–206, 2019. ISSN 0094-114X. doi:10.1016/j.mechmachtheory.2018.10.017.

K. D. Nguyen, T.-C. Ng, and I.-M. Chen. On algorithms for planning s-curve motion profiles. *International Journal of Advanced Robotic Systems*, 5(1) :99–106, 2008. ISSN 17298806. doi:10.5772/5652.

J. Pusey, A. Fattah, S. Agrawal, and E. Messina. Design and workspace analysis of a 6-6 cable-suspended parallel robot. *Mechanism and Machine Theory*, 39(7) :761–778, 2004. ISSN 0094114X. doi:10.1016/j.mechmachtheory.2004.02.010.

A. T. Riechel and I. Ebert-Uphoff. Force-feasible workspace analysis for under-constrained, point-mass cable robots. In *Proceedings of the IEEE International Conference on Robotics and Automation*, volume 5, pages 4956–4962, April 2004. doi:10.1109/ROBOT.2004.1302503.

L. Scalera, A. Gasparetto, and D. Zanotto. Design and experimental validation of a 3-dof underactuated pendulum-like robot. *IEEE/ASME Transactions on Mechatronics*, 25(1) : 217–228, 2020. doi:10.1109/TMECH.2019.2947915.

V. Schmidt, W. Kraus, W. Y. Ho, J. Seon, A. Pott, J.-O. Park, and A. Verl. Extending dynamic trajectories of cable-driven parallel robots as a novel robotic roller coaster. In *Proceedings for the Joint Conference of ISR 2014 - 45th International Symposium on Robotics and Robotik 2014 - 8th German Conference on Robotics, ISR/ROBOTIK 2014*, pages 367–373, Munich, Germany, 2014.

K. Shoemake. Animating rotation with quaternion curves. In *Proceedings of the 12th Annual Conference on Computer Graphics and Interactive Techniques*, SIGGRAPH '85, page 245–254, New York, NY, USA, 1985. Association for Computing Machinery. ISBN 0897911660. doi:10.1145/325334.325242.

A. Trevisani. Underconstrained planar cable-direct-driven robots : A trajectory planning method ensuring positive and bounded cable tensions. *Mechatronics*, 20(1) :113–127, 2010. ISSN 09574158. doi:10.1016/j.mechatronics.2009.09.011.

S. Xiang, H. Gao, Z. Liu, and C. Gosselin. Dynamic transition trajectory planning of three-dof cable-suspended parallel robots via linear time-varying MPC. *Mechanism and Machine Theory*, 146 :103715, 2020a. ISSN 0094-114X. doi:10.1016/j.mechmachtheory.2019.103715.

S. Xiang, H. Gao, Z. Liu, and C. Gosselin. Trajectory optimization for a six-dof cable-suspended parallel robot with dynamic motions beyond the static workspace. In *Proceedings of the IEEE International Conference on Robotics and Automation*, pages 3903–3908. IEEE, 2020b. doi:10.1109/ICRA40945.2020.9196803.

Y. Xiang, Q. Li, and X. Jiang. Dynamic rotational trajectory planning of a cable-driven parallel robot for passing through singular orientations. *Mechanism and Machine Theory*, 158 :104223, 04 2021. ISSN 0094-114X. doi:10.1016/j.mechmachtheory.2020.104223.

D. Zanotto, G. Rosati, and S. Agrawal. Modeling and control of a 3-dof pendulum-like manipulator. In *Proceedings of the IEEE International Conference on Robotics and Automation*, pages 3964–3969, Shanghai, China, 2011. doi:10.1109/ICRA.2011.5980198.

F. Zhang. *The Schur Complement and its Applications*, volume 4 of *Numerical Methods and Algorithms*. Springer, New York, 2005. ISBN 0387242716 9780387242712 0387242732 9780387242736 1280337451 9781280337451. doi:10.1007/b105056.

N. Zhang and W. Shang. Dynamic trajectory planning of a 3-dof under-constrained cable-driven parallel robot. *Mechanism and Machine Theory*, 98 :21–35, 2016. ISSN 0094-114X. doi:10.1016/j.mechmachtheory.2015.11.007.

N. Zhang, W. Shang, and S. Cong. Geometry-based trajectory planning of a 3-3 cable-suspended parallel robot. *IEEE Transactions on Robotics*, 33(2) :484–491, 2017. doi:10.1109/TRO.2016.2631591.

B. Zi, B. Duan, J. Du, and H. Bao. Dynamic modeling and active control of a cable-suspended parallel robot. *Mechatronics*, 18(1) :1 – 12, 2008. doi:10.1016/j.mechatronics.2007.09.004.

N. Zoso and C. Gosselin. Point-to-point motion planning of a parallel 3-dof underactuated cable-suspended robot. In *Proceedings of the IEEE International Conference on Robotics and Automation*, pages 2325–2330, St. Paul, MN, USA, 2012. doi:10.1109/ICRA.2012.6224598.